

1

2

3

4

Search for supersymmetry in pp collisions with all-hadronic final states using the α_T variable with the CMS detector at the LHC

5

6

Bryn Mathias
Imperial College London

7

Supervisor: Dr Alex Tapper

Abstract

1

2

This is a thesis.

DRAFT

Declaration

There are many like it.

Author

Preface

¹

²

Something witty.

DRAFT

Acknowledgements

¹

²

Thanks.

Contents

1	1. Introduction	9
2	2. Theory	13
3	2.1. The Standard Model (SM)	13
4	2.1.1. Gauge Invariance	14
5	2.1.2. Electro-weak symmetry and interactions	16
6	2.1.3. Quantum Chromo Dynamics	16
7	2.1.4. The Higgs and Electro-weak Symmetry Breaking	17
8	2.2. Beyond the Standard Model	17
9	2.2.1. The Constrained Minimal Super Symmetric Model	18
10	2.2.2. Simplified Models	18
11	3. The CMS detector	20
12	3.1. The Silicon Tracker	21
13	3.2. The Electromagnetic Calorimeter (ECAL)	22
14	3.3. The Hadronic Calorimeter (HCAL)	23
15	3.4. The The Compact Muon Solenoid (CMS) Super-Conducting Solenoid	25
16	3.5. The CMS Muon system	25
17	3.6. The Level-1 Trigger System	26
18	3.7. The High Level Trigger System	27
19	4. Level-1 Calorimeter Trigger	28
20	4.1. Level-1 Trigger Jet Algorithm	29
21	4.2. Level-1 Trigger Performance	32
22	4.3. Level-1 Trigger Pile-up Mitigation	40
23	4.3.1. Effect on trigger efficiency	42
24	4.3.2. Efficiency of H_T Triggers	43
25	4.3.3. Efficiency of Jet Triggers	44
26	4.3.4. Efficiency of MultiJet Triggers	44

1	4.4. Summary	44
2	5. Motivating the α_T Analysis	46
3	5.1. The Problem	46
4	6. Reconstruction and Event selection	48
5	6.1. The α_T variable.	48
6	6.2. Event selection	50
7	6.2.1. Preselection of hadronic objects	50
8	6.2.2. Electrons	52
9	6.2.3. Muons	53
10	6.2.4. Photons	54
11	6.3. Common Analysis cuts	54
12	6.4. High Level triggers for the α_T analysis	57
13	6.4.1. Trigger efficiency measurement	58
14	6.5. Extension to higher analysis dimensions. B-tagging	63
15	7. Background Prediction	71
16	7.1. Electro-Weak Background Prediciton	71
17	7.1.1. The $\mu + \text{Jets}$ control sample	74
18	7.1.2. The $\mu\mu + \text{Jets}$ control sample	75
19	7.1.3. The $\gamma + \text{Jets}$ control sample	75
20	7.1.4. Muon control samples with out an α_T cut.	76
21	7.2. Systematic uncertainties on the electro-weak background model.	79
22	7.3. Motivating the combined systematic on the translation factors	81
23	7.4. Estimating the residual QCD background component.[1]	82
24	7.5. Likelihood model	84
25	7.6. Final Results	88
26	8. Interpretation	94
27	8.1. Signal Models	94
28	8.2. Signal Efficiency	95
29	8.2.1. Constrained Minimal SuperSymmetric Model (CMSSM)	95
30	8.2.2. Simplified Models	95
31	8.3. Uncertainty on Signal Efficiency	96
32	8.4. Choice of Parton Density Function (PDF) set at generator level.	97
33	8.5. Effects of Jet Energy Scale Variations on Signal Efficiency	99

1	8.6. Systematic Uncertainty on Signal Yield from Cleaning Filters and Object	
2	Vetoies	99
3	8.7. Interpretation in terms of new physics models.	100
4	9. Conclusion	105
5	A. Additional information on triggers	106
6	B. Addition information on background estimation methods	111
7	B.1. Determination of k_{QCD}	111
8	C. Closure tests and systematic uncertainties	112
9	C.1. Defining muon samples without an α_T requirement	112
10	C.2. Closure tests for inclusive analysis	113
11	C.3. Closure tests for b-tag analysis	114
12	C.4. Closure tests concerning pile-up	115
13	D. Signal efficiency	118
14	D.1. CMSSM	118
15	D.2. T1	119
16	D.3. T2	120
17	D.4. T2tt	121
18	D.5. T2bb	122
19	D.6. T1tttt	123
20	D.7. T1bbbb	124
21	D.8. Signal contamination for T1tttt	125
22	E. Experimental systematic uncertainties on signal efficiency times accep-	
23	tance	126
24	E.1. Systematics due to jet energy scale uncertainties	126
25	E.2. Systematics due to the MHT/MET cut	127
26	E.3. Systematics due to the dead ECAL cut	128
27	E.4. Systematics due to the lepton and photon vetoes	129
28	Bibliography	145
29		

Chapter 1.

1 Introduction

2 The key factor in mankind's success is the ability to abstract, experiment, quantify and
3 learn from our surroundings and experiments. Over time this ability have improved,
4 from making fire to shaping stones and metal to form tools. This understanding of
5 our surroundings now allows us to harness energy directly from nuclear processes. Our
6 understanding is built upon rigorous mathematical foundation, we can successfully
7 describe the motion of planets, stars and galaxies using General Relativity (GR) and the
8 interactions of the fundamental particles are described by the Standard Model (SM) of
9 particle physics.

10 However our understanding is incomplete, we are currently unable to produce a
11 combined description of gravity and the interactions of fundamental particles. Some
12 model which describes both of these regimes must exist. Our current best model, the
13 SM predicts no dark matter, which has been conclusively inferred from cosmological
14 observations, for example the rotational curves of the M33 galaxy[2] show that the amount
15 of visible mass is not enough to confine the stars at the edges given their velocities as
16 shown in Figure 1.1

17 So far it is unknown if we are on the correct track with our descriptions of the universe
18 at high energies and short time scales, experimentally our theories are supported, however
19 one can only guess at how nature works outside of our experimental range. With this in
20 mine the Large Hadron Collider (LHC) was designed and built, to test our theories and
21 search for the missing components of the SM at previously unattainable energy scales.

22 The LHC its self is a particle accelerator and collider, two counter rotating beams
23 of protons are collided at four interaction points around it's circumference, at design
24 capacity these collisions occur every 25 ns or at a rate of 40 million times per second.

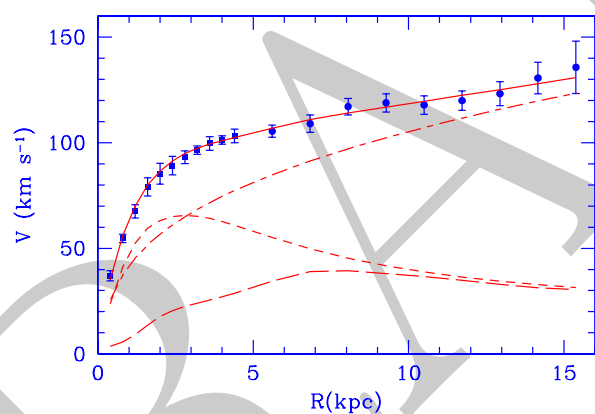


Figure 1.1.: M33 rotation curve (points) compared with the best fit model (continuous line). Also shown the halo contribution (dashed-dotted line), the stellar disk (short dashed line) and the gas contribution (long dashed line), from [2].

1 The accelerator is situated in the Large Electron-Positron Collider (LEP)[] tunnel at
 2 CERN on the Franco-Swiss border. At 27 km in circumference it is the largest machine
 3 on the earth, it is constructed from 1624 niobium-titanium magnets, cooled to 1.8 K
 4 which produce a maximum field strength of 8.36 T, this magnetic field is used to bend
 5 the trajectories of the proton beams so they move in a circular path.

6 Protons are to be collided at a design centre of mass energy of 14 TeV, however design
 7 energy has not yet been realised, instead two runs, one at 7 TeV and the other at 8 TeV
 8 have been performed. The beams are collided to give an instantaneous luminosity of up
 9 to $1 \times 10^{34} \text{ cm}^{-2} \text{ s}^{-1}$, with a maximum instantaneous luminosity of $\approx 5 \times 10^{33} \text{ cm}^{-2} \text{ s}^{-1}$
 10 delivered during the 2012 run.

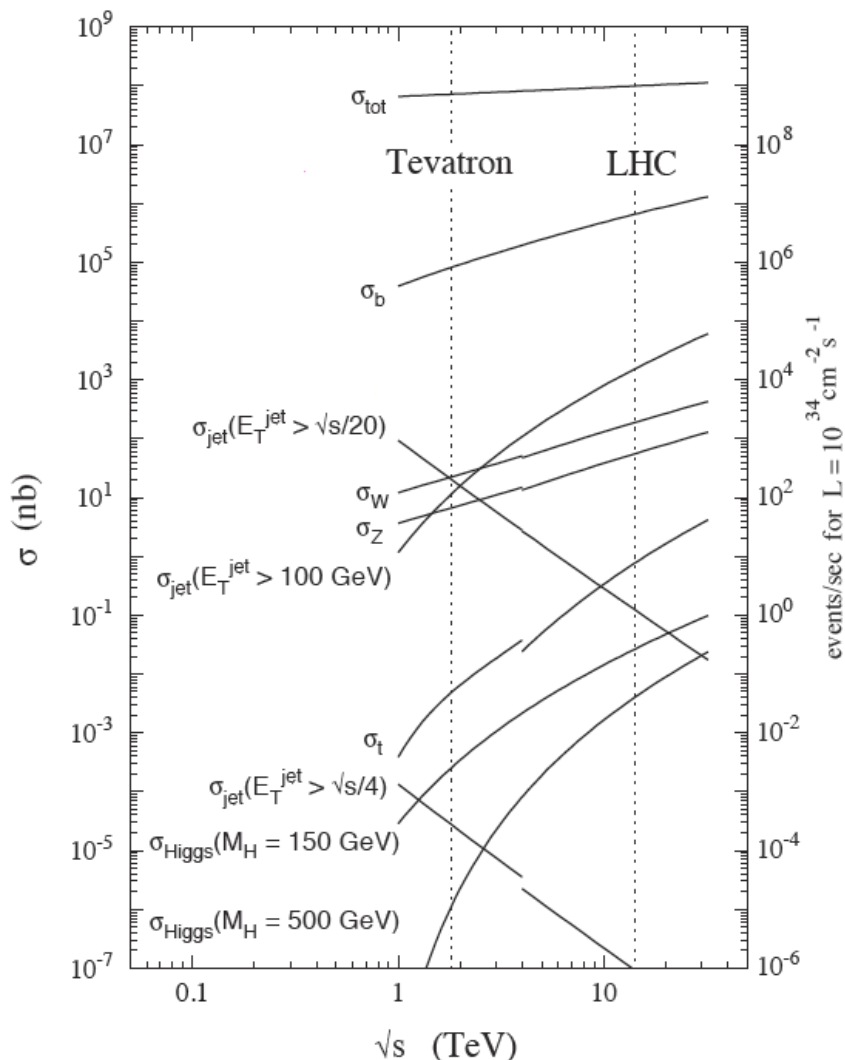


Figure 1.2.: Production cross sections for SM processes and Higgs production for various Higgs masses.

Figure 1.2 shows the production cross sections of SM and Beyond the Standard Model (BSM) processes. To disentangle the already discovered physics low p_T physics from electro-weak and new unseen processes requires highly sophisticated particle detectors, four of which are employed at CERN for the LHC. These consist of two general purpose detectors ATLAS[3] and CMS[4] which is described in detail in Chapter 3. The other two detectors are specialised LHCb[5] is designed to charge-parity violation in the b sector and perform precision measurements of the SM and the ALICE[6] experiment designed to study the quark-gluon plasma when the LHC is running in it's secondary mode and colliding lead ions.

The low production cross sections for “interesting” new events mean that choosing which events to write out for later analysis and which events to dump is highly important and requires complex algorithms. The thesis covers triggering and event selection for a search for beyond the standard model physics that produces a dark matter candidate particle, as well as the analysis of the data collected. In the absence of discovery limits are set on the production cross section and mass scale of new physics models.

Chapter 2.

¹ Theory

² 2.1. The Standard Model (SM)

³ The SM of particle physics seeks to describe all of the observed matter particles and
⁴ their interactions. The theory is a quantum field theory which is both invariant under
⁵ local gauge transform and renormalisable. The theory is constructed from the unitary
⁶ product group $SU(3) \otimes SU(2)_L \otimes U(1)_Y$ where $SU(3)$ describes the colour charged
⁷ strong nuclear force and $SU(2)_L \otimes U(1)_Y$ describes the electro-weak interactions. The
⁸ electro-weak sector contains bosons which exhibit mass, which is contrary to what is
⁹ inferred by the invariance under local gauge transform, that the gauge bosons should
¹⁰ be massless. The $SU(2)_L \otimes U(1)_Y$ symmetry is thus seen to be broken, this is achieved
¹¹ by the addition of a scalar field with a non-zero vacuum expectation value, the extra
¹² degrees of freedom introduced by this scalar field allow the electro-weak bosons to gain
¹³ mass without breaking the local gauge invariance of the Lagrangian. The method was
¹⁴ proposed by Englert, Brout, Higgs, Guralnik, Hagen and Kibble [] but is shortened to
¹⁵ the “Higgs” mechanism and the resulting mediator is known as the Higgs boson (H).

¹⁶ The SM matter particles have spin (1/2) and obey Fermi-Dirac statistics, they exist
¹⁷ in three families of quark and lepton doublets. The force carrying particles have spin
¹⁸ (1) except for the H which is predicted to have spin (0), the bosons obey Bose-Einstein
¹⁹ statistics. Figure 2.1 shows the hierarchy of the standard model particles and the
²⁰ couplings between them.

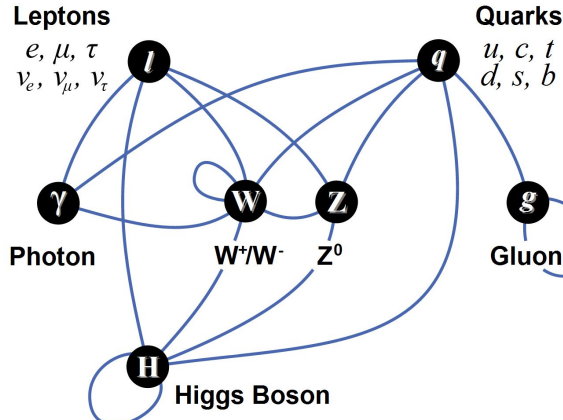


Figure 2.1.: caption

2.1.1. Gauge Invariance

The example of adding a local gauge term to the free Dirac Lagrangian is chosen to show the effects of requiring a system to be invariant under local gauge transform. It is to be noted that natural units are used throughout ($c = \hbar = 1$). The free Dirac Lagrangian is written as

$$\mathcal{L} = i\bar{\psi}\gamma^\mu\partial_\mu\psi - m\bar{\psi}\psi, \quad (2.1)$$

under a simple global phase transform $\psi \rightarrow e^{i\theta}\psi$ and $\bar{\psi} \rightarrow e^{-i\theta}\bar{\psi}$ the exponents cancel and we are left with an invariant system. However if $\theta \rightarrow \theta(x)$ there is a θ dependant term introduced when evaluating the derivative which destroys the invariance of the system:

$$\partial_\mu(e^{i\theta}\psi) = i(\partial_\mu\theta)e^{i\theta}\psi + e^{i\theta}\partial_\mu\psi. \quad (2.2)$$

This infers that an extra term is added to the Lagrangian, i.e

$$\mathcal{L} \rightarrow \mathcal{L} - (\partial_\mu\theta)\bar{\psi}\gamma^\mu\psi \quad (2.3)$$

for convenience we set $\lambda(x) = -\frac{\theta(x)}{q}$ where q is the charge/coupling of the particle we can re-express the Lagrangian as

$$\mathcal{L} \rightarrow \mathcal{L} + (q\bar{\psi}\gamma^\mu\psi)\partial_\mu\lambda(x) \quad (2.4)$$

when demanding that the entire Lagrangian is invariant under local transform one must add a term to cancel the additional term in Equation (2.4), we take

$$\mathcal{L} = [i\bar{\psi}\gamma^\mu\partial_\mu - m\bar{\psi}\psi] - (q\bar{\psi}\gamma^\mu\psi) \mathbf{A}_\mu \quad (2.5)$$

where \mathbf{A}_μ is some new field which transforms as

$$\mathbf{A}_\mu \rightarrow \mathbf{A}_\mu + \partial_\mu\lambda(x) \quad (2.6)$$

This property of \mathbf{A}_μ means that the Lagrangian is now invariant to the additions of a local phase or gauge. However \mathcal{L} must include a term for the free field \mathbf{A}^μ

$$\mathcal{L} = \frac{-1}{16\pi} \mathbf{F}^{\mu\nu} \mathbf{F}_{\mu\nu} + \frac{1}{8\pi} m_A^2 \mathbf{A}^\nu \mathbf{A}_\nu \quad (2.7)$$

for the Lagrangian to remain invariant m_A must equal zero. Hence requiring that the Dirac Lagrangian be invariant under local phase or gauge transform requires the addition of a massless vector field \mathbf{A}_μ giving the full Lagrangian as

$$\mathcal{L} = [i\bar{\psi}\gamma^\mu\partial_\mu\psi - m\bar{\psi}\psi] - \left[\frac{-1}{16\pi} \mathbf{F}^{\mu\nu} \mathbf{F}_{\mu\nu} \right] - (q\bar{\psi}\gamma^\mu\psi) \mathbf{A}_\mu. \quad (2.8)$$

- ¹ Equation (2.6) shows the choice of gauge, in this case the electro-magnetic potential
- ² does not change the system. This addition of a local phase invariance to the free Dirac
- ³ Lagrangian generates all electro dynamics.

The difference between the addition of a global phase and a local phase arises from the calculation of the derivatives of the fields

$$\partial_\mu\psi \rightarrow e^{-iq\lambda(x)} [\partial_\mu - iq(\partial_\mu\lambda(x))] \psi \quad (2.9)$$

here rather than picking up a phase factor we pick up a term involving $\partial_\mu\lambda(x)$, this can be removed by replacing ∂_μ in the full Lagrangian by the covariant derivative

$$\mathcal{D}_\mu \equiv \partial_\mu + iq\mathbf{A}_\mu \quad (2.10)$$

- ⁴ this replacement cancels the extra term in Equation (2.9). This substitution of \mathcal{D}_μ is an
- ⁵ elegant method for promoting a globally invariant Lagrangian to a locally invariant one.

¹ 2.1.2. Electro-weak symmetry and interactions

² If we take the example show in Section 2.1.1 which describes the effects of requiring that
³ the Lagrangian for a free Dirac particle is invariant under local gauge transformation
⁴ infers the existence of a massless gauge field, which is responsible for the photon and the
⁵ electrodynamic interactions.

If we expand this so that rather than considering the Dirac equation for one free particle we consider two free particles, the requirement for invariance under local gauge transform describes not only the interaction with the gauge field but also the inter particle interactions. In this case the covariant derivative \mathcal{D}_μ is expressed as:

$$\mathcal{D}_\mu \equiv \partial_\mu + iq\boldsymbol{\tau} \cdot \mathbf{A}_\mu \quad (2.11)$$

⁶ this promotes us to the $SU(2)_L \otimes U(1)_Y$ regime where there are a total of four gauge
⁷ fields, $\boldsymbol{\tau}$ represents the three Pauli matrices and \mathbf{A}_μ represents three gauge fields, these
⁸ three gauge fields and the mixing with the gauge field seen in $U(1)_Y$ are responsible for
⁹ the W and Z bosons and the photon. However as shown before the requirement for the
¹⁰ whole Lagrangian including the terms for the free gauge fields to be invariant under local
¹¹ gauge transform forces these gauge fields to be massless.

¹² 2.1.3. Quantum Chromo Dynamics

The component which the scribes the strong force is the $SU(3)$ term in $SU(3) \otimes SU(2)_L \otimes U(1)_Y$. A similar gauge invariance is required of the $SU(3)$ group as is required in the previous sections. However the gluon mass is already set to zero by nature so this is not a broken symmetry. The eight gauge fields represent the eight colour combinations of gluons. The tensor in the Lagrangian is given by

$$F^{\mu\nu} \equiv \partial_\mu \mathbf{A}^\nu - \partial^\nu \mathbf{A}_\mu - 2q (\mathbf{A}^\mu \times \mathbf{A}^\nu) \quad (2.12)$$

where the cross product is given by

$$(\mathbf{B} \times \mathbf{C})_i = \sum_{j,k=1}^8 f_{ijk} \mathbf{B}_j \mathbf{C}_k \quad (2.13)$$

¹³ this cross product contains the self interaction of the gluon.

2.1.4. The Higgs and Electro-weak Symmetry Breaking

It has been shown that the choice of representing the SM as a gauge invariant Lagrangian for the $SU(3) \otimes SU(2)_L \otimes U(1)_Y$ group product naturally gives the inter-particle couplings, interaction fields and the force carrying bosons. It has also been shown in [7] that these gauge invariant theories are renormalisable. However as shown in Section 2.1.1 the mass terms of the free fields are not locally gauge invariant, whilst this is not a problem for the photon or gluons as their masses are set to zero by nature, it is a problem for the W and Z bosons which are massive [8, 9]. To break the electro-weak symmetry and give the W and Z mass a scalar field with a non-zero vacuum expectation value is introduced in to the Lagrangian[10, 11]. This field is known as the Higgs field, it breaks the symmetry of the $SU(2) \otimes U(1)$ group, introducing an extra degree of freedom which can be used to give the bosons mass, the breaking method also predicts the now observed[12, 13] Higgs boson.

2.2. Beyond the Standard Model.

The SM does a good job of describing the fundamental particles, their interactions and the generation of fundamental mass. However it is not a full description of the observed physics in the universe.

Firstly whilst the theory is invariant under special relativity, it is not invariant under general relativity and as such provides no description of the gravitational interactions of the fundamental particles. Secondly the amount of Charge-Parity (CP) violation predicted by the SM is not sufficient to account for the observed matter dominance in the universe.

There are also problems in the neutrino sector where the SM predicts that the neutrino is massless, however due to the observation of flavour changing the neutrino mass must be non-zero. The most glaring short coming other than the lack of a description of gravitational dynamics is the lack of a dark matter candidate. This dark matter candidate needs to be heavy, stable, chargeless, colourless and interact via the weak nuclear force only. Such particles are predicted by SuperSymmetry (SUSY) models which also provide a description of gravity. These models insert a further broken symmetry between bosons and fermions, i.e. for each SM boson there is a SUSY fermion and visa versa.

2.2.1. The Constrained Minimal Super Symmetric Model

Whilst there are a plethora of SUSY models, in order to compare the CMS searches against previous and contemporary experiments the CMSSM is chosen as a bench mark, however there are compelling reasons to study the CMSSM it's self. SUSY introduces 105 new parameters to the existing 19 of the SM, effectively sampling a space this large is prohibitive, instead the CMSSM reduces the number of free parameters to 5 these are: $\tan\beta$, where β is the ratio of the vacuum expectation values for the two Higgs fields; m_0 and $m_{1/2}$ which are the mass values for the boson and fermion states at the unification scale; A_0 which is the SUSY breaking tri-linear coupling; finally the sign of μ which is the Higgs breaking parameter.

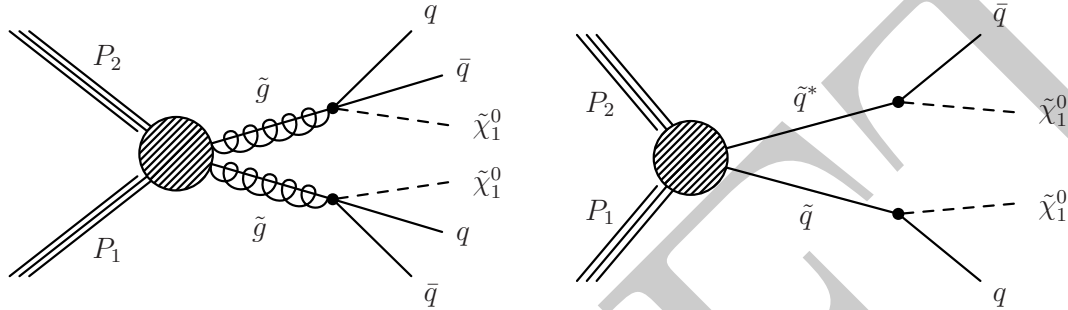
Through out the accessible regions of these values both electro-weak and strong production methods are predicted as well as a multitude of final states involving a stable dark matter candidate particle χ_0 and standard model particles. For the interpretation of the analysis presented in this thesis, limits are set as a function of m_0 and $m_{1/2}$ with fixed values for the other variables of $\tan\beta = 10$, $A_0 = 0$ and $\mu > 0$. Before LHC start up the preferred values for m_0 and $m_{1/2}$ as given by [?] were well defined and with in reach of the early LHC SUSY searches.

2.2.2. Simplified Models

[14] An alternative to searching for a specific beyond the standard model Lagrangian and it's associated physical manifestation is to build a set of self consistent models of new physics which are characterised by production and decay topology, most generally the type of the pair produced particle (quark like or gluon like) and the mass splitting between this parent particle and the final state weakly interacting massive particle which provides a dark matter candidate. This method has several advantages over searching for a specific model:

- If a discrepancy with the SM is found the amount of collected data during early running of the LHC will be insufficient to confirm or rule out specific models of new physics.
- Generalised limits on decay topologies can be applied to many models and are useful for guiding model building.

- 1 • Difficult to search for decay topologies such as those with small mass splittings can
 2 be investigated and analyses turned to these areas of kinematic phase space.



(a) Production and decay of the T1 simplified model with the process $pp \rightarrow \tilde{g}\tilde{g} \rightarrow q\bar{q}\tilde{\chi}_1^0\bar{q}\bar{q}\tilde{\chi}_1^0$
 (b) Production and decay of the T2 simplified model with the process $pp \rightarrow \tilde{q}\tilde{q} \rightarrow q\tilde{\chi}_1^0\bar{q}\tilde{\chi}_1^0$

Figure 2.2.: Simplified model production and decay diagrams.

3 The models considered by this analysis require fully hadronic final states. Two
 4 production topologies are considered. Gluino-gluino production which is pictured in
 5 Figure 2.2(a) is referred to as T1 type models, where any suffix labels the flavour that
 6 the final state particles are forced to. T1 decays to four light (u,d or c) quarks and two
 7 $\tilde{\chi}_1^0$ particles. Squark-squark production, pictured in Figure 2.2(b) is referred to as T2
 8 type production, again any suffix denotes the flavour of the final state quarks. The decay
 9 topology involves two $\tilde{\chi}_1^0$ particles and two final state quarks which hadronise to form
 10 jets.

Chapter 3.

1 The CMS detector

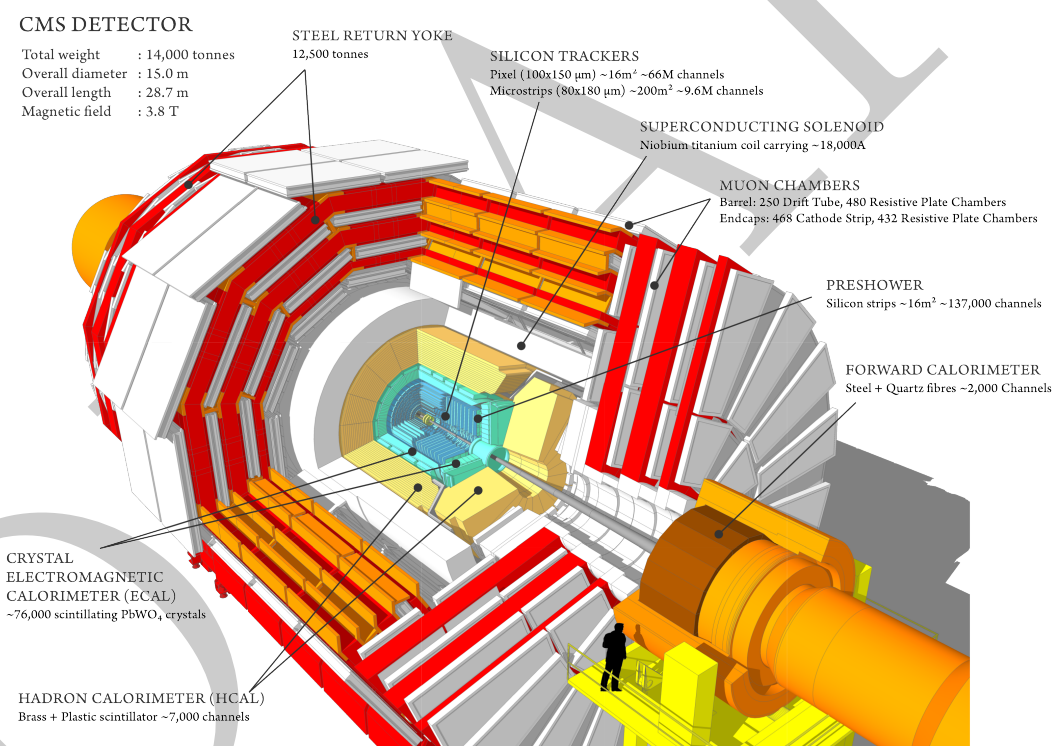


Figure 3.1.: A perspective view of the C.M.S detector[15].

2 The CMS detector was designed and built to study proton-proton interactions at the
3 LHC with the aim of discovering the Higgs boson and searching for beyond the standard
4 model physics signals. The detector is a traditional onion layer design with high precision
5 tracking detectors nearest the interaction point and high energy resolution calorimetric
6 detectors in the outer layers. Due to the predicted presence of missing energy \cancel{E}_T in new
7 physics models, energy measurement over the full η range is required. As alluded to in the
8 name the possibilities of the new physics models containing muons and the “golden” Higgs

¹ decay channel $H \rightarrow ZZ \rightarrow \mu\mu\mu\mu$, and Z' models the detector was designed to accurately
² reconstruct muons with p_T of up to 1 TeV. Due to the prevalence of lepton signals and
³ the ability to distinguish these leptons from the large amount of hadronic fragmentation
⁴ caused by smashing two protons together at a centre of mass energy of 14 TeV the CMS
⁵ Electromagnetic calorimeter was also designed to have precise energy measurement and
⁶ fine grain spatial resolution, this design feature was motivated by the Higgs decay channel
⁷ $H \rightarrow \gamma\gamma$. The other new feature of CMS is the use silicon detectors throughout for particle
⁸ tracking these give precise track reconstruction abilities and the associated fine grain
⁹ resolution in both position and momentum. All the sub-detectors save the muon system
¹⁰ are contained within the barrel of a 4 T superconducting solenoid. This magnet provides
¹¹ the particle track bending required for momentum and lepton charge measurement. In
¹² this section the key detector elements and their design parameters are discussed.

¹³ 3.1. The Silicon Tracker

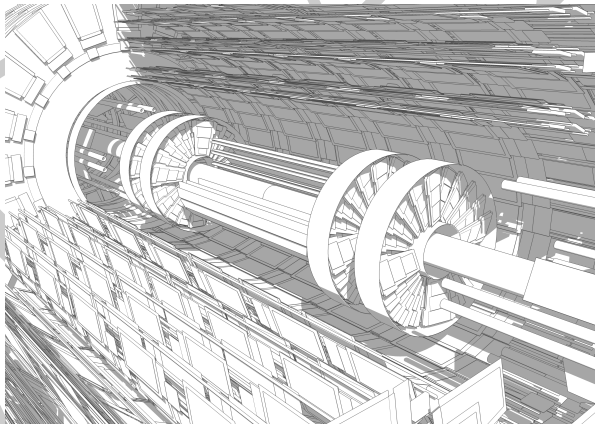


Figure 3.2.: The CMS tracking system, pixel detectors are situated at the centre of the detector closest to the interaction point, surrounded by layers of silicon strip detectors[15].

¹⁴ The design goal for the CMS tracking system was to produce a system that can
¹⁵ precisely and efficiently measure the trajectories of charged particles produced in LHC
¹⁶ collisions. The tracking system surrounds the collision point and has a length of 5.8 m
¹⁷ and a diameter of 2.5 m. At the LHC's design instantaneous luminosity of $10^{34} \text{ cm}^{-2} \text{ s}^{-1}$
¹⁸ an average of 1000 charged particles from more than 20 proton-proton interactions will
¹⁹ be produced per 25 ns bunch crossing. This imposes the requirements of high granularity
²⁰ so that the individual particles and their trajectories can be distinguished and a fast

1 response so that the hits can be assigned to the correct bunch crossing. The technical
2 implications of these requirements imply both a large amount of on-detector electronics
3 and their associated cooling equipment. This large amount of tracker material increases
4 the multiple scattering, bremsstrahlung, photon conversion and nuclear interactions of
5 the particles which are traversing the tracking system, this in turn limits the position
6 and energy resolution of the calorimeter systems. A compromise between the material
7 budget of the tracking system, the desired features and the requirement for the tracking
8 system to have an expected life time of 10 years in a high radiation environment, this
9 resulted in the construction of the tracking system using only solid state silicon detector
10 technology.

11 The CMS tracking system is formed of a pixel detector with three layers situated
12 between 4.4 cm and 10.2 cm of the interaction point and a silicon strip tracker with 10
13 barrel layers extending outwards to a radius of 1.1 m from the interaction point. The
14 barrel layers of both the pixel and strip detectors are complimented by layers of either
15 pixel or strip disks which extend the acceptance of the tracker to $|\eta| < 2.5$. The resulting
16 structure is that of a detector with 200 m^2 of active silicon which makes the CMS tracker
17 the largest detector of its type ever constructed.

18 The individual pixels that comprise the pixel detector are $100 \times 150 \mu\text{m}^2$ which
19 corresponds to an occupancy of around 10^{-4} per bunch crossing. The detector cell size for
20 the microstrip detectors at a radius between 20-55 cm is $10 \text{ cm} \times 180 \mu\text{m}$ which leads to
21 an average occupancy of 2-3%. Further out at a radius greater than 55 cm the minimum
22 cell size is increased to $25 \text{ cm} \times 180 \mu\text{m}$ with an occupancy of around 1%. The tracker
23 performance is extensively documented in [16].

24 **3.2. The Electromagnetic Calorimeter (ECAL).**

25 The CMS electromagnetic calorimeter[17] is a hermetic homogeneous calorimeter con-
26 structed from lead tungstate (PbWO_4) crystals. The ECAL is split into two parts, a
27 barrel covering $|\eta| < 1.479$ read out by avalanche photodiodes and the two end-caps
28 covering $1.479 < |\eta| < 3.0$, read out by vacuum photo-triodes.

29 Lead tungstate crystals were chosen because of their short radiation length, fast
30 scintillation and radiation hardness. During the research and development program
31 it was shown that radiation damage does not affect the scintillation method or the

¹ uniformity of the emitted light yield along the crystal, it only effects the transparency
² through the creation of colour centres. This will be monitored throughout the lifetime of
³ the ECAL via a light injection system[18].

⁴ The barrel crystals have a front face of $22 \times 22 \text{ mm}^2$, this corresponds to the Moliere
⁵ radius of $\approx 22 \text{ mm}$; with a length of 230 mm giving a each crystal length of $25.8X_0$ where
⁶ X_0 is amount of material required for 68% of an electromagneticly interacting particle's
⁷ energy to be radiated in the form of bremsstrahlung or pair production whilst traversing
⁸ that material for lead tungstate this length is $X_0 = 0.89 \text{ cm}$. They are arranged in 36
⁹ super-modules, forming two half barrels. The crystal axes are skewed at 3° with respect
¹⁰ to the vertex and each covers 1° in ϕ and η

¹¹ The endcap crystals are arranged in two semi-circular ‘Dees’, groups of 5×5 crystals
¹² are canter-levered on a aluminium backing plate. The crystals are again skewed with
¹³ regard to the interaction vertex, however they are arranged in an $x - y$ grid rather than
¹⁴ a $\phi - \eta$ grid. The crystal dimensions are different to the barrel, in that the cross section
¹⁵ is $28.6 \times 28.6 \text{ mm}^2$, with a length of 220 mm corresponding to 24.7 radiation lengths

¹⁶ The crystals are read out with avalanche photo-diodes in the barrel region which
¹⁷ covers $|\eta| < 1.479$ and with vacuum photo-triodes in the endcap region which covers
¹⁸ $1.479 < |\eta| < 3.0$.

¹⁹ In addition to the ECAL there is a pre-shower detector situated at $1.653 < |\eta| < 2.6$,
²⁰ this provides identification of isolated electrons against electrons produced in showers,
²¹ each particle passes though the detector leaving a minimum ionising track, or hit, the
²² number of these hits per area gives information on the isolation of the particle and
²³ improves the position measurement of electrons and photons in the ECAL endcaps.

²⁴ Figure 3.3 shows the change in response of the ECAL during running, due to the
²⁵ formation of colour centres, this response is measured using laser light at 440 nm and is
²⁶ used to correct the energies recorded in data during each run to form a uniform response.
²⁷ The ECAL performance in 2011 is extensively documented in [20].

²⁸ 3.3. The Hadronic Calorimeter (HCAL).

²⁹ The design of the CMS HCAL is constrained by the size requirements of fitting the
³⁰ tracking system, ECAL and HCAL inside the solenoid magnet. The HCAL is situated
³¹ between the ECAL which ends at a radius of 1.77 m and the solenoid which starts

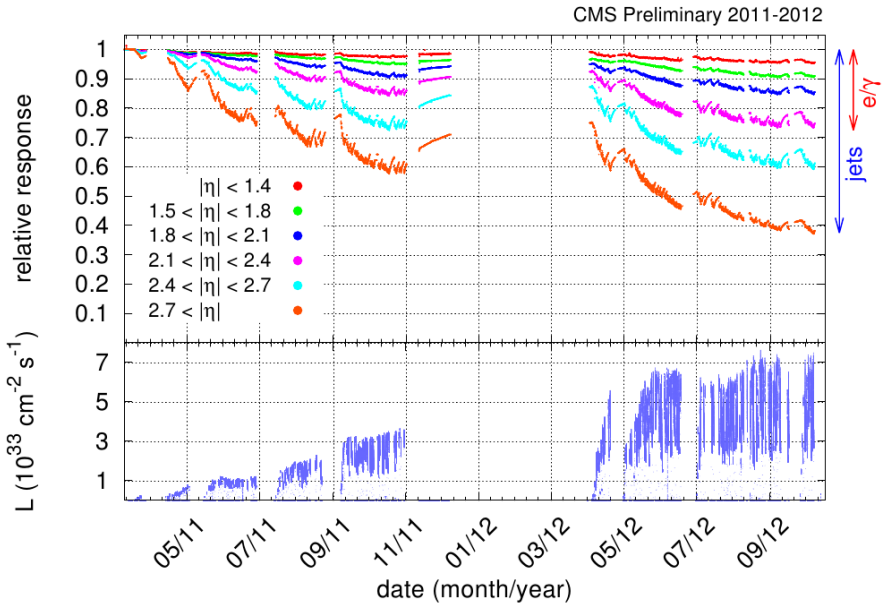


Figure 3.3.: Relative response to laser light (440 nm) measured by the ECAL laser monitoring system, averaged over all crystals in bins of pseudo-rapidity, for the 2011 and 2012 data taking periods. The response change observed in the ECAL channels is of the order of a few percent in the barrel, while it reaches up to 25% in the most forward endcap regions used for electron and photon reconstruction. The response change is up to 60% in channels closest to the beam pipe. These measurements are used to correct the physics data.

The bottom plot shows the instantaneous LHC luminosity delivered during this time period.[19]

1 at a radius of 2.95 m. This constraint limits the amount of material which can be
 2 put in place to fully contain the hadronic showers. To overcome this an outer lay of
 3 instrumentation is placed outside of the magnet and cryogenic system to fully contain
 4 hadronic showers. The full containment of the hadronic objects is necessary for precise
 5 missing energy measurement, which is a key discriminatory feature for new physics
 6 models with undetectable final state particles.

7 The hadronic calorimeter is split in to three sub detectors, the hadronic barrel (HB)
 8 $|\eta| < 1.3$, hadronic endcaps (HE) $1.3 < |\eta| < 3.0$ and a forward calorimeter (HF)
 9 $3.0 < |\eta| < 5.5$.

10 The HB and HE are comprised of layered tiles of brass absorber plates interspaced
 11 with scintillator plates which are read out by wavelength shifting fibres. The total
 12 absorber thickness varies between 5.2 and 10.6 interaction lengths, the ECAL adds
 13 approximately one extra interaction length. The scintillators are segmented in to towers

¹ of area $\Delta\eta \times \Delta\phi = 0.087 \times 0.087$ in the barrel and $\Delta\eta \times \Delta\phi = 0.17 \times 0.17$ in the endcaps.
² The light produced and in the scintillators is merged in the wavelength shifting fibres
³ and then read out using hybrid photo-diodes. The HF is constructed from radiation hard
⁴ quartz fibres, this enables the detector to survive in the very forward regions of the
⁵ detector where high levels of radiation are experienced.

⁶ The hadronic outer (HO) which is situated outside the solenoid used the solenoid
⁷ coils as an extra absorber adding extra interaction lengths in the barrel region ensuring
⁸ full containment of hadronic showers. The HO is constructed from layers of scintillator
⁹ tiles, the light from which is then merged in the wavelength shifting fibres and read out
¹⁰ using hybrid photo-diodes. HCAL performance is documented in [?].

¹¹ 3.4. The CMS Super-Conducting Solenoid

¹² The requirement for precise muon momentum measurements for muons with $p_T > 1$ TeV
¹³ infers the requirement of large bending power, this requirement forces the choice of a
¹⁴ superconducting magnet. The CMS magnet is 13 m long, has an inner diameter of 6 m
¹⁵ and provides a 4 T magnetic field, which gives a bending power of 12 Tm before the muon
¹⁶ bending angle is measured by the muon system. The bore of the solenoid contains the
¹⁷ tracking and calorimeter systems. The magnet is constructed from Niobium-Titanium
¹⁸ superconductor embedded in an aluminium stabiliser is coiled in four layers resulting in
¹⁹ 220 t of cold mass. This is then cooled to around 4 K using liquid helium and a current
²⁰ of ≈ 20 kA is applied to generate the magnetic field.

²¹ 3.5. The CMS Muon system.

²² The CMS muon system is designed to provide accurate muon p_T measurements ($\sqrt{p_T}/p_T <$
²³ 0.1) for muons over a large p_T range. Due to the cylindrical nature of the solenoid, the
²⁴ muon system is also designed to be cylindrical. The muon system has three purposes the
²⁵ first is the identification of muons, secondly the momentum measurement of these muons
²⁶ and thirdly to provide information to the trigger system. The muon system uses three
²⁷ types of gaseous detectors for particle tracking and identification, in the barrel region
²⁸ where the magnetic field is uniform, drift chambers (DT) are used, these cover the region
²⁹ $|\eta| < 1.2$ and are interspaced between the layers of the magnetic flux return plates. In the

1 end cap regions where the muon and background rates are higher and the magnetic field
 2 is non-uniform, cathode strip chambers (CSC) are used due to their fast response,
 3 radiation hardness and fine grain segmentation, the CSCs cover $0.9 < |\eta| < 2.4$. Due to
 4 the initial uncertainty on the background rates and the 25 ns bunch crossing intervals
 5 expected when the LHC is running under design conditions a complementary dedicated
 6 muon triggering system consisting of Resistive Plate Chamber (RPC) was added in the
 7 range $|\eta| < 1.6$, the RPCs provide a fast, independent and fine grain system for which to
 8 trigger on muon objects in the harshest of running conditions.

9 Due to multiple scattering and the sheer quantity of detector material before the first
 10 muon station momentum measurement using the muon system only is accurate to a level
 11 of $\approx 10\%$ below 200 GeV and accurate to a level of 15 – 40%, $|\eta|$ dependant for 1 TeV
 12 muons, when including the tracker information in the muon momentum measurement
 13 the resolution is improved to $\approx 1\%$ below 200 GeV and to about 5% for 1 TeV muons.
 14 The performance of the CMS muon system is detailed in [21].

15 3.6. The Level-1 Trigger System.

16 The CMS trigger system is designed in two levels, the first, the Level-1 trigger is built
 17 using custom electronics and is designed to reduce the input rate of 40 million events
 18 per second to a manageable rate of 100 thousand events per second. Information only
 19 from the calorimeter and muon systems are considered as the time required to read
 20 out the tracking information is prohibitive at this level. Two separate trigger systems,
 21 one performing triggering on the calorimeter system, the other performing triggering on
 22 the muon systems are employed. For a detailed discussion of the calorimeter triggering
 23 algorithms and their performance see Chapter 4. The information from these two sub
 24 triggers is passed to the global trigger, where the decision to accept the event or not
 25 is made. The muon trigger considers information from each of the DT, CSC and RPC
 26 muon systems. Tracks are created from the hits in each of the sub systems and fitted,
 27 the muon momentum is then calculated from the radius of curvature of these muons,
 28 the four highest p_T muon candidates are then passed to the global trigger. Electron and
 29 photon candidates are created by the regional calorimeter trigger, the GCT creates jet
 30 candidates, energy and missing energy sums, the four highest E_T jet candidates of each
 31 type (central, tau and forward), the energy sums and the electron/photon candidates
 32 are then passed to the global trigger where the final trigger decisions are made. These

¹ decisions can require information from a single detector or can require cross objects such
² as the requirement of an energy sum value and a muon.

³ 3.7. The High Level Trigger System.

⁴ The high level trigger system is constructed from off the shelf components. The system is
⁵ composed of two sets of machines, the first are the Event Builder (EB) units, these build
⁶ raw data in to regional chunks from the data read out at the front end of the detector
⁷ when a Level-1 accept is received, this is then combined and transmitted to the Event
⁸ Filter cluster. The EB units transfer the data to the (EF) units via a standard TCP/IP
⁹ gigabit ethernet link. The task of the HLT EF units is to run complex reconstruction
¹⁰ algorithms using combined detector information to reduce the data rate accepted by the
¹¹ Level-1 trigger to a manageable rate, the original design anticipated an output rate of
¹² 100 events per second, however in 2012 running 1000 events per second were stored, half
¹³ of this rate was assigned to the prompt reconstruction queue, the other half was stored
¹⁴ for reconstruction during the long shut down of the LHC in 2013-2015.

¹⁵ The EF farm is formed from standard rack-mounted PC units with a total of approx-
¹⁶ imately 1000 computing cores operating at a clock frequency of around 2 GHz. Upon
¹⁷ receiving an event, each unit performs the CMS reconstruction, the same software frame-
¹⁸ work is used as for offline analysis meaning that the objects used for trigger decisions
¹⁹ are as close in performance to the offline objects as possible, this increases the over all
²⁰ trigger efficiency, however the calibrations used at HLT level are not the final derived
²¹ version. Trigger chains are designed so that full event reconstruction can be performed,
²² however when constructing a trigger that requires full tracking reconstruction steps are
²³ made so that if a given requirement is failed at a lower stage of the reconstruction then
²⁴ time is not wasted performing the full reconstruction. The EF farm is connected to a
²⁵ large (several hundred terabytes) storage area network, this acts as a temporary storage
²⁶ area for the events accepted by the HLT before the events are transferred to the tier-zero
²⁷ reconstruction farm which is located at the central CERN site.

Chapter 4.

1 Level-1 Calorimeter Trigger

2 In this chapter the Level-1 calorimetric triggers are detailed and their performance
3 is measured with respect to various offline quantities which are defined to match the
4 HLT level objects. The performance is measured under evolving pile-up conditions, the
5 impacts of analyses evolving to use pile-up corrected offline variables are measured with
6 respect to Level-1 quantities. Finally a method for reducing the impact of pile-up on
7 Level-1 trigger rate without directly raising the trigger thresholds is studied and the
8 change in performance due to this change is then studied.

9 The nomenclature for the Level-1 trigger algorithms is as follows L1_AlgoType Threshold
10 for example L1_HTT150 refers to a Level-1 trigger requiring $H_T > 150$ GeV.

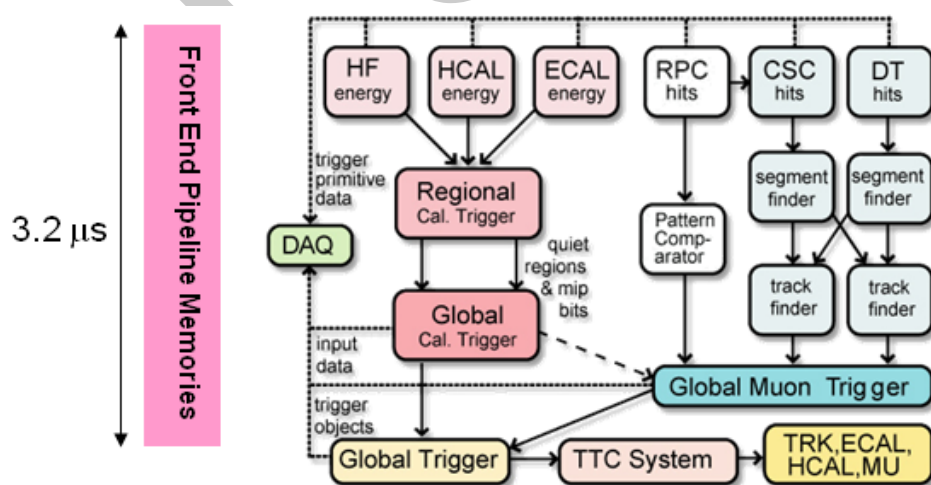


Figure 4.1.: The CMS Level-1 Trigger system.

¹ The CMS Level-1 trigger system[22] is a pipelined dead-timeless system based on
² custom-built electronics. The Level-1 trigger is a combination of several sub systems,
³ which are interconnected as depicted in Figure 4.1.

⁴ Coarse information from the electromagnetic, hadronic and forward calorimeters is
⁵ processed by the Regional Calorimeter Trigger (RCT), this is then passed to the Global
⁶ Calorimeter Trigger (GCT) where the coarse grain information is clustered in to physics
⁷ objects, these objects are then passed to the Global Trigger where the Level-1 accept
⁸ decision is made. Due to the limited size of the pipe line this Level-1 accept must be
⁹ issued within 4.0 μs .

¹⁰ The objects passed from the GCT to the GT include electro-magnetic objects, both
¹¹ electrons and photons as due to the lack of tracking information at the Level-1 trigger
¹² these objects are indistinguishable, jets and energy sums.

¹³ The RCT generates up to 72 isolated and non-isolated electro-magnetic objects, these
¹⁴ are sorted by rank, which is equivalent to transverse energy E_T . The four highest ranked
¹⁵ electro-magnetic objects are then passed via the GCT to the GT at an equivalent data
¹⁶ rate of 29 Gbs^{-1} per type.

¹⁷ Hadronic objects under go two clustering steps. First the transverse energy sums of
¹⁸ the ECAL and corresponding HCAL towers are calculated, the towers are then summed
¹⁹ in to 4×4 trigger regions, these are passed to the GCT at a data rate of 172.8 Gbs^{-1} .
²⁰ These trigger regions are clustered in to jet candidates by the GCT and ranked. The jets
²¹ are then sub-divided in the categories depending on their pseudo-rapidity and the result
²² of τ identification.

²³ Energy sums come in two forms, the total transverse energy E_T which is the scalar
²⁴ sum of all transverse energies and the total jet transverse energy H_T which is calculated
²⁵ as the scalar sum of all jets above some programmable threshold.

²⁶ The missing energy equivalents of these \cancel{E}_T and \cancel{H}_T are formed from the negative
²⁷ vector sum of the objects considered for the transverse sums.

²⁸ 4.1. Level-1 Trigger Jet Algorithm

²⁹ The Level-1 trigger algorithm is detailed explicitly in [23]. The CMS detector can be un-
³⁰ rolled in the ϕ direction to form a rectangular grid of the 396 calorimeter regions, connected

1 along the ϕ edge. The rectangle is formed from 18 ϕ divisions (from $-180^\circ < \phi \leq 180^\circ$)
 2 and 22 η divisions (from $-5 < \eta < 5$). Each ϕ division corresponds to 20° . The η
 3 divisions correspond to $\Delta\eta = 0.5$ in the forward calorimeters and to $\Delta\eta \approx 0.348$ in the
 4 barrel. A pictorial representation of this can be seen in Figure 4.3.

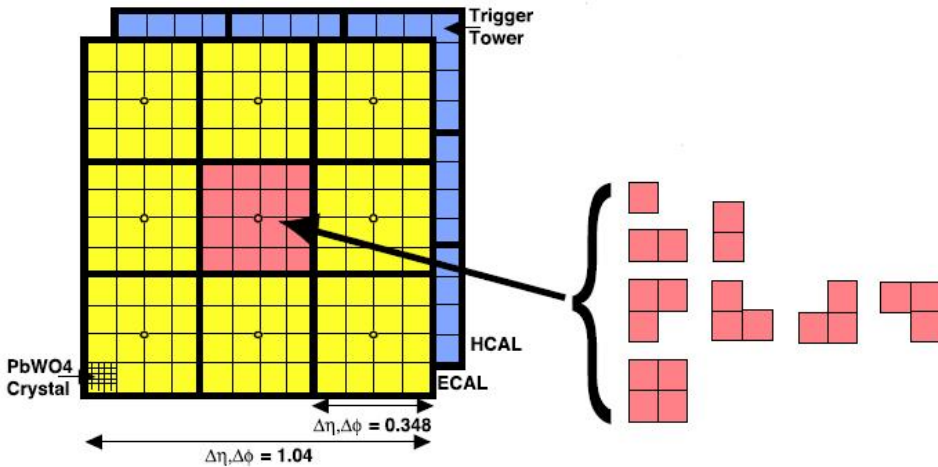


Figure 4.2.: The 3×3 jet-finder window at Level-1. Each cell represents a trigger tower, which is the sum of the HCAL and ECAL transverse energies. The τ -jet veto patterns are shown to the right.

5 A jet candidate is created if the sum of the ECAL and HCAL energies of the central
 6 calorimeter region has an energy deposit larger than all of its neighbours, as shown in
 7 Figure 4.2. The jet is centred at this region where $p_T^{central} > p_T^{surrounding}$ and the transverse
 8 energies of the surrounding regions are summed into the central region. The jet is then
 9 classified as a τ jet if $|\eta| < 3.0$ and none of the τ veto bits are set. If any τ vetoes are set
 10 the jet is classified as a central jet. The jet is classified as forward if $3.0 < |\eta| < 5.0$

11 The τ -vetoes are set by the RCT depending on whether or not the energy depositions
 12 in up to four contiguous trigger towers are below a programmable fraction of the regional
 13 E_T as shown in Figure 4.2. These topologies are due to the hadronic decay mode of the
 14 τ containing one or three isolated pions, any signal that deposits energy in all the trigger
 15 towers in a region is not from one or three isolated pions.

16 It is possible to apply separate jet energy corrections to each of the sub categories of
 17 GCT jets, however at current the same E_T and η dependant corrections are used for all
 18 three jet types.

19 In order to reduce the total data duplicated and shared between the jet finders
 20 the GCT employs a pre-clustering algorithm, which involves 18 jet finders operating

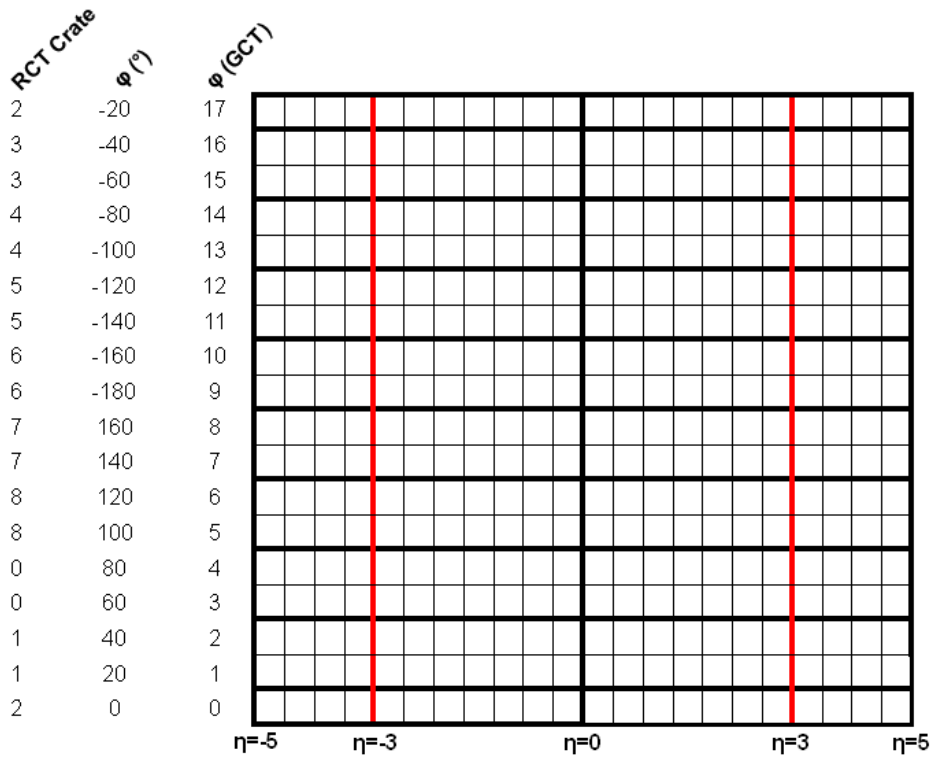


Figure 4.3.: The calorimeter map that the 3×3 jet-finder operates over is made up for 396 calorimeter regions, each jet finder is mapped on to an RCT crate which is composed of an 11×2 strip of these regions. RCT crate labels are shown for negative η only.

1 simultaneously over the whole detector. These jet finders then only share information
 2 with neighbouring regions when the clustered jets are found. Figure 4.3 shows the
 3 boundaries between which the jet finders operate, these map naturally on to one RCT
 4 crate per jet finder. A maximum of 3 jets can be found on each of the ϕ strips acted
 5 on by the jet finders, this gives a maximum of 108 jets per event. In order to preserve
 6 continuity across the $\eta = 0$ boundary, the two adjacent trigger regions are shared between
 7 the jet finders.

8 An example of the jet finding is shown in Figure 4.4. The first step is to create a 2×3
 9 mini cluster around any local maxima found in the 12×2 strip. Equality statements
 10 are imposed so that the energy of the central cell is greater than its neighbours in some
 11 directions and greater than or equal to the neighbours other directions to enforce a gap
 12 of at least one trigger region in both η and ϕ between the centres of the clustered jets.

13 In the second step the jet finder transfers the three largest mini clusters on a given
 14 ϕ strip to the closest ϕ strip on the neighbouring jet finder. These are then compared

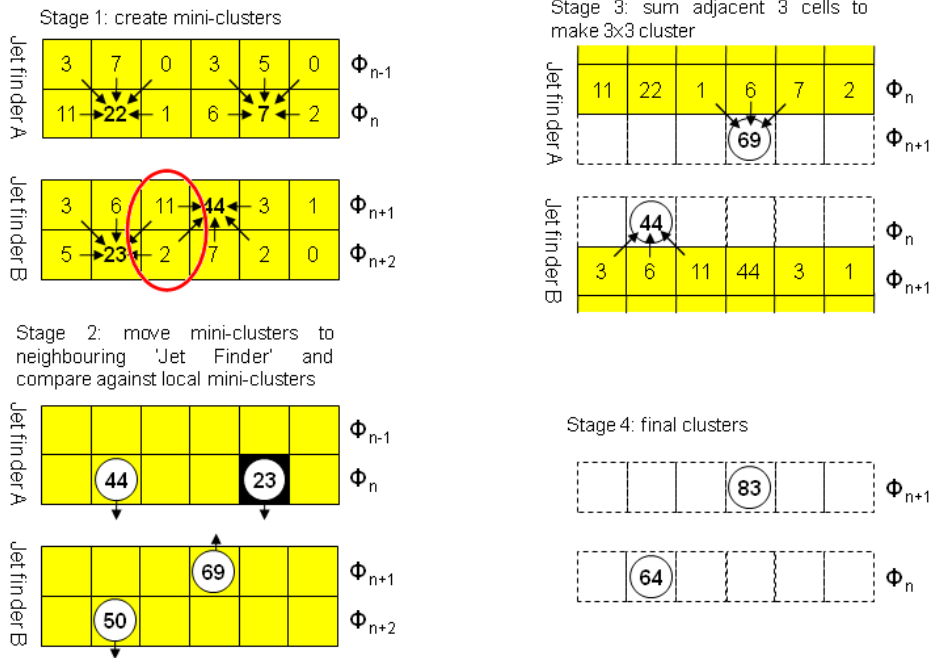


Figure 4.4.: The Level-1 jet clustering method, six cells in η are shown. An example of overlapping jets is shown.[24]

- 1 against the existing mini clusters in that ϕ strip, those that are adjacent or diagonally
- 2 adjacent to a larger mini cluster are removed. The inequality statements are then
- 3 reimposed to prevent problems with clusters having the same energies. In the final stages
- 4 the mini clusters have their three adjacent regions summed in to produce a 3×3 jet
- 5 cluster. Finally the four highest ranked jets are corrected and passed to the GT.

4.2. Level-1 Trigger Performance

- 7 During the start of data taking in 2010, no Jet Energy Corrections (JEC) were applied in
- 8 the Level-1 trigger. This gave a relatively slow turn on in terms of offline hadronic objects.
- 9 During the winter shutdown of the LHC between the 2010 and 2011 running periods a
- 10 set of Level-1 JEC were developed. These corrections used a piecewise cubic form for the
- 11 interpolation function used to correct the jet energy dependant on it's uncorrected E_T
- 12 and η values. However as can be seen in Figure 4.5 these corrections were only applied to
- 13 jets with a raw energy below 130 GeV, the secondary lobe shows those objects that do
- 14 not have their energy corrected.

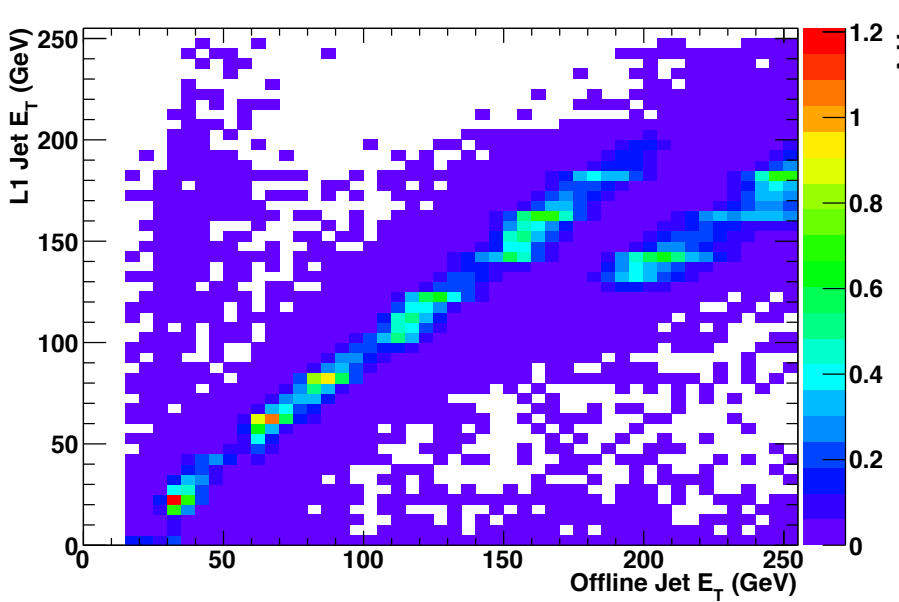


Figure 4.5.: Correlation between offline corrected jet energy and Level-1 corrected jet energy for matched jets. The discontinuity shows where the Level-1 jet corrections do not alter the raw energy of the jet.

1 To overcome this a new set of corrections were derived using a well established tool
 2 for producing offline corrections,

3 **REFERENCE TO tapper-001 here**

4 using the same functional form that was derived for correcting particle flow jets.

5 **REFERENCE TO PF HERE**

6 In this section we discuss the performance of both sets of Level-1 JEC and the
 7 performance of the energy sum and missing energy triggers H_T , $\#_T$, and \cancel{E}_T , the
 8 performance of which are not effected by the application of jet energy corrections at
 9 the Level-1 trigger due to the quantities being built from the internal GCT jets before
 10 they pass through the corrections look up table. The performance is studied under both
 11 low pile up conditions where the mean peak pile up $\langle PU \rangle$ is 16 primary vertices and
 12 under high pile up conditions where $\langle PU \rangle$ is 36 primary vertices.

13 To measure the performance of the Level-1 single jet triggers we assume that the
 14 leading offline corrected anti- $k_t(0.5)$ calorimeter (see Section 6.2.1 for a description of the
 15 offline jet clustering algorithm) jet is the jet that triggered the event. We then match
 16 this offline jet to the closest Level-1 jet in ΔR , where for there to be a match $\Delta R < 0.5$

is required. For this match central, τ and forward jets are considered. Events where the recorded Level-1 energy is set to the overflow bit, meaning they have more than 254 GeV of E_T measured at Level-1 are ignored.

To collect an unbiased sample in which to measure the performance, two methods are used; the first is to require a Minimum Bias trigger, which is triggered by beam induced activity in the CMS detector. However due to the nature of these collisions the number of events with high energy interactions is low and the prescale applied to this trigger further reduces the sample size. However this method does produce the least bias. The second method is to trigger an object that does not deposit significant energy in the calorimeter systems, in this case we choose the muon trigger with the lowest unprescaled p_T threshold. The muon trigger is chosen with some loose isolation requirements to make sure it does not overlap with a jet, causing a discrepancy in the measure of the calorimetric energy. The sample has a higher number of events due to the large amount of bandwidth given to the single object muon triggers in CMS. The use of a muon trigger also serves to increase the precision of the measurement of the Level-1 missing energy trigger as the muons are not seen by the calorimeter system the \cancel{E}_T sample is enriched.

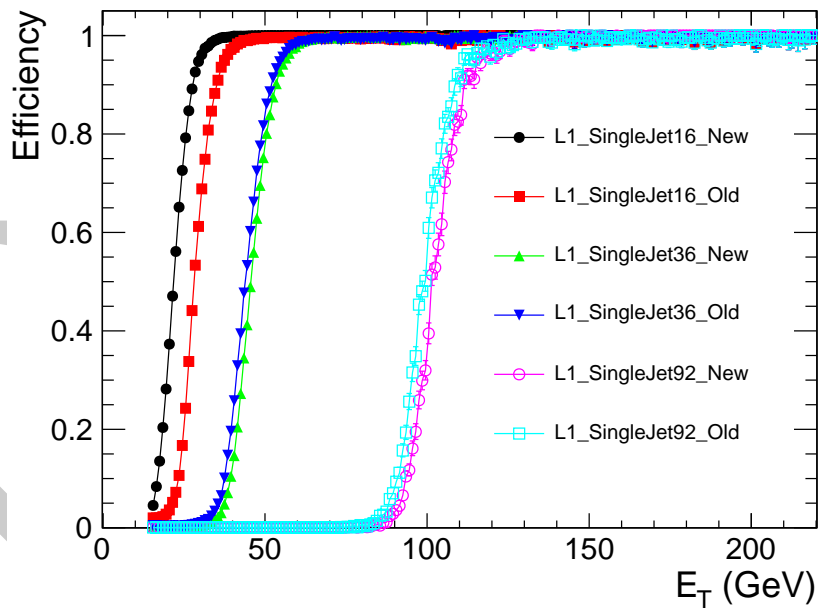


Figure 4.6.: Comparison of the performance of L1_SingleJet16, L1_SingleJet36 and L1_SingleJet92, when using the piecewise cubic corrections and using the new correction scheme. The difference in performance of the two is negligible above 36GeV.

Figure 4.6 shows the performance of the piecewise cubic corrections (PWC) and the performance of the new corrections. The data was taken with the PWC enabled in the GCT hardware. The updated corrections were emulated in the bitwise reproduction of the GCT. The made an event by event comparison possible. At low E_T the new corrections turn on before the PWC corrections, if the new corrections were applied on with no change to the trigger menu, the Level-1 trigger rate would rise. At a threshold of 36 GeV and higher the performance of the two correction schemes is very similar. Due to the small change in observed performance and the ability to correct raw energies above 130 GeV, the new corrections were deployed online after the first machine development period of 2011 and are still online at the end of data taking in 2012.

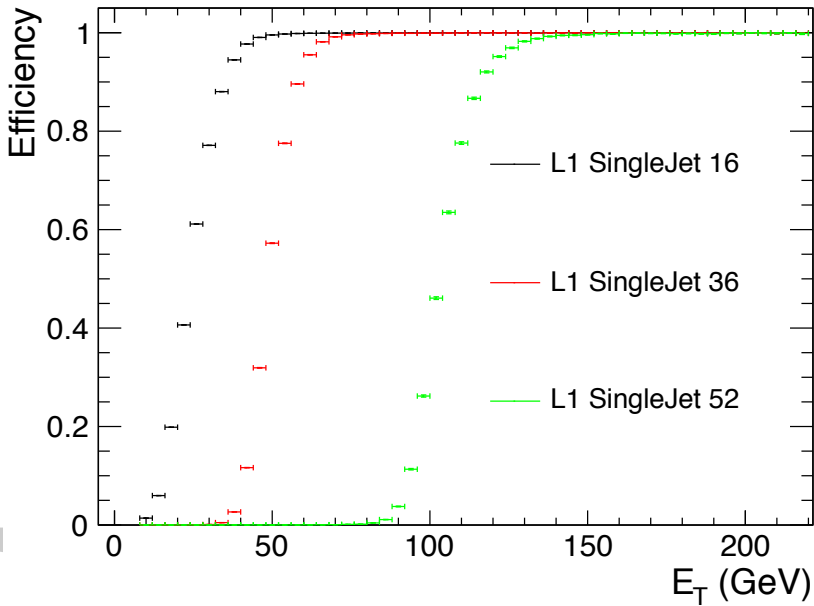


Figure 4.7.: Performance measurements of L1_SingleJet16, L1_SingleJet36 and L1_SingleJet92, when using the new correction scheme deployed in the GCT hardware. The performance is slightly worse than that of the emulated triggers due to a change in pile up conditions between the two data taking periods.

The performance of the updated corrections was then measured with data taken with the corrections applied in the GCT hardware. The reference sample was taken with a trigger requiring an isolated muon with $p_T > 24$ GeV (HLT_IsoMu24_v*). The performance of three example triggers is show in Figure 4.7. The data collected and represented in Figure 4.7 has a peak mean pile up ($\langle PU \rangle$) of 16 interactions, this is higher than the $\langle PU \rangle$ of approximately 8-10 present in Run2011A, on which the previous comparison was performed. The observed difference in the performance of the

1 Level-1 single jet triggers as a function of pile up is a case of concern when data taking
2 is underway at continually increasing luminosity and pile-up conditions.

3 The instantaneous luminosity in 2012 was predicted to be $5 \times 10^{33} \text{ cm}^{-2} \text{ s}^{-1}$, with
4 $\langle PU \rangle \approx 32$. In order to study the effect on the trigger rate and efficiency a high pile
5 up, low instantaneous luminosity, LHC fill was taken in 2011.

6 The Level-1 single jet performance was studied in this run in terms of two offline
7 object definitions. The first was the standard anti- $k_t(0.5)$ calorimeter jet reconstruction,
8 the second was a set of anti- $k_t(0.5)$ calorimeter jets which were corrected for pile up using
9 the fastjet correction algorithm, which is further detailed in Section 6.2.1. The fast-jet
10 corrections remove the energy deposited by the secondary interactions from the objects
11 which are expected to come from the primary hard interaction, thus removing energy from
12 the offline jets. The effect of these pile up corrections on the Level-1 trigger performance
13 is first studied under conditions with $\langle PU \rangle$ of 16, the performance of which has
14 already been measured with respect to non pile up corrected offline objects, as a sanity
15 check. The results are shown in Figure 4.8, the performance is measured with respect
16 to HLT_IsoMu24_v*, in terms of both pile up corrected and standard offline objects. As
17 expected the performance in the two cases is very similar. The same comparison is shown
18 for H_T in Figure 4.9, where the effect of the fastjet[25] corrections is more pronounced
19 due to the sum over jets. The difference between the turn on points for the two offline
20 quantities is on the order of 10 GeV under low pile up conditions.

21 Due to the high pile up fill being a specialised fill with low instantaneous luminosity,
22 the high level trigger paths were disabled, instead Level-1 trigger pass though paths were
23 utilised to take the data. The Level-1 single muon pass though trigger is used to collect
24 the reference sample. Otherwise the same analysis method is common between the two
25 data sets. Figure 4.10 shows the difference in turn on for three example Level-1 single jet
26 triggers when using standard calorimeter jets and fastjet corrected calorimeter jets. In
27 the high pile up conditions the switch to offline jets that are corrected for pile up shifts
28 the turn on point to lower values of E_T , the magnitude of this effect reduces as the Level-1
29 trigger trigger threshold raises. This implies that the same offline performance as seen in
30 the low pile up conditions can be achieved by using the pile up corrected offline objects
31 and raising the Level-1 single jet trigger thresholds.

32 Figure 4.11 shows the same high pile up comparison, but for the Level-1 H_T triggers.
33 Due to the size of the sample the precision of this measurement is low. However the
34 same trend of a shift to lower H_T values of the turn on point of the Level-1 triggers when

1 using pile up corrected offline objects is observed. This again implies that the Level-1
 2 H_T trigger thresholds can be raised whilst preserving the same offline performance as
 3 during the low pile up conditions.

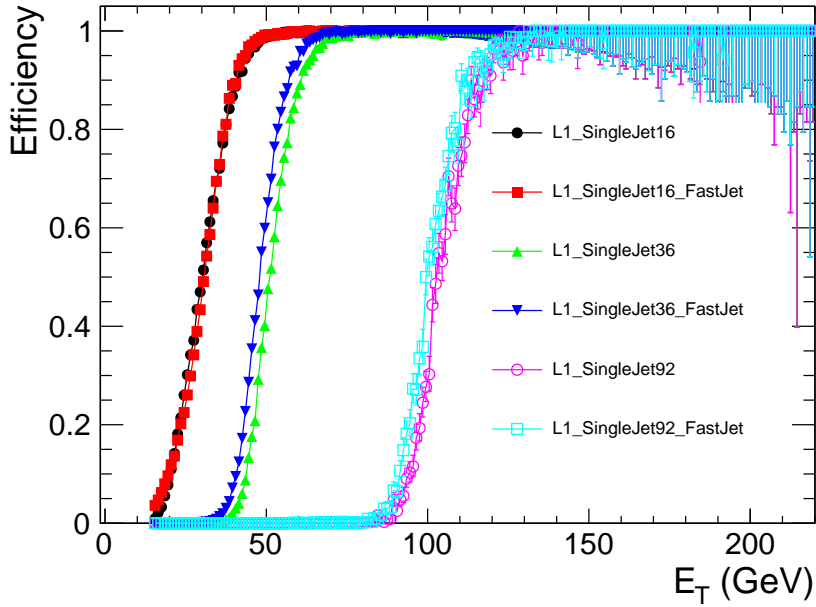


Figure 4.8.: Comparison of the performance of L1_SingleJet16, L1_SingleJet36 and L1_SingleJet92 triggers. Where $\langle PU \rangle = 16$. For two offline reconstruction methods, standard anti- $k_t(0.5)$ calorimeter jets and pile up corrected anti- $k_t(0.5)$ calorimeter jets.

4 The performance of each of the Level-1 triggers is then reported to the analysis users
 5 so that high level trigger paths can be designed with the Level-1 constraints in mind.
 6 These measurements are also used when designing new Level-1 trigger menus where the
 7 requirement for taking the correct data has to be balanced against the total trigger rate
 8 of the Level-1 menu.

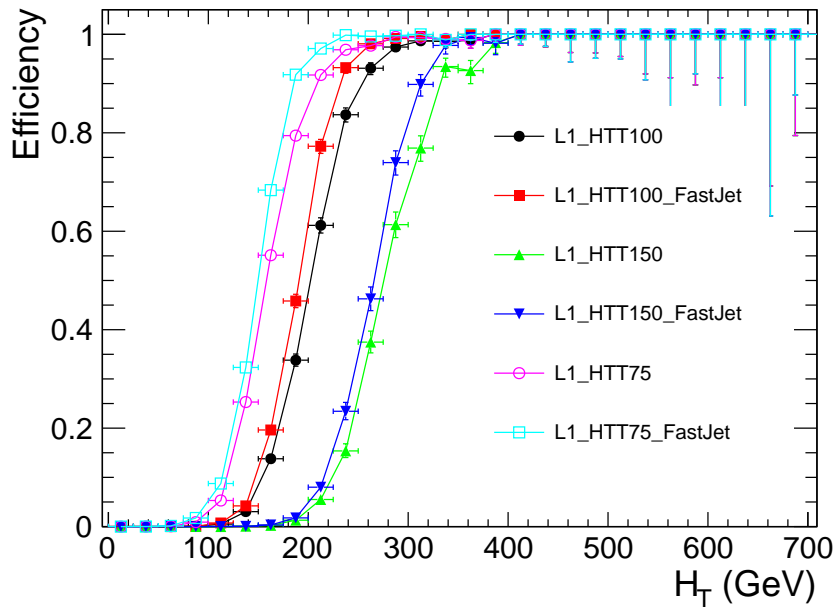


Figure 4.9.: Comparison of the performance of L1_HTT75, L1_HTT100 and L1_HTT150 triggers. Where $\langle PU \rangle = 16$. For two offline reconstruction methods, standard anti- $k_t(0.5)$ calorimeter jets and pile up corrected anti- $k_t(0.5)$ calorimeter jets.

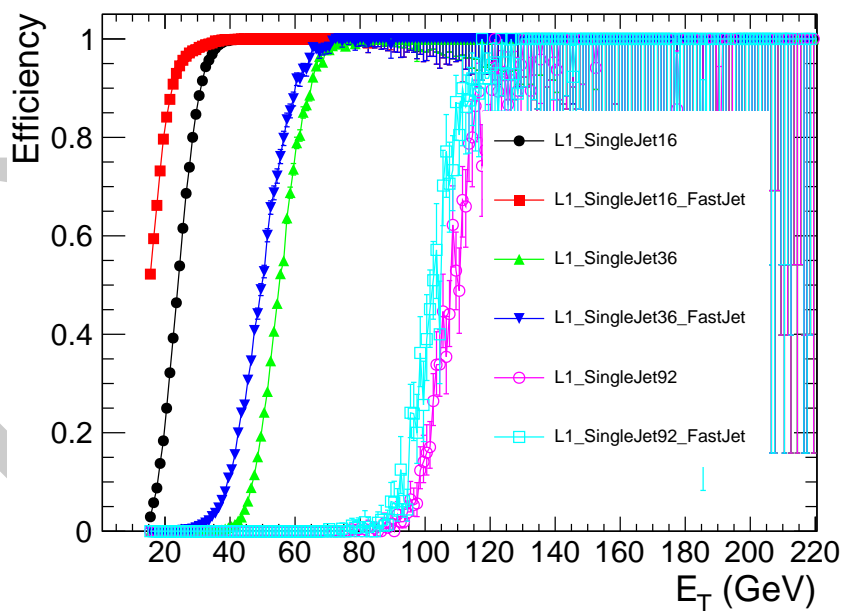


Figure 4.10.: Comparison of the performance of L1_SingleJet16, L1_SingleJet36 and L1_SingleJet92 triggers. Where $\langle PU \rangle = 36$. For two offline reconstruction methods, standard anti- $k_t(0.5)$ calorimeter jets and pile up corrected anti- $k_t(0.5)$ calorimeter jets.

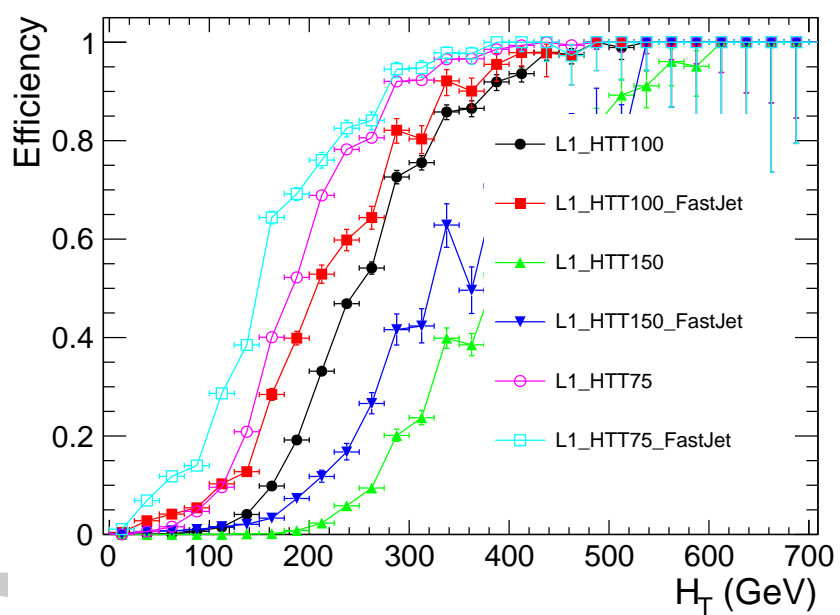


Figure 4.11.: Comparison of the performance of L1_HTT75, L1_HTT100 and L1_HTT150 triggers. Where $\langle PU \rangle = 36$. For two offline reconstruction methods, standard anti- $k_t(0.5)$ calorimeter jets and pile up corrected anti- $k_t(0.5)$ calorimeter jets.

4.3. Level-1 Trigger Pile-up Mitigation

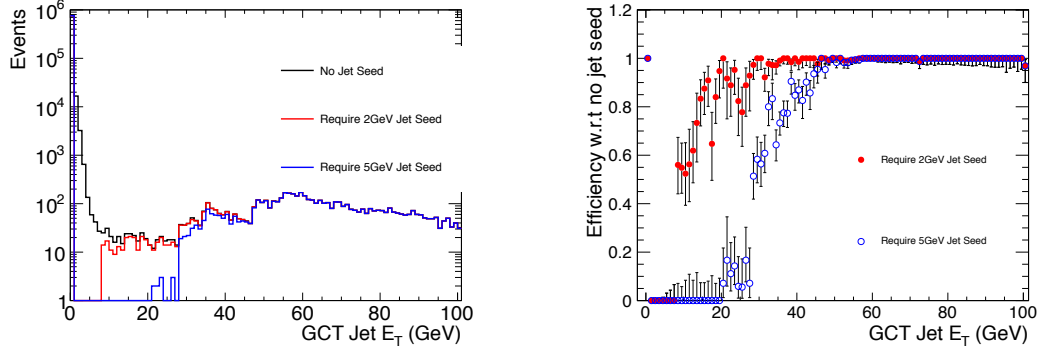
Whilst we have seen that the offline performance of the Level-1 hadronic triggers can be maintained when raising the trigger thresholds to deal with increased rate, when switching to pile up corrected offline objects. Figure 4.14 shows the trigger cross section as a function of instantaneous luminosity for the L1_HTT150 trigger, which requires $H_T > 150$ GeV. However beyond a certain point raising thresholds causes a loss of performance. In this section we look at a method to reduce the effects of pile up hadronic Level-1 triggers, by making an addition to the Level-1 jet finding algorithm.

In Section 4.1 the Level-1 jet clustering algorithm was described. The proposed change was to add a requirement that the seeding region has a direct energy threshold, in addition to the equality relations that are set up. The effects of applying a 2 GeV and a 5 GeV threshold are studied. This threshold is on the raw, uncorrected energy of the trigger regions and effects all Level-1 jets. The impact will be seen in the Level-1 jet triggers which use corrected energy and Level-1 H_T and \cancel{H}_T which are formed from uncorrected jets. The aim is to remove the events which are accepted due to pile up, but not to remove physics events.

The triggers most effected by this change are the energy sum triggers as they sum many jets of low threshold, where as the single object triggers are already cutting on high E_T objects.

Figure 4.12(a) shows the internal GCT uncorrected jet energy spectrum in high pile up conditions, taken with the L1_SingleMu pass though triggers. The three histograms are for; no application of jet seed threshold in black, where there are many low E_T jets; In red a 2 GeV seed requirement is made, the effect is to cut out all jets below 2 GeV and cut out jets with an energy up to approximately 35 GeV of uncorrected energy; The blue histogram shows the jet energy spectrum after applying a 5 GeV seed threshold, the effect is to remove all jets below 5 GeV and to cut out jets with energy up to 55 GeV. Figure 4.12(b) shows the efficiency with respect to the no seed sample for the two test seed thresholds. The removal of jets in the low energy region of the E_T spectrum due to the jet stemming from pile-up rather than collimated objects is where the advantage of applying a seed threshold is seen over simply raising the trigger thresholds, or raising the threshold of jets to be included in the Level-1 H_T or \cancel{H}_T calculation.

To quantify the effects of the addition of the jet seed a low pile up sample, where the effects are expected to be small, is studied in terms of rate reduction and efficiency



(a) GCT internal uncorrected jet E_T distributions for the same events with a 0, 2 or 5 GeV seed requirement.
(b) Efficiency of applying a requirement of 2 or 5 GeV with respect to no requirement.

Figure 4.12.: Effect of requiring a jet seed threshold on GCT internal jets.

1 change. The dedicated high pile up fill is then studied in terms of rate reduction, due to
2 the limited sample size of the high pile up fill the change in efficiency on this sample is not
3 studied. However due to the addition of energy from the secondary pile up interactions
4 the change in efficiency in the low pile up sample is the worse case scenario.

5 Table 4.1 details the rate reduction with respect to the 0 GeV seed threshold for seed
6 thresholds of 2 GeV and 5 GeV for three example triggers, these are:

- 7 • L1_SingleJet50, which requires at least one jet with $E_T > 50$ GeV with in $|\eta| <$
8 3.0;
- 9 • L1_QuadJet38, which requires 4 jets with $E_T > 38$ GeV with in $|\eta| < 3.0$;
- 10 • L1_HTT100, which requires that Level-1 $H_T > 100$ GeV.

11 The rate of L1_SingleJet50 is not effected by the requirement of a 2 GeV seed thresh-
12 old and is reduced by 15% when a 5 GeV seed requirement is made. The L1_QuadJet38
13 trigger rate is reduced by the same amount as the single jet trigger, under low pile up
14 conditions for both seed thresholds. L1_HTT100 sees a 2% rate reduction when requiring
15 a 2 GeV seed threshold and a 3% reduction in rate when requiring a 5 GeV seed.

16 Table 4.2 shows the rate reduction under high pile up conditions with respect to
17 the 0 GeV seed threshold requirement, for the same three example triggers as in the
18 low pile up case. The rate of L1_SingleJet50 is not reduced when making a 2 GeV
19 seed requirement, when making a 5 GeV seed requirement the single jet 50 GeV rate is

Table 4.1.: Summary of rate reduction during low pile up conditions.

Trigger	% rate reduction with a 2GeV requirement	% rate reduction with a 5GeV requirement
L1_HTT100	$3 \pm 11\%$	$3 \pm 11\%$
L1_QuadJet38	$0 \pm 0\%$	$15 + 6 - 8\%$
L1_Jet50	$0 + 0 - 12\%$	$15 + 9 - 15\%$

Table 4.2.: Summary of rate reduction during high pile up conditions.

Trigger	% rate reduction with a 2GeV requirement	% rate reduction with a 5GeV requirement
L1_HTT100	$40 \pm 5.7\%$	$99 + / - 50\%$
L1_QuadJet38	$30 \pm 20\%$	$40 + 22 - 24\%$
L1_Jet50	$0 + 7 - 0\%$	$30 + 10 - 12\%$

¹ reduced by 30%. The rate of L1_QuadJet38 is reduced by 30% when requiring a 2 GeV seed and by 40% when requiring a 5 GeV seed. The rate of L1_HTT100 is reduced by 40% when requiring a 2 GeV seed threshold and when requiring a 5 GeV seed threshold ⁴ the rate is reduced by $\approx 99\%$, however the statistical error on this prediction is large.

⁵ 4.3.1. Effect on trigger efficiency

⁶ Section 4.3 shows that requiring a jet seed threshold substantially reduces the trigger acceptance rate at in high pile up conditions.

⁸ However the aim of requiring a jet seed is to reduce rate, but not at the cost of physics.
⁹ In this section we look at the effects of requiring a seed threshold, whilst requiring some
¹⁰ loose, generic offline selection on the hadronic objects.

¹¹ The change in efficiency is measured under low pile up conditions where the least
¹² extra energy added to the event. This gives a worse case estimate of the effect of requiring
¹³ a jet seed on the offline efficiency.

¹⁴ Each offline reconstructed calorimeter jet must adhere to the following quality criteria:

¹⁵ • Pass loose calorimeter ID[26];

¹⁶ • $p_T \geq 30$ GeV;

¹⁷ • $|\eta| \leq 3.0$;

- ¹ • Matched to a Level-1 jet with $\Delta R \leq 0.5$.

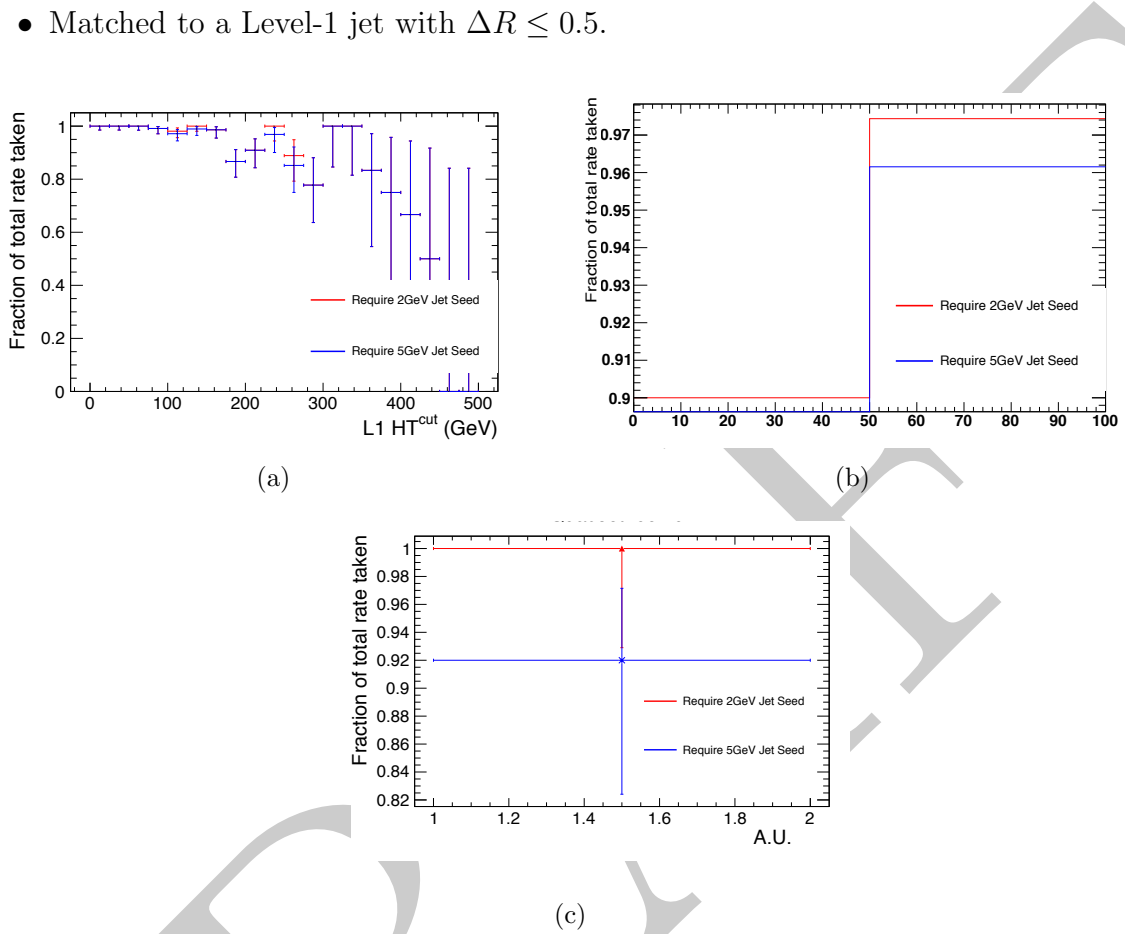


Figure 4.13.: Efficiency reductions for various Level-1 algorithms when applying a 2 or 5 GeV seed tower requirement, in low pile up conditions. Figure (a) shows the efficiency reduction for H_T triggers at low pile up in cut steps of 25 GeV. Figure (b) shows the efficiency reduction for jets with $|\eta| < 3$. and $p_T > 50\text{GeV}$. Figure (c) show the efficiency reduction for a quad jet trigger, with jet $|\eta| < 3$. and $p_T > 38\text{GeV}$.

² 4.3.2. Efficiency of H_T Triggers

- ³ Figure 4.13(a) shows the acceptance reduction after applying the two jet seed thresholds.
⁴ The distribution is the cumulative number of events passing a cut of $L1 HT^{cut}$ in bins of
⁵ 25 GeV. Since H_T is the scalar sum of the jet p_T 's in the event the value of Level-1 H_T
⁶ is reduced as jets are removed from the calculation. To preserve efficiency the Level-1
⁷ trigger threshold will have to be reduced. When comparing to the high pile up rate
⁸ reduction in table 4.2 it is shown that the trigger rate can be reduced by $\approx 20\%$ when

- ¹ requiring a 2 GeV seed threshold and reduced by $\geq 99\%$ when requiring a 5 GeV seed
² threshold, for a trigger threshold of 100 100 GeV.

³ 4.3.3. Efficiency of Jet Triggers

- ⁴ Figure 4.13(b) shows the change in acceptance of jets in low pile up conditions when the
⁵ two seed thresholds are required. The effect is on the order of a few percent for each of
⁶ the thresholds. Requiring a 2 GeV seed reduces the efficiency for jets above 50 GeV by
⁷ $\approx 2.5\%$, whilst requiring a 5GeVseed reduces the efficiency of the same jets by $\approx 4\%$.

⁸ 4.3.4. Efficiency of MultiJet Triggers

- ⁹ Figure 4.13(c) shows that the effect of requiring a seed threshold of 2 GeV has no effect
¹⁰ on the efficiency of the quad jet 38 GeV trigger and requiring a seed threshold of 5 GeV
¹¹ reduces the efficiency of the quad jet 38 trigger by 8%. The change in rate is dramatic in
¹² high pile up conditions where for a 2 GeV seed threshold the rate is reduced by $\approx 30\%$
¹³ and by $\approx 40\%$ when requiring a 5 GeV seed. However it is to be noted that the sample
¹⁴ where this measurement has been made is of limited size, inferring a reasonably large
¹⁵ statistical uncertainty.

¹⁶ 4.4. Summary

- ¹⁷ The effects of requiring a jet seed have been studied using the Level-1 trigger emulator
¹⁸ on high and low pile-up samples. The studies show that requiring a jet seed of 5 GeV
¹⁹ greatly reduces the rate of the H_T and Multi Jet triggers in high pile up conditions,
²⁰ whilst not adversely effecting the data taking efficiency of these triggers.

- ²¹ The cross section of L1.HTT150 has been measured with and with out the addition
²² of a jet seed threshold of 5 GeV as shown in Figure 4.14. Ideally the trigger cross section
²³ would be independent of the instantaneous luminosity and pile up, Figure 4.14 shows
²⁴ that the addition of a 5 GeV seed threshold reduces the dependance on instantaneous
²⁵ luminosity of the trigger cross section.

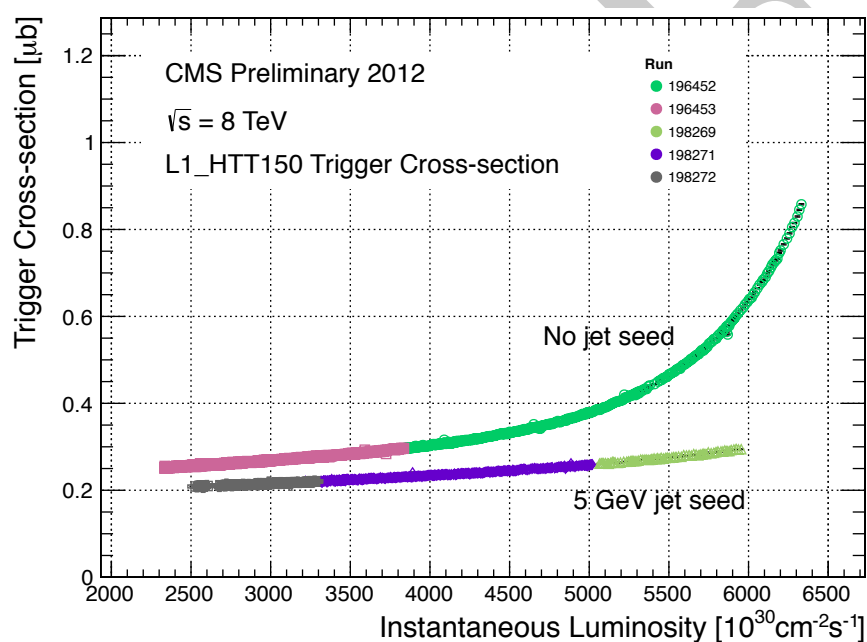


Figure 4.14.: Trigger cross section as a function of number of pile up interactions. Showing that applying a 5 GeV jet seed threshold dramatically reduces the dependance of cross section on the instantaneous luminosity.

Chapter 5.

¹ Motivating the α_T Analysis

² 5.1. The Problem

³ If Supersymmetry or some other beyond the SM theory is to provide a yet undiscovered
⁴ dark matter candidate the Lightest SUSY Particle (LSP), it is predicted that this
⁵ candidate will interact via the weak nuclear force only. This gives a decay topology
⁶ involving missing energy in the form of the dark matter particle escaping the detector.
⁷ Due to the nature of interactions at the L.H.C, these particles would be produced at the
⁸ end of a decay chain of heavy particles that interact strongly, giving a final topology
⁹ involving hadronic objects which are classified as jets for the purpose of analysis and
¹⁰ missing energy. There are several SM processes that mimic this final state.

¹¹ By far the largest of these backgrounds comes from QCD multi jet events where
¹² fake missing energy is introduced either from failures in reconstruction, or stochastic
¹³ fluctuations in the calorimeter systems.

¹⁴ expand on this - E/\sqrt{E} has non gaussian tails. Figures of jets falling below
threshold, missed jets etc. probably from some jet-met paper.

¹⁵ However due to the theoretical errors on the QCD production cross section predicting
¹⁶ the number QCD background events from Montecarlo simulation is not possible. A
¹⁷ secondary QCD background also exists, where due to the requirement of a jet E_T
¹⁸ threshold, multiple jets fall under threshold by a few GeV, this causes a balanced event
¹⁹ to look unbalanced as the jets under threshold are no longer considered. It is these
²⁰ sources of QCD background that α_T is designed to remove.

1 The second major background comes from SM electro-weak decays and is irreducible
2 as the final states involve real missing energy, from neutrinos. The electro-weak decays
3 that form the back ground are $W \rightarrow \tau\nu + \text{Jets}$, where the τ is reconstructed as a jet,
4 or the lepton fails the identification required for the dedicated lepton vetoes, $Z \rightarrow \nu\bar{\nu}$
5 + Jets is completely irreducible. These are generally di-jet topologies. At higher jet
6 multiplicities top quark production followed by semi-leptonic top decay accounts of the
7 largest background. These backgrounds are predicted using a well understood control
8 sample this is fully explained in Section 7.1.

9 The final background source is that introduced by detector failure or electronic noise
10 induced by the movement of the L.H.C proton beam. Approximately 1% of the ECAL
11 read out is not available in offline event reconstruction, this provides a source of fake
12 missing energy.

Chapter 6.

1 Reconstruction and Event selection

2 In this chapter the event reconstruction and selection are defined, the search variable
3 α_T is constructed both as an offline discriminator and as an analysis specific trigger,
4 the performance of this trigger under different data taking conditions is measured with
5 respect to the final event selection.

6 The first performance measurement is performed on the full 5 fb^{-1} of 7 TeV data
7 collected in 2011, this data set is then used for the full analysis presented in this thesis.
8 The performance of a suite of upgraded α_T triggers is then measured on 11 fb^{-1} of 8 TeV
9 data which was collected during the 2012 LHC run. These performance measurements
10 were used in the analysis presented in

11 ref latest paper.

12 6.1. The α_T variable.

13 α_T is inspired by Ref [27] and was expanded to transverse multi jet topologies by members
14 of the CMS collaboration in Refs [28, 29]. The purpose is to provide a variable that can
15 be cut on to eliminate QCD from the final selection. To do this the inherent balance of
16 the QCD system is exploited.

17 For di-jet systems α_T is defined as:

$$\alpha_T = \frac{E_T^{j_2}}{M_T} \quad (6.1)$$

¹ where $E_T^{j_2}$ is the transverse energy of least energetic of the two jets and M_T is defined as:

$$M_T = \sqrt{\left(\sum_{i=1}^2 E_T^{j_i}\right)^2 - \left(\sum_{i=1}^2 p_x^{j_i}\right)^2 - \left(\sum_{i=1}^2 p_y^{j_i}\right)^2} \quad (6.2)$$

For a perfectly measured di-jet system with $E_T^{j_1} = E_T^{j_2}$, where the jets are opposite in ϕ $\alpha_T = 0.5$, for events with back to back jets where one is miss-measured $\alpha_T < 0.5$. However the majority of signals predict many jets in the final state. α_T can be generalised to work with n-jets in the flowing way. The variables H_T , \mathbb{H}_T and ΔH_T are constructed,

$$H_T = \sum_{i=0}^{n \text{ jets}} E_T^{jet_i}, \quad (6.3)$$

$$\mathbb{H}_T = \left| \sum_{i=0}^{n \text{ jets}} \vec{p}_T^{jet_i} \right|, \quad (6.4)$$

² for jets above some predefined threshold E_T which is common for all jet based quantities.
³ The multi jet system is reduced to a pseudo di-jet system by forming two large jets. The
⁴ individual jet E_T 's are summed, with the final configuration being chosen to have the
⁵ minimum difference in energy (ΔH_T) between the pseudo jets. This simple clustering
⁶ criteria provides the best separation between miss-measured events and those with real
⁷ \cancel{E}_T .

α_T is then defined as:

$$\alpha_T = \frac{H_T - \Delta H_T}{2\sqrt{H_T^2 - \mathbb{H}_T^2}} \quad (6.5)$$

⁸ Figure 6.1 shows the α_T distribution for both data and simulated background samples.
⁹ The QCD multi jet background is negligible above an α_T value of 0.55, where as the
¹⁰ standard model processes which involve real \cancel{E}_T exist at all possible values of α_T . Values
¹¹ of α_T in the range $0.5 < \alpha_T < 0.55$ arise in multi jet QCD due to jets falling below
¹² threshold or large stochastic fluctuations. It is to be noted that the discrepancy between
¹³ data and simulation for $\alpha_T \leq 0.55$ is due to no trigger emulation being applied to the
¹⁴ simulated background samples.

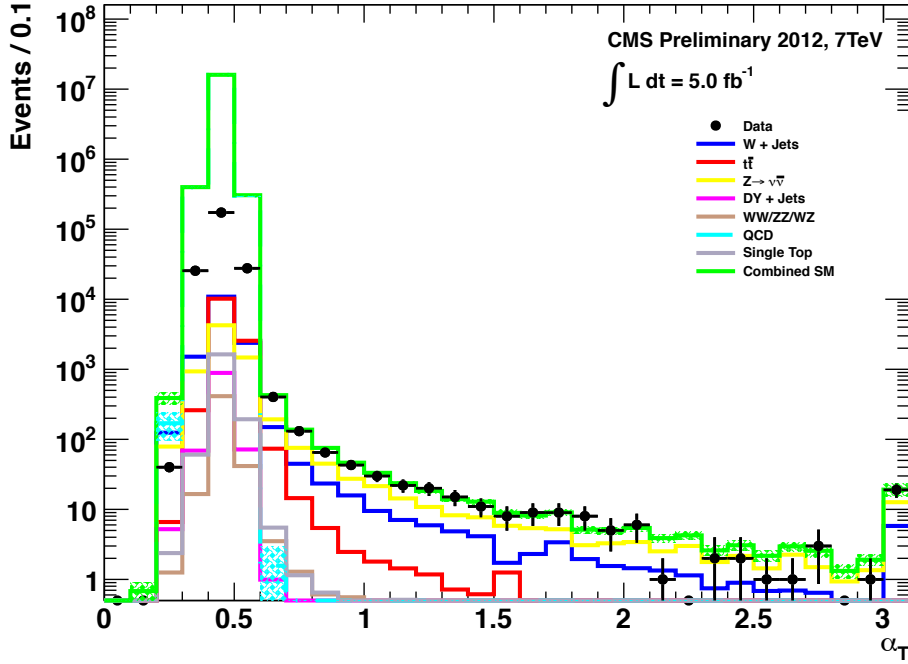


Figure 6.1.: α_T distribution for background and data for the region $H_T > 375$ GeV. Trigger emulation is not applied in the simulated background which leads to the discrepancy in the region $\alpha_T \leq 0.55$. The QCD multi-jet background is reduced to less than one event.

6.2. Event selection

In order to select events for the hadronic signal sample and the muon and photon control samples a common set of section cuts is defined. In this section the objects are defined as are the flow of the analysis cuts and filters.

6.2.1. Preselection of hadronic objects

Hadronic showers are clustered into objects which from now on will be referred to as jets. These jets are formed from the energy deposits recorded in the calorimeter towers. Individual jets are clustered using the anti- $k_t(0.5)$ algorithm[30], for high p_T jets this produces cone like jets, for low p_T jets deviations from the circular geometry are allowed, as shown in Figure 6.2. CMS uses two complimentary reconstruction methods for creating jets, the first uses only calorimeter information, these jets are referred to as anti- $k_t(0.5)$ -Calorimeter jets, the second method adds information from the tracking system to improve the energy resolution and is not used in this analysis due to the

- 1 requirements of using the same objects at both trigger level and offline to preserve data
 2 taking efficiency.

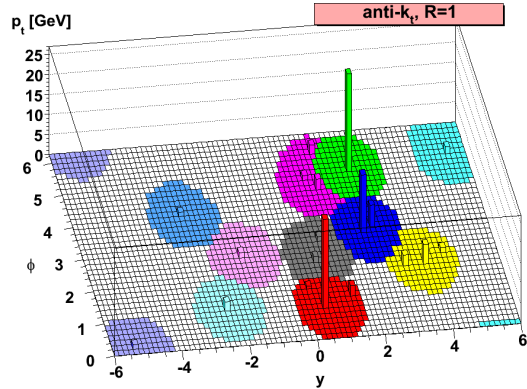


Figure 6.2.: Simulated hadronic objects clustered in to Jets using the anti- $k_t(0.5)$ jet clustering algorithm, note the high p_T green object which causes the low p_T jet in close proximity to be cut off.

- 3 The jets have their raw energies corrected based on their position and momentum to
 4 establish a uniform relative response in η and a calibrated absolute response in transverse
 5 energy E_T , with an associated uncertainty of between 2% and 4% dependant on E_T and
 6 η [31]. Figure 6.3 shows the absolute jet energy scale uncertainty as a function of the jet's
 7 p_T for the jets considered in this analysis.

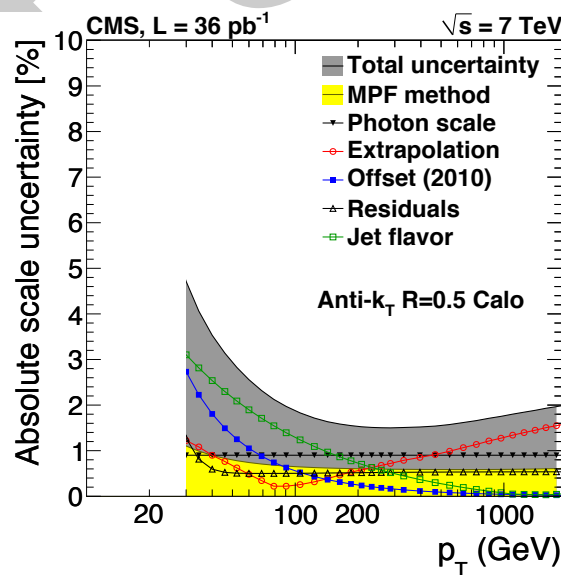


Figure 6.3.: Absolute jet energy scale uncertainty as a function of jet p_T for anti- $k_t(0.5)$ -Calorimeter jets[32].

It is also possible to correct the raw energies of the jets for pile up. Pile up causes energy from secondary interactions to be added to the event, for soft pile up interactions this energy is distributed uniformly though out the detector. Two forms of pile up corrections are used in CMS to correct the energies of calorimeter jets. The first is an offset correction, the raw energy has a constant energy removed though out the detector based on the number of primary vertices in the event. The second method is to calculate per event the average energy deposited in each calorimeter tower using the `FastJet`[25, 33] jet clustering package, this quantity is referred to as ρ and is also used to correct the isolation variables for electrons, muons and photons.

The jets considered in the analysis are not corrected for pile up, each jet is required to have $E_T > 50$ GeV, the highest E_T jet in the events is required to be within tracker acceptance ($|\eta| < 2.5$) and the sub leading jet is required to have $E_T > 100$ GeV. In the lowest two offline H_T bins the jet thresholds are scaled to preserve the jet multiplicity, for the bin $275 \text{ GeV} < H_T < 325 \text{ GeV}$, the jet threshold is 36.6 GeV and the sub leading jet threshold is 73.3 GeV. In the bin $325 \text{ GeV} < H_T < 375 \text{ GeV}$, the jet threshold is 43.3 GeV and the sub leading jet threshold is 86.6 GeV.

The quantities H_T and $\#H_T$ are then formed from these jets.

6.2.2. Electrons

Two complementary algorithms are used at the track seeding stage of the electron reconstruction. Tracker driven seeding which is more suitable for low p_T ($p_T < 5$ GeV) electrons and ECAL driven seeding, which starts at the ECAL and works back towards the interaction point. The ECAL driven seeding starts by creating superclusters[34] which contain information on the lateral shower shape in the η direction of the electron or photon shower and the spread of energy deposits in the ϕ plane for electrons, due to the radiation of photons by the election in the CMS magnetic field. Track seeds from inner tracking layers and electron track are then build from these track seeds. The trajectories are reconstructed using a dedicated modelling of the electron energy loss and fitted with a Gaussian Sum Filter[35]. For the purpose of the analysis an object is defined as an electron if it has $p_T > 10$ GeV, $|\eta| < 2.5$ and passes “VBTF” working point 95 quality criteria[36]. Any event containing an identified electron is vetoed.

6.2.3. Muons

Muon reconstruction at CMS is designed to be regional meaning that the full reconstruction sequence can be run at both the HLT and offline. Regional reconstruction only performs the reconstruction in a small part of the detector meaning that the time taken is short. As an example the amount of information required to reconstruct a muon in the silicon tracker is less than one percent of the entire tracker read out. The regions which are reconstructed at the HLT are seeded by the muon candidates produced by the Level-1 trigger even if these muons did not cause the issue of the Level-1 accept. Global muon reconstruction uses information from both the stand alone muon system and from the silicon tracker and performs a fit to the individual detector hits. Figure 6.4 shows the muon p_T resolution for muons reconstructed using either the muon system only, the tracker only or the global muon reconstruction.

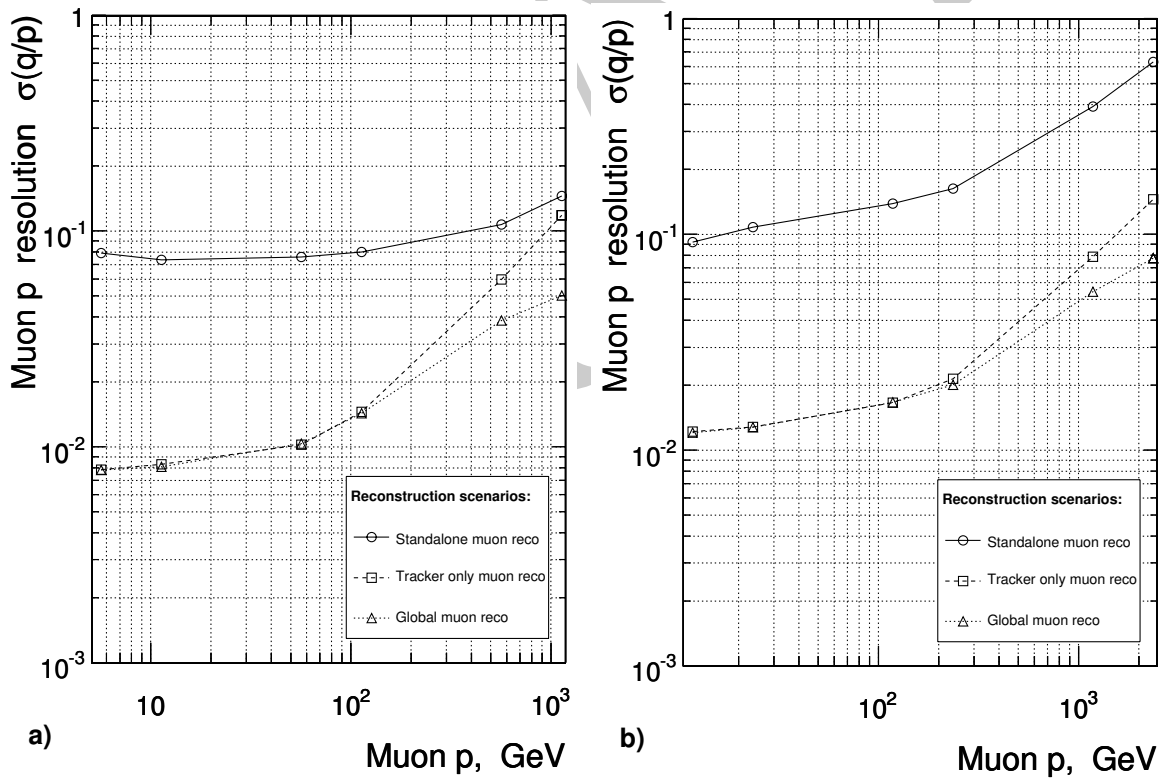


Figure 6.4.: Resolution of $(1/p)$ versus p for standalone, global and tracker-only reconstruction.
a) Barrel, $\eta = 0.5$; b) Endcap, $\eta = 1.5$.[34]

12

13 Signal events are vetoed if they contain a muon with $p_T > 10$ GeV and $|\eta| < 2.5$ that
14 passes the “VBTF” working point 95 for muons [37]. Two separate muon control samples

¹ are defined, one requiring exactly one muon with $p_T > 10$ GeV, the second requiring two
² muons, who's invariant mass sums to the Z mass.

³ 6.2.4. Photons

⁴ Photons are reconstructed in the ECAL using the same methods as used to reconstruct
⁵ elections. However an anti selection is performed on the tracking requirements. For
⁶ photons which do not convert in the tracker a supercluster energy deposit is required with
⁷ no associated electron track, for photons which undergo pair production in the tracker
⁸ material the tracks associated to the super clusters do not originate from the interaction
⁹ vertex, instead they appear in a layer of the tracker. For unconverted photons the ratio of
¹⁰ the energy deposited in the central ECAL crystal to the energy of the surrounding 3×3
¹¹ group of ECAL crystals is used as an identification variable. Signal events are vetoed if
¹² they contain a photon with $E_T > 25$ GeV, $|\eta| < 2.5$ and that passes ID requirements[38].
¹³ A requirement of exactly one photon with $E_T > 150$ GeV with in $|\eta| < 1.45$ is made for
¹⁴ the photon control sample.

¹⁵ 6.3. Common Analysis cuts

- ¹⁶ • **Good run selection**, All detector subsystems on, CMS in “Physics Declared”
¹⁷ mode and all physics object groups have certified the runs and luminosity sections.
¹⁸ This removes any events where the sub-detectors were in an error state or events
¹⁹ from before the tracker was switched to high voltage mode.
- ²⁰ • **P.K.A.M (Previously Known As Monsters) filter**, these events are caused
²¹ by beam-gas interactions close to CMS, which cause a shower of particles to enter
²² the pixel detector along the beam line, resulting in a large proportion of the pixel
²³ detector to record hits.
- ²⁴ • **Vertex Selection** requires at least one non-fake vertex with at least four associated
²⁵ tracks, within a cylinder of radius 2 cm and length 48 cm, centred at $Z = 0$ of the
²⁶ CMS detector.
- ²⁷ • **Hadronic barrel and end-cap noise filter**, this filter removes events where
²⁸ strips of towers in the hadronic calorimeters record energy from electrical noise,
²⁹ mimicking large, unbalanced energy deposits.

- **Vertex $p_T/H_T > 0.1$** , removes events where the sum of the p_T of all tracks from all good vertices is less than 10% of the energy deposited by jets in the calorimeters. This cut is designed to remove events with tracking failure, which would otherwise pass the calorimeter only event quality requirements.
- **Masked ECAL channel filter:** Approximately 1% of the ECAL crystals are masked, or have read out failure. To avoid selecting events with large energy miss measurement, a topological cut was devised. The first step is to calculate $\Delta\phi^*$ for each jet (\vec{j}) in the event, where:

$$\Delta\phi^* = \Delta\phi\left(\vec{E}_T + \vec{j}, \vec{j}\right). \quad (6.6)$$

Which gives a measure of the miss measurement of a jet, if $\Delta\phi^*$ is small, the missing energy points along the jet in the ϕ direction. By selecting the miss measured jet, full position information is preserved. If any jet has $\Delta\phi^* < 0.5$, the number of masked ECAL crystals with in $\Delta R < 0.3$ are summed, if there are more than 10 masked crystals adjacent to the jet, the event is vetoed.

- **$R_{miss} < 1.25$:** The total hadronic energy in an event is required to be greater than 275 GeV which is well above the transverse energy threshold of 50 GeV for each jet. However several jets falling below this threshold can sum to a significant quantity of ignored energy. This is shown in Figure 6.5, here the missing energy calculated from jets in the range $10 \text{ GeV} < E_T < 50 \text{ GeV}$ is shown, whilst requiring that $\cancel{E}_T < 20 \text{ GeV}$. This shows that for a well balanced event the jets below threshold can carry greater than 100 GeV of ignored energy. R_{miss} is defined as H_T/\cancel{E}_T and can be used to single out events where the inclusion of lower momentum jets does significantly improve the balance of the event. Figure 6.6 shows for two H_T regions the R_{miss} distribution after the application of the full cut flow, including α_T , QCD contamination is visible in the signal sample for $R_{miss} > 1.25$.

This cut flow and set of object definitions define the common selection, on top of this an α_T cut is applied, the passing events are then binned in 8 H_T bins, these are 275 GeV - 325 GeV, 325 GeV - 375 GeV, 375 GeV - 475 GeV, 475 GeV - 575 GeV, 575 GeV - 675 GeV, 675 GeV - 775 GeV, 875 GeV - 7 TeV. However the raw number of events in the signal region is meaningless without an accurate background prediction, as discussed earlier taking the background estimation from simulation is not viable due to the requirement of high order theory calculations on the cross sections of SM processes involving jets, these have many divergencies due to the nature of QCD. Instead the

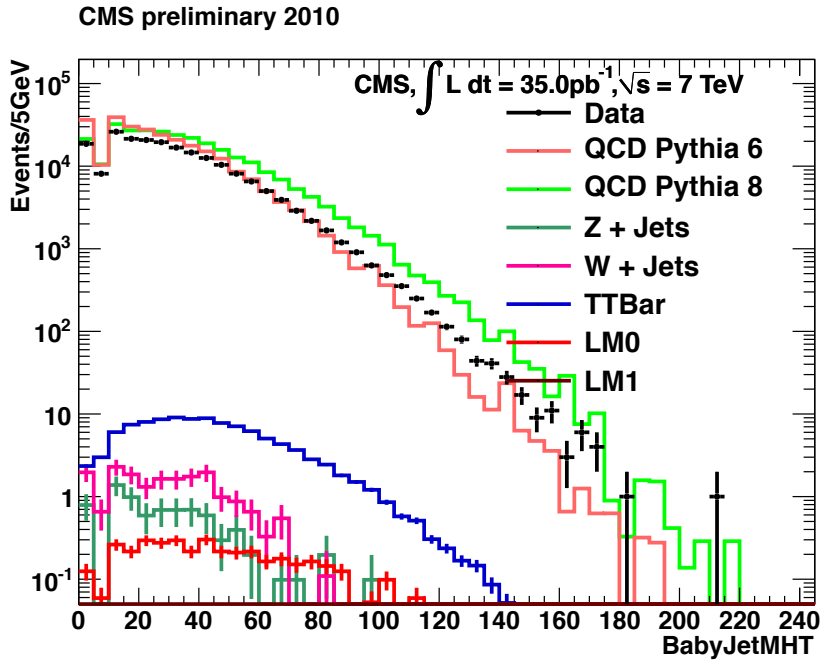


Figure 6.5.: \cancel{H}_T from jets with $10 \text{ GeV} < E_T < 50 \text{ GeV}$ in events with $H_T > 350 \text{ GeV}$ and $\cancel{E}_T < 20 \text{ GeV}$ in 35 pb^{-1} of data.

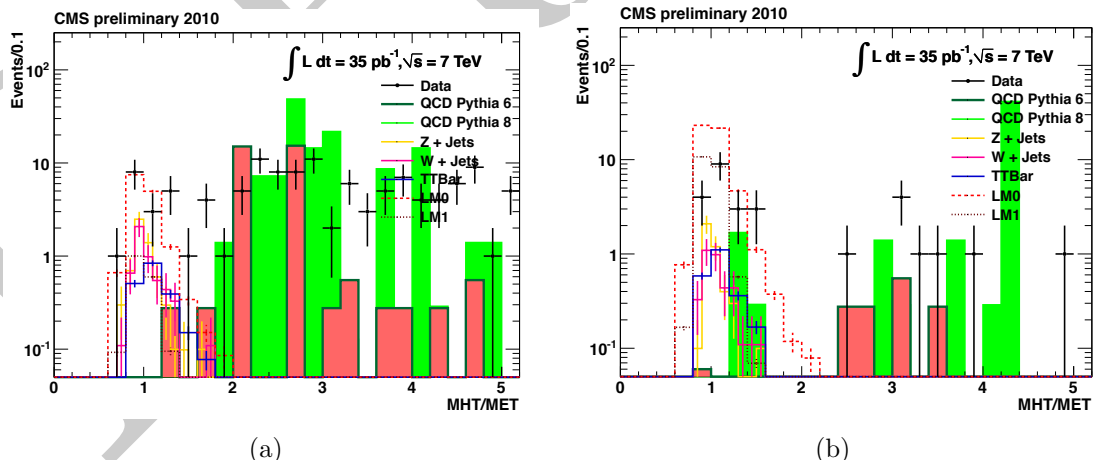


Figure 6.6.: (a) R_{miss} distribution for events in the $250 \text{ GeV} < H_T < 350 \text{ GeV}$ region, where due to the low H_T requirement QCD contamination is enriched.
(b) R_{miss} distribution for events in the $H_T > 350 \text{ GeV}$ region, QCD contamination occurs at $R_{miss} > 1.25$.

¹ simulation is used to form a translation factor between two samples measured in data,
² a control sample which closely mimics the SM processes producing missing energy, but
³ has a visible muon or photon in the final state. The background estimation methods
⁴ are described and the background predictions stated in Section 7.1. The next section
⁵ describes the triggers used to collect the data samples

⁶ 6.4. High Level triggers for the α_T analysis

⁷ The CMS trigger system has been discussed in detail in Section 3.7 and Chapter 4,
⁸ however details of analysis specific trigger paths were not discussed. During 2011 the
⁹ first α_T specific trigger was designed and deployed online. The trigger was then upgraded
¹⁰ for the higher luminosity and energy conditions of the 2012 data taking period.

¹¹ The trigger takes advantage of cutting on two variables, H_T and α_T at low H_T a high
¹² α_T value cuts the trigger rate, whereas at high H_T where the trigger rate is lower the
¹³ α_T requirement can be loosened.

¹⁴ Due to the scaling of jet thresholds in the lowest offline H_T bins as detailed in
¹⁵ Section 6.2 using a fixed jet threshold would cause inefficiency in the lowest offline H_T
¹⁶ bins. To overcome this the trigger level α_T calculation is performed iteratively for all
¹⁷ jets above a predefined threshold. This raises the total number of accepted events whilst
¹⁸ adding the benefit of being efficient for any offline jet threshold above the minimum
¹⁹ trigger jet threshold.

²⁰ Due to concerns on the time taken to perform the ΔH_T minimisation at the trigger
²¹ and time constraints enforced on trigger menu development, the first implementation
²² calculates α_T for the first 3 jets. For higher jet multiplicities the variable β_T is calculated.

$$\beta_T = \frac{H_T}{2\sqrt{H_T^2 - \cancel{H}_T^2}} \quad (6.7)$$

this gives us the relation:

$$\alpha_T \leq \beta_T. \quad (6.8)$$

²³ The decision flow is shown in Figure 6.7 and explained in detail below.

When a level one accept is issued the trigger bits that fired are checked, if the event fires a L1 muon trigger it is passed to the HLT muon triggers where only muon reconstruction is performed, reducing the reconstruction time. The α_T triggers are seeded on the lowest threshold unprescaled L1 H_T trigger, during 2011 this was L1_HTT100. Any events issuing a L1 accept and passing L1_HTT100 undergo calorimeter jet reconstruction, the reconstruction algorithm is detailed in Section 6.2.1.

Once the jets have been formed the trigger filter is entered. Initially the first two jets ranked by E_T , are considered, H_T and α_T are calculated, if both pass the trigger thresholds the event is accepted and the full detector read out is performed. If either H_T or α_T is below threshold, the next jet in E_T order is added, if the jet collection contains more than 3 jets then the β_T approximation is used. All jets in the event are added until either the event is accepted, or there are no more jets to be added above 40 GeV.

The effect of switching to the β_T approximation is to accept events that have missing energy due to miss-measurement, when calculating α_T offline these events have values of $\alpha_T < 0.5$. This introduces an impurity to the trigger and costs rate for events that will not be considered in the offline analysis.

6.4.1. Trigger efficiency measurement

The performance of the α_T trigger suit is measured with respect to a sample collected using the muon system. This allows the measurement of efficiency of both the level one seed trigger and the higher level trigger at the same time as different sub-systems are used to collect the reference and the signal triggers. This is due to the exclusive use of calorimeter jets in the α_T trigger, if more complicated reconstruction methods which produce an event hypothesis were used, muons would at HLT level only be considered as jets. Where as during calorimeter only reconstruction, muons are not considered and the p_T of any muons in an event is viewed as missing energy.

The selection for the trigger efficiency measurement is the same as listed in Section 6.2 with the requirement of exactly one well identified muon with $p_T > 45$ GeV, the sum of the \cancel{E}_T in the event and the muon must add to the W mass and finally the muon must be separated by at least 0.5 in ΔR to the closest jet, to avoid the muon energy changing the energy of the jet offline when the cross cleaning is applied.

Due to the increase in luminosity over the running period the trigger thresholds were increased, to ensure constant rate though out the year and the trigger version numbers

1 were increased each time the trigger menu was updated. The list of triggers considered
2 and their reference triggers are listed in Tables 6.1 and 6.2.

3 The efficiency of each trigger version is measured in the required H_T bins, the total
4 efficiency for each H_T bin is then calculated by combining the individual efficiencies
5 using a weighted sum based on the fraction of the total luminosity of the sample that
6 each version carries. This accounts for the change in running conditions during the data
7 taking period and the criteria that the trigger suite takes constant rate. The higher
8 trigger versions and thresholds generally represent more integrated luminosity due to the
9 evolution of running conditions with time.

10 The efficiency is measured as a function of the cumulative number of events, ie the
11 efficiency at each point on the x axis is the measured efficiency if a cut were applied
12 offline at that cut value.

13 As an example, the efficiency of each trigger used in the $275 \text{ GeV} < H_T < 325 \text{ GeV}$
14 bin is measured and then combined to give the total efficiency. The cumulative efficiency
15 curves for each trigger seeding the lowest bin is show in Figures 6.8, 6.9 & 6.10. Note
16 that some of the triggers are repeated, due to the reference trigger version incrementing
17 and the signal trigger not.

18 These are then combined to give Figure 6.11 the efficiency at a cut of $\alpha_T > 0.55$
19 is $83.3\% + 0.5\% - 0.6\%$. The loss in efficiency comes from the disparity between the
20 minimum thresholds for jets to enter the H_T and α_T calculations at the HLT and those
21 used in the analysis. The trigger jet E_T threshold is 40 GeV where as the analysis jet
22 E_T threshold in this bin is 36.6 GeV. The triggers used to take data at the end of this
23 running period also have an α_T threshold above the analysis cut of $\alpha_T > 0.55$, which
24 again causes an inefficiency. The list of efficiencies for each H_T bin are shown in Table 6.3.
25 The trigger efficiencies are measured to better than one percent and this information
26 is used in the final likelihood model, to correct the expected numbers from simulation
27 when calculating the translation factors.

28 The α_T triggers were upgraded for the increased instantaneous luminosity and pile up
29 conditions expected during the 2012 data taking period. The first stage was to implement
30 the full α_T calculation for each addition of a new jet, this change increases the purity of
31 the trigger, meaning that for the same threshold the rate taken is lower than that of the

Offline H_T bin	Signal Trigger	Reference Trigger
$275 \text{ GeV} < H_T < 325 \text{ GeV}$	HLT-HT250_AlphaT0p53_v2	HLT_Mu15_HT200_v2
$275 \text{ GeV} < H_T < 325 \text{ GeV}$	HLT-HT250_AlphaT0p53_v3	HLT_Mu15_HT200_v3
$275 \text{ GeV} < H_T < 325 \text{ GeV}$	HLT-HT250_AlphaT0p53_v4	HLT_Mu15_HT200_v4
$275 \text{ GeV} < H_T < 325 \text{ GeV}$	HLT-HT250_AlphaT0p53_v5	HLT_Mu30_HT200_v1
$275 \text{ GeV} < H_T < 325 \text{ GeV}$	HLT-HT250_AlphaT0p55_v1	HLT_Mu5_HT200_v4
$275 \text{ GeV} < H_T < 325 \text{ GeV}$	HLT-HT250_AlphaT0p55_v2	HLT_Mu40_HT200_v4
$275 \text{ GeV} < H_T < 325 \text{ GeV}$	HLT-HT250_AlphaT0p58_v3	HLT_DoubleMu8_Mass8_HT200_v4
$275 \text{ GeV} < H_T < 325 \text{ GeV}$	HLT-HT250_AlphaT0p58_v3	HLT_DoubleMu8_Mass8_HT200_v5
$275 \text{ GeV} < H_T < 325 \text{ GeV}$	HLT-HT250_AlphaT0p60_v3	HLT_DoubleMu8_Mass8_HT200_v4
$275 \text{ GeV} < H_T < 325 \text{ GeV}$	HLT-HT250_AlphaT0p60_v3	HLT_DoubleMu8_Mass8_HT200_v5
$325 \text{ GeV} < H_T < 375 \text{ GeV}$	HLT-HT300_AlphaT0p52_v1	HLT_Mu5_HT200_v4
$325 \text{ GeV} < H_T < 375 \text{ GeV}$	HLT-HT300_AlphaT0p52_v2	HLT_Mu8_HT200_v4
$325 \text{ GeV} < H_T < 375 \text{ GeV}$	HLT-HT300_AlphaT0p52_v3	HLT_Mu15_HT200_v2
$325 \text{ GeV} < H_T < 375 \text{ GeV}$	HLT-HT300_AlphaT0p53_v3	HLT_Mu15_HT200_v3
$325 \text{ GeV} < H_T < 375 \text{ GeV}$	HLT-HT300_AlphaT0p53_v4	HLT_Mu15_HT200_v4
$325 \text{ GeV} < H_T < 375 \text{ GeV}$	HLT-HT300_AlphaT0p53_v5	HLT_Mu30_HT200_v1
$325 \text{ GeV} < H_T < 375 \text{ GeV}$	HLT-HT300_AlphaT0p53_v6	HLT_Mu40_HT200_v3
$325 \text{ GeV} < H_T < 375 \text{ GeV}$	HLT-HT300_AlphaT0p53_v6	HLT_Mu40_HT200_v4
$325 \text{ GeV} < H_T < 375 \text{ GeV}$	HLT-HT300_AlphaT0p54_v5	HLT_Mu40_HT300_v4
$325 \text{ GeV} < H_T < 375 \text{ GeV}$	HLT-HT300_AlphaT0p54_v5	HLT_Mu40_HT300_v5
$325 \text{ GeV} < H_T < 375 \text{ GeV}$	HLT-HT300_AlphaT0p55_v3	HLT_DoubleMu8_Mass8_HT200_v4
$325 \text{ GeV} < H_T < 375 \text{ GeV}$	HLT-HT300_AlphaT0p55_v3	HLT_DoubleMu8_Mass8_HT200_v5

Table 6.1.: List of α_T triggers used in the lowest two offline H_T bins and the triggers used to collect the reference sample.

Offline H_T bin	Signal Trigger	Reference Trigger
$375 \text{ GeV} < H_T < 475 \text{ GeV}$	HLT-HT350_AlphaT0p51_v1	HLT_Mu5_HT200_v4
$375 \text{ GeV} < H_T < 475 \text{ GeV}$	HLT-HT350_AlphaT0p51_v2	HLT_Mu8_HT200_v4
$375 \text{ GeV} < H_T < 475 \text{ GeV}$	HLT-HT350_AlphaT0p51_v3	HLT_Mu15_HT200_v2
$375 \text{ GeV} < H_T < 475 \text{ GeV}$	HLT-HT350_AlphaT0p51_v4	HLT_Mu15_HT200_v3
$375 \text{ GeV} < H_T < 475 \text{ GeV}$	HLT-HT350_AlphaT0p51_v5	HLT_Mu15_HT200_v4
$375 \text{ GeV} < H_T < 475 \text{ GeV}$	HLT-HT350_AlphaT0p52_v1	HLT_Mu30_HT200_v1
$375 \text{ GeV} < H_T < 475 \text{ GeV}$	HLT-HT350_AlphaT0p52_v2	HLT_Mu40_HT200_v3
$375 \text{ GeV} < H_T < 475 \text{ GeV}$	HLT-HT350_AlphaT0p52_v2	HLT_Mu40_HT200_v4
$375 \text{ GeV} < H_T < 475 \text{ GeV}$	HLT-HT350_AlphaT0p53_v10	HLT_Mu40_HT300_v4
$375 \text{ GeV} < H_T < 475 \text{ GeV}$	HLT-HT350_AlphaT0p53_v10	HLT_Mu40_HT300_v5
$475 \text{ GeV} < H_T < 7 \text{ TeV}$	HLT-HT400_AlphaT0p51_v1	HLT_Mu5_HT200_v4
$475 \text{ GeV} < H_T < 7 \text{ TeV}$	HLT-HT400_AlphaT0p51_v2	HLT_Mu8_HT200_v4
$475 \text{ GeV} < H_T < 7 \text{ TeV}$	HLT-HT400_AlphaT0p51_v3	HLT_Mu15_HT200_v2
$475 \text{ GeV} < H_T < 7 \text{ TeV}$	HLT-HT400_AlphaT0p51_v4	HLT_Mu15_HT200_v3
$475 \text{ GeV} < H_T < 7 \text{ TeV}$	HLT-HT400_AlphaT0p51_v5	HLT_Mu15_HT200_v4
$475 \text{ GeV} < H_T < 7 \text{ TeV}$	HLT-HT400_AlphaT0p51_v6	HLT_Mu30_HT200_v1
$475 \text{ GeV} < H_T < 7 \text{ TeV}$	HLT-HT400_AlphaT0p51_v7	HLT_Mu40_HT200_v3
$475 \text{ GeV} < H_T < 7 \text{ TeV}$	HLT-HT400_AlphaT0p51_v7	HLT_Mu40_HT200_v4
$475 \text{ GeV} < H_T < 7 \text{ TeV}$	HLT-HT400_AlphaT0p51_v10	HLT_Mu40_HT300_v4
$475 \text{ GeV} < H_T < 7 \text{ TeV}$	HLT-HT400_AlphaT0p51_v10	HLT_Mu40_HT300_v5
$475 \text{ GeV} < H_T < 7 \text{ TeV}$	HLT-HT400_AlphaT0p52_v5	HLT_Mu40_HT300_v4
$475 \text{ GeV} < H_T < 7 \text{ TeV}$	HLT-HT400_AlphaT0p52_v5	HLT_Mu40_HT300_v5

Table 6.2.: List of α_T triggers used in the $H_T > 375 \text{ GeV}$ bins and the triggers used to collect the reference sample.

H_T range (GeV)	Trigger efficiency (%)
275–325	$83.3^{+0.5}_{-0.6}$
325–375	$95.9^{+0.7}_{-0.9}$
375–475	$98.5^{+0.5}_{-0.9}$
475– ∞	$100.0^{+0.0}_{-4.8}$

Table 6.3.: Efficiencies of the α_T triggers used in the 7 TeV α_T analysis on 5 fb^{-1} of LHC data.

H_T range	Trigger
275 GeV–325 GeV	HLT-HT250_AlphaT0p55_v*
325 GeV–375 GeV	HLT-HT300_AlphaT0p53_v*
375 GeV–475 GeV	HLT-HT350_AlphaT0p52_v*
475 GeV–8 TeV	HLT-HT400_AlphaT0p51_v*

Table 6.4.: Triggers used to seed the analysis H_T bins during 2012 data taking.

1 previous algorithm. This allows the thresholds to be kept low, whilst not increasing the
2 overall trigger rate.

3 The second upgrade was to switch to pile up corrected jets at the HLT, this change
4 keeps the trigger cross section liner as a function of instantaneous luminosity.

5 The third choice was to design a trigger suite that could run for the entire 2012
6 data taking period, with out changing the trigger thresholds, this was done to make the
7 measurement of the efficiency simpler.

8 The trigger thresholds used are presented in Table 6.4, due to the constant thresholds
9 in H_T and α_T though out the run, the versioning of the triggers is excluded from this
10 table. The efficiency of the triggers is measured for 11.7 fb^{-1} of LHC data taken at a
11 centre of mass energy of 8 TeV the efficiencies were measured for the analysis presented
12 at HCP, documented in [39]. A single muon trigger is used to collect the reference sample,
13 the threshold of this trigger was unchanged during the data taking period, the path
14 selected is HLT_IsoMu24_v* which requires at least one muon with $p_T > 24 \text{ GeV}$ that is
15 not over lapping with any other object in the detector. The same method is used as for
16 the 2011 trigger efficiency measurement. However the offline jets are corrected for pile
17 up using the fast jet corrections, to stay inline with the HLT object definitions.

18 Figure 6.12 shows the efficiencies of the four individual triggers that seed the 275 GeV–
19 325 GeV H_T bin for 11.7 fb^{-1} of 8 TeV LHC data, Figure 6.13 shows the combined
20 cumulative efficiency of the 2012 trigger suite.

21 The two trigger suites have very similar offline performance with 100% efficiency
22 in the analysis bins above 475 GeV and high efficiency in the lower bins. To quantify
23 the difference in performance between the two algorithms the purity is defined as the
24 number of events passing the trigger that pass the offline α_T requirement at the same

H_T range (GeV)	Trigger efficiency (%)
275 GeV – 325 GeV	$89.6^{+0.4}_{-0.4}$
325 GeV – 375 GeV	$98.6^{+0.2}_{-0.3}$
375 GeV – 475 GeV	$99.4^{+0.2}_{-0.3}$
475 GeV – 8 TeV	$100.0^{+0.0}_{-0.5}$

Table 6.5.: Efficiencies of the α_T triggers at a centre of mass energy of 8 TeV α_T measured in 11.7 fb^{-1} of LHC data.

threshold as the trigger requirement divided by the total number of events accepted by the trigger. The purity of each trigger algorithm is measured for an example trigger with a H_T threshold of 350 GeV and an α_T threshold of 0.52. The 2011 trigger which only performs the full α_T calculation for jet multiplicities of less than four has a purity of 48%, which means a quarter of all rate taken by the trigger is used in the offline analysis. The 2012 trigger which performs the full α_T calculation for all jet multiplicities has a purity of 75%. This 25% increase in purity translates in to a 25% rate reduction for the same trigger threshold when changing to the full α_T calculation for all jet multiplicities, thus enabling the trigger thresholds to be kept at the same or lower thresholds in the 2012 run as in the 2011 run.

6.5. Extension to higher analysis dimensions.

B-tagging

Declaration Whilst it should be noted that the author did not contribute towards the extension of the analysis to include a dimension based on the measurement of the number of jets containing b quarks in the final state, the final analysis does include this extension, hence the b-tagging procedure is explained in sufficient detail as to understand the process but not to elude to all the nuances of the method in the following section.

Jets are tagged as originating from a b decay via the identification of a displaced vertex as it takes the b a finite amount of time to decay, during this time the quark which is not produced at rest travels away from the initial interaction point, where upon decaying a secondary decay vertex is created. The algorithm used to classify these jets as containing a b quark is the Combined Secondary Vertex (CSV) tagger. The “Medium” working point is used in the analysis, which requires a cut of > 0.679 on the CSV value.

- ¹ This results in a gluon/light quark miss tag rate of 1% where “light” quarks are u, d and
² s types. The efficiency for tagging b quark jets in the range 60 – 70%[40] is achieved,
³ this efficiency depends on the jet p_T . The discriminator is supported by the CMS b
⁴ physics object group[41] and its performance is well understood. The Montecarlo miss
⁵ tag and identification rates are re-weighted to agree with data observations, thus provide
⁶ an accurate background prediction for the high multiplicity b-tagged bins which are
⁷ dominated by the miss tag of light quarks as b quarks.

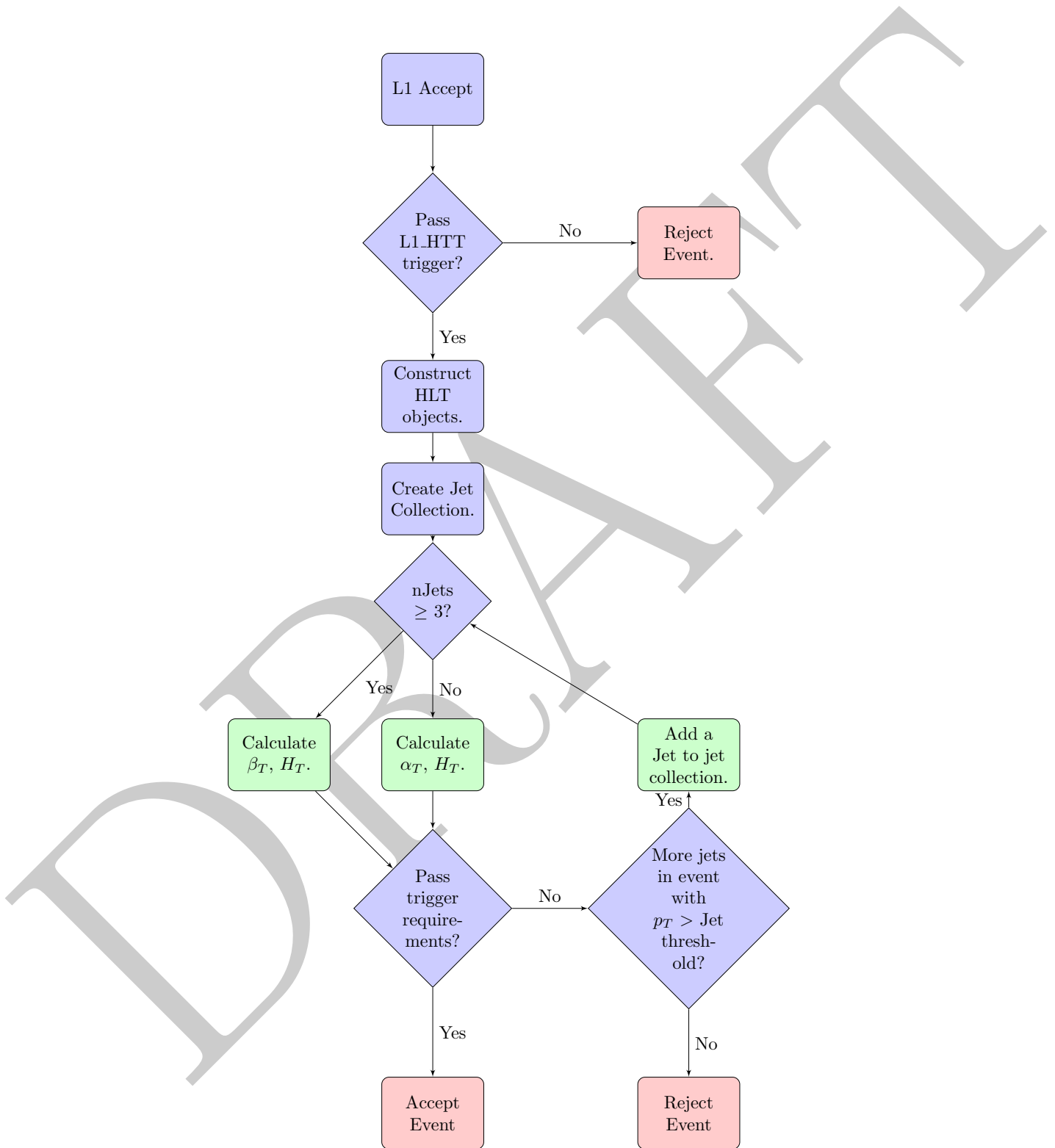


Figure 6.7.: Flow chart representing the steps taken to make a trigger decision using the α_T trigger algorithm.

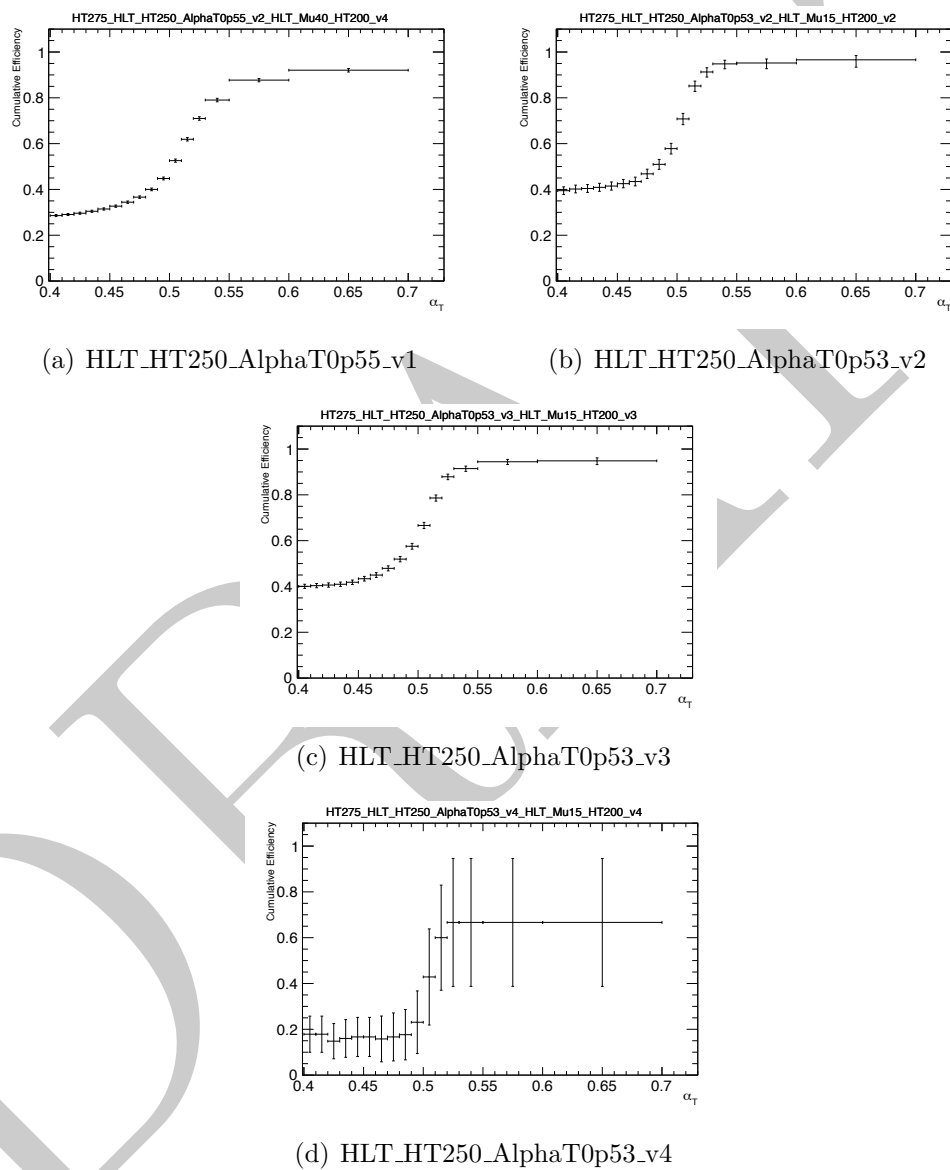


Figure 6.8.: Turn on curves for the individual α_T triggers used to seed the $275 \text{ GeV} < H_T < 325 \text{ GeV}$ bin.

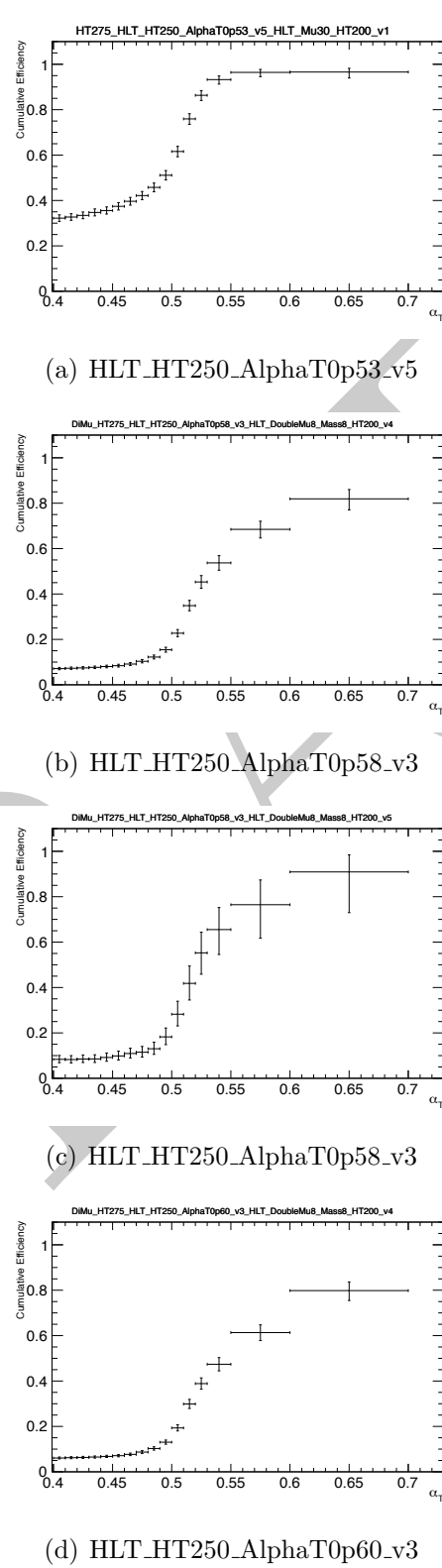
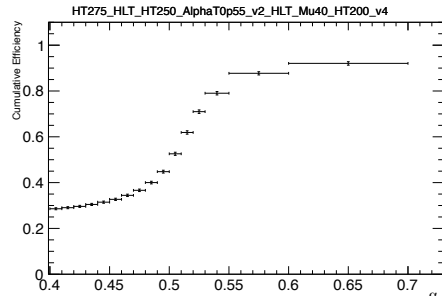


Figure 6.9.: Turn on curves for the individual α_T triggers used to seed the $275 \text{ GeV} < H_T < 325 \text{ GeV}$ bin.



(a) HLT_HT250_AlphaT0p60_v3

Figure 6.10.: Turn on curves for the individual α_T triggers used to seed the $275 \text{ GeV} < H_T < 325 \text{ GeV}$ bin.

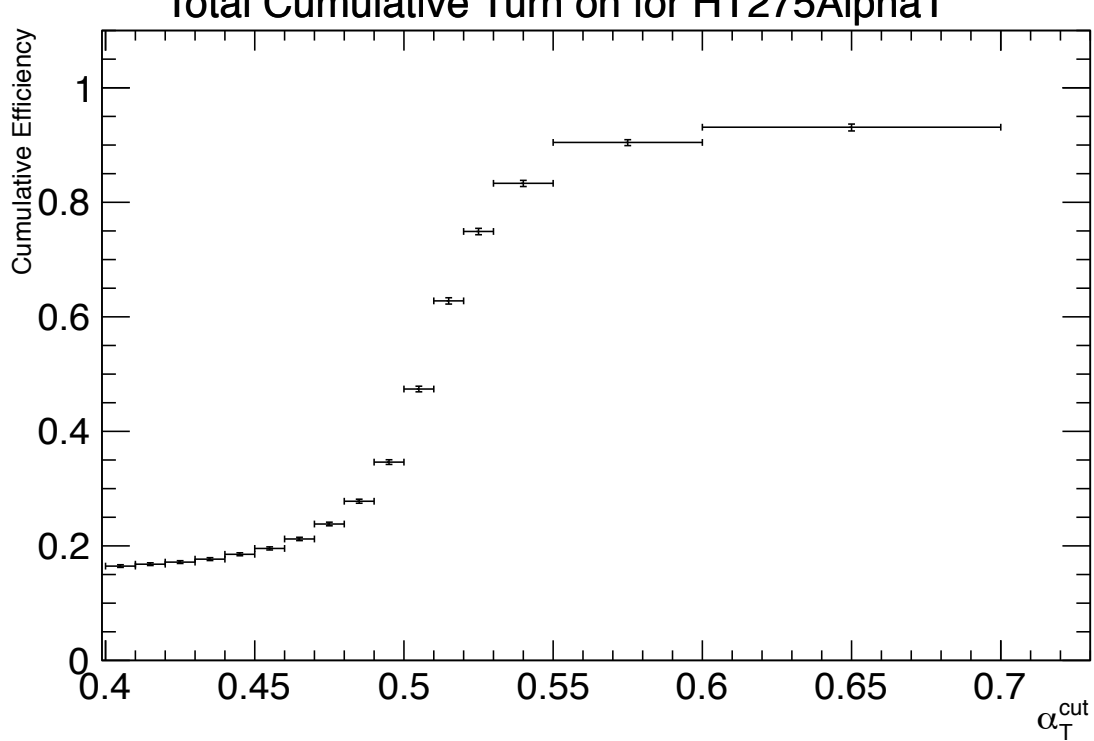


Figure 6.11.: Combined cumulative efficiency for the triggers seeding the $275 \text{ GeV} < H_T < 325 \text{ GeV}$ offline analysis bin.

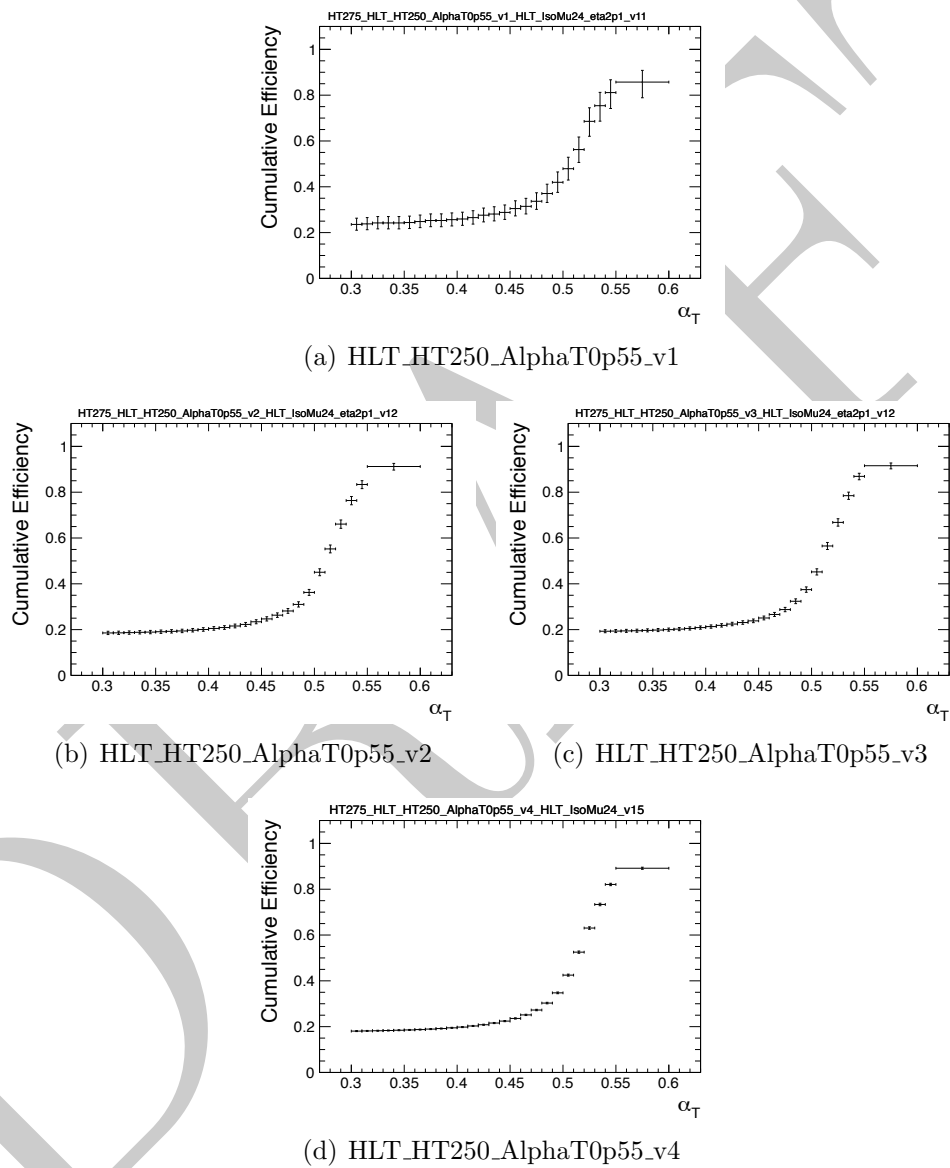


Figure 6.12: Turn on curves for the individual α_T triggers used to seed the $275 \text{ GeV} < H_T < 325 \text{ GeV}$ bin, during 2012 data taking.

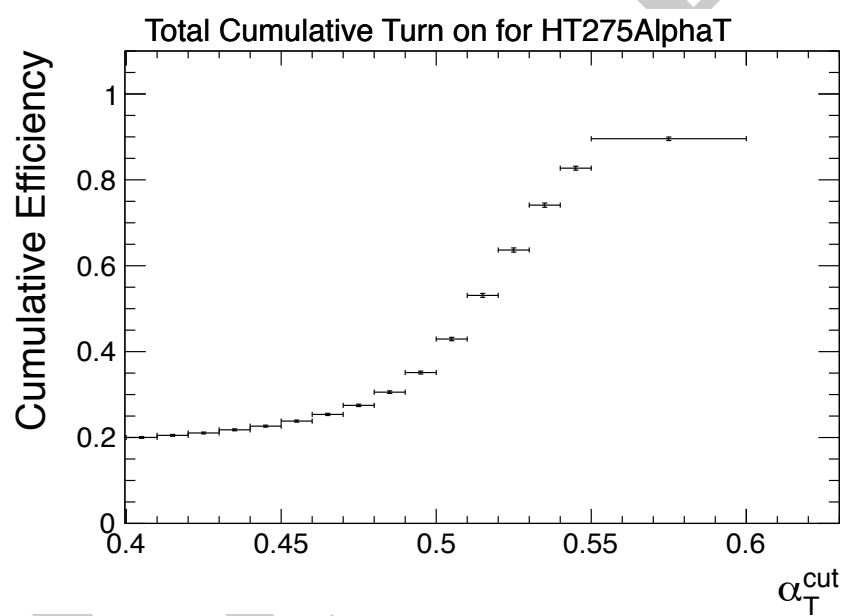


Figure 6.13.: Combined cumulative efficiency for the triggers seeding the $275 \text{ GeV} < H_T < 325 \text{ GeV}$ offline bin for 11.7 fb^{-1} of 8 TeV LHC data.

Chapter 7.

¹ Background Prediction

² 7.1. Electro-Weak Background Prediction

³ The requirement of an α_T cut on the signal sample removes multi-jet QCD events where a
⁴ balanced event is counted as signal due to miss-measurements, the remaining background
⁵ events in the signal region are due to electro-weak processes which produce real missing
⁶ energy. Primarily these events are produced from $Z \rightarrow \nu\bar{\nu} + \text{Jets}$, $W \rightarrow \ell\bar{\nu} + \text{Jets}$ and
⁷ $t\bar{t}$ decay, with smaller contributions from Drell-Yan + Jets, single top production in the
⁸ s,t and tW channels and from di-boson + Jet events. To predict the number of these
⁹ events contributing to the number of signal like events three control samples are defined
¹⁰ and though the use of a Montecarlo derived transfer factor the control samples are used
¹¹ to predict the number of SM events expected in the signal region.

¹² Figure 7.1[1] shows the expectation from simulation in all bins of the hadronic signal
¹³ region, for the different background samples and an example CMSSM reference model
¹⁴ RM1.

¹⁵ Explain what RM1 is

¹⁶ The expected composition of the the backgrounds in the hadronic signal region, as a
¹⁷ percentage of the total SM background, are summarised in Table 7.1. $Z \rightarrow \nu\nu$ contributes
¹⁸ $\approx 43\%$ of the SM background in the 275 GeV–325 GeV H_T bin, raising to $\approx 53\%$ in the
¹⁹ $H_T > 875$ GeV bin. Events entering the signal region due to Z or W decays where the
²⁰ lepton is missed by the lepton vetoes account for $\approx 25\%$ at low H_T and $\approx 13\%$ at high H_T .
²¹ Events from hadronically decays τ (τ_h) have a low H_T dependance, contributing $\approx 22\%$
²² of the background at low H_T and $\approx 27\%$ of the background at high H_T . Those events

- ¹ arising from τ particles which decay leptonically (τ_l) and are missed by the lepton vetoes
² account for $\approx 10\%$ of the SM background.

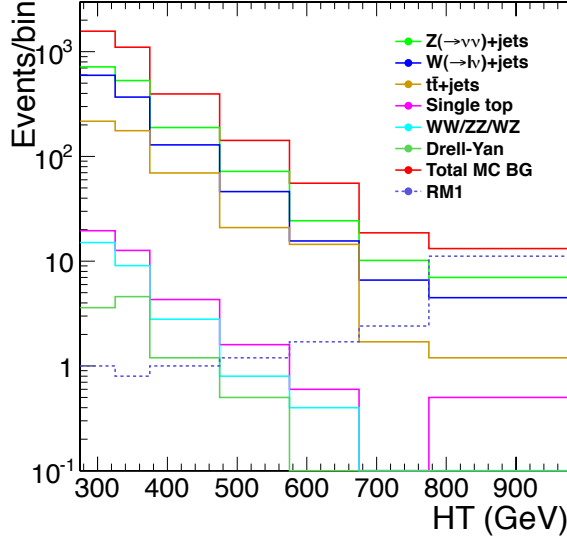


Figure 7.1.: Expectation from MC in all bins of the hadronic signal region for the following different background processes: $Z \rightarrow \nu\nu + \text{jets}$, $W + \text{jets}$, $t\bar{t}$, single top + jets, di-boson production ($WW/WZ/ZZ$), and Drell-Yan. The total SM expectation is also shown, along with that for the CMSSM benchmark model RM1.

Table 7.1.: Relative background composition as given by MC simulation in all bins of the hadronic signal region (expressed as a percentage of the total SM background).

H_T GeV	N _{events}	$Z \rightarrow \nu\nu + \text{jets}$ (%)	W + jets, $t\bar{t}$, single top, DY and di-boson			
			missed e, μ from W/Z (%)	τ_h (%)	τ_l (%)	τ_h matched to jet (%)
275–325	3938.0	43	24	22	11	7
325–375	1569.9	46	25	22	9	7
375–475	1104.2	48	20	23	10	7
475–575	396.0	48	17	24	11	10
575–675	142.4	51	17	23	10	11
675–775	55.5	44	19	31	7	17
775–875	18.7	55	17	22	4	9
875– ∞	13.2	53	13	27	7	19

- ³ To calculate the bin by bin translation factors the signal selection and the individual
⁴ control selections are applied to the montecarlo simulated background samples. The ratio

of the number of accepted events is then taken, the signal yield prediction is computed from applying the control selections to real data and multiplying the event yield by the translation factor. The measurements from all control samples are considered simultaneously in a fit defined in Section 7.5. This method can be extended to high dimensions of analysis bins, for example in [39] a secondary dimension involving the number of B quarks in the event is studied. However the B extension is not detailed in this thesis.

$$N_{\text{prediction}}^{\text{sig}}(H_T) = N_{\text{obs}}^{\text{control}}(H_T) \times \frac{N_{MC}^{\text{sig}}(H_T)}{N_{MC}^{\text{control}}(H_T)} \quad (7.1)$$

The three control samples used are a $W \rightarrow \mu\nu + \text{Jets}$ sample, a $Z \rightarrow \mu\mu + \text{Jets}$ sample and a $\gamma + \text{Jets}$ sample.

The selection criteria for each of these control samples is kept as similar to the signal selection as possible, so as to not introduce systematic errors from incorrect modelling in the simulation. The use of the ratio of the number of observed events in the montecarlo cancels the systematic effects. A systematic is still assigned to each translation factor to account for theoretical uncertainties and acceptance and instrumental effects.

Additional kinematic cuts are applied in the two muon control samples to enrich the $W + \text{Jets}$ $t\bar{t}$ and $Z + \text{Jets}$ components in the control samples. The samples are defined to maximised efficiency rather than purity, any impurities are accounted for in the transfer factors as the yields from all montecarlo samples are used. This is valid under the assumption that the SM electro-weak and Drell-Yan processes are well modelled by the simulation. The possibility of SUSY like signal contamination in the control samples is accounted for in the final likelihood, after measuring the signal acceptance for the control samples on simulated SUSY events.

The magnitude of the systematic uncertainties on the transfer factors is motivated by a set of closure tests between the control samples. A transfer factor is produced to predict each control sample from each of the other control samples. No assumed systematic is applied in these closure tests, instead the level of agreement with in statistical uncertainty is used to set the scale of the systematic error for each H_T bin.

¹ 7.1.1. The $\mu + \text{Jets}$ control sample

² The $\mu + \text{Jets}$ control sample is designed to mimic the events appearing in the signal region
³ due to $W + \text{Jets}$ and $t\bar{t}$ decays where the leptons are missed offline, either due to falling
⁴ out of acceptance or being missed by the reconstruction algorithms. Hadronic tau decays
⁵ from high p_T W bosons are also predicted from this sample. The additional selection
⁶ criteria for this sample are designed to select events containing the decay $W \rightarrow \mu\nu + \text{Jets}$
⁷ in the same kinematic conditions as those events entering the signal selection. Offline the
⁸ event level discriminators, H_T and α_T , are calculated using only the hadronic components
⁹ of the event. In order to select the W exactly one tightly identified, isolated muon with in
¹⁰ $|\eta| < 2.5$ with $p_T > 10$ GeV is required. The transverse mass of the muon combined with
¹¹ the missing energy of the event $M_T(\mu, \cancel{E}_T)$ is required to be larger than 30 GeV, as shown
¹² in Figure 7.2 the transverse mass cut removes a large amount of QCD whilst preserving
¹³ a high efficiency W selection. Events are vetoed if for any jet $\Delta R(\mu, \text{Jet}) < 0.5$, or if a
¹⁴ second muon candidate exists that is either loose, non-isolated or outside of acceptance
¹⁵ if the two muons have an invariant mass within ± 25 GeV of the Z mass, to suppress
¹⁶ $Z \rightarrow \mu\mu$ events.

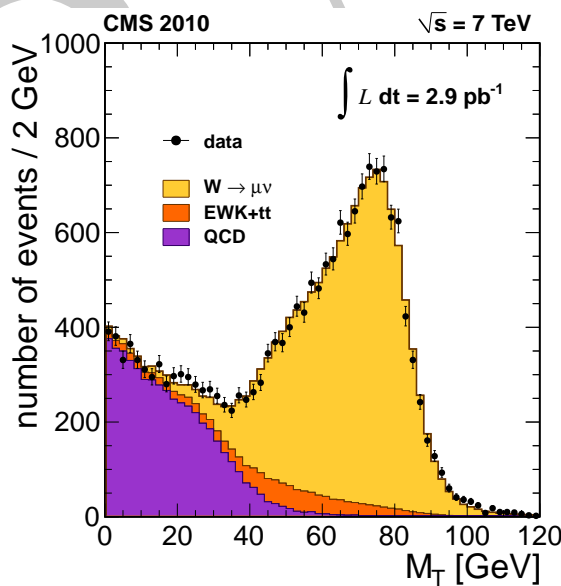


Figure 7.2.: Transverse mass between the selected muon and \cancel{E}_T in $W \rightarrow \mu\nu$ events.[42].

¹ 7.1.2. The $\mu\mu + \text{Jets}$ control sample

² The $\mu\mu + \text{Jets}$ control sample is used to measure the $Z \rightarrow \nu\nu + \text{Jets}$ irreducible
³ background in the signal region. The process $Z \rightarrow \mu\mu + \text{Jets}$ is identical kinematically,
⁴ however the acceptance and the branching ratio are both smaller the branching ratio due
⁵ to the possible decay in to one of three neutrino flavour states verses the requirement of
⁶ a particular lepton flavour, the acceptance difference is due to the p_T and identification
⁷ quality requirements on the muons alter the acceptance between the two processes. The
⁸ following selection criteria are applied on top of the common selection: Exactly two
⁹ tightly identified, isolated muons, with in $|\eta| < 2.5$ with $p_T > 10$ GeV are required; The
¹⁰ invariant mass of the di-muon pair is required to be with in ± 25 GeV of the Z mass;
¹¹ Events are vetoed if for any muon and jet combination $\Delta R(\mu, \text{Jet}) < 0.5$. As in the
¹² single muon control sample all event level quantities are calculated from the hadronic
¹³ objects alone. This control sample can be used in all of the offline H_T bins.

¹⁴ 7.1.3. The $\gamma + \text{Jets}$ control sample

¹⁵ The $\gamma + \text{Jets}$ control sample can also be used to measure the $Z \rightarrow \nu\nu + \text{Jets}$ background
¹⁶ as the $\gamma + \text{Jets}$ process is kinematically similar when the $\gamma E_T > \approx 100$ GeV[43, 44], again
¹⁷ when calculating the event level quantities only hadronic objects are considered. The
¹⁸ photon sample requires the following criteria on top of the common selection requirements:
¹⁹ Exactly one photon with $E_T > 150$ GeV to ensure trigger efficiency, $|\eta| < 1.45$. Events
²⁰ are vetoed if for any jet $\Delta R(\gamma, \text{jet}) < 1.0$. Given that due to the trigger requirements the
²¹ photon E_T is required to be greater than 150 GeV and the photon is treated as missing
²² energy, the $\alpha_T > 0.55$ requirement implies a minimum H_T threshold of ≈ 350 GeV, hence
²³ the $\gamma + \text{Jets}$ control sample can only be used in the offline region where $H_T > 375$ GeV.

²⁴ Table 7.2 gives the hadronic signal yields in each of the offline H_T bins along with
²⁵ the simple background estimate from the single muon plus jets control sample. The full
²⁶ background prediction is given from the results of the simultaneous fit to the separate
²⁷ background estimates.

Table 7.2.: Total SM prediction using the $\mu + \text{Jets}$ sample only. These are illustrative only, as the final prediction is provided by the final simultaneous fit.

α_T bin	0.55– ∞	0.55– ∞	0.55– ∞	0.55– ∞
H_T bin (GeV)	275–325	325–375	375–475	475–575
Hadronic selection MC	2872.32 ± 64.44	1384.22 ± 51.46	1041.38 ± 12.53	396.13 ± 19.85
$\mu + \text{jets}$ selection MC	1228.90 ± 46.18	670.50 ± 38.74	495.14 ± 7.86	181.65 ± 9.65
Translation factor	2.34 ± 0.10	2.06 ± 0.14	2.10 ± 0.04	2.18 ± 0.16
$\mu + \text{jets}$ selection yield data	1421	645	517	169
Total SM prediction	3321.30 ± 169.97	1331.57 ± 105.45	1087.36 ± 52.50	368.56 ± 39.09
Hadronic yield data	3703	1533	1043	346
α_T bin	0.55– ∞	0.55– ∞	0.55– ∞	0.55– ∞
H_T bin (GeV)	575–675	675–775	775–875	875– ∞
Hadronic selection MC	142.37 ± 7.61	55.47 ± 3.51	18.68 ± 1.45	13.18 ± 1.15
$\mu + \text{jets}$ selection MC	70.84 ± 4.36	22.64 ± 1.82	7.54 ± 0.80	5.19 ± 0.67
Translation factor	2.01 ± 0.16	2.45 ± 0.25	2.4 ± 0.33	2.54 ± 0.40
$\mu + \text{jets}$ selection yield data	52	18	8	1
Total SM prediction	104.50 ± 16.81	44.09 ± 11.33	19.83 ± 7.41	2.54 ± 3.47
Hadronic yield data	122	44	14	6

1 7.1.4. Muon control samples with out an α_T cut.

2 The requirement of an α_T value above 0.55 in the previous control samples limits the
 3 event yield of each of the montecarlo samples, increasing the statistical error of the
 4 prediction. This is especially evident when splitting the analysis in to more dimensions
 5 than the H_T binning. The requirement of an α_T cut on the control samples means that
 6 as the muon is not seen by the calorimeter systems the signal trigger can also be used
 7 to collect the both the single and di muon background samples. The translation factor
 8 method can be used to create a prediction from any sample to any other sample if and
 9 only if the modelling of the event kinematics and acceptances of any cuts introduces
 10 no large systematic errors. We now show that the montecarlo simulation accurately
 11 reproduces the kinematics and acceptance of the α_T cut when applied to electro-weak
 12 background samples, enabling the removal of the α_T requirement for the muon control
 13 samples.

14 The preselection of events in the two muon control samples ensures samples with
 15 negligible QCD contamination, which are enriched with $t\bar{t}$, $W + \text{Jets}$ and $Z + \text{Jet}$ events.
 16 This is shown for the $\mu + \text{Jets}$ sample in Figure 7.3 and for the $\mu\mu + \text{Jets}$ sample in

- Figure 7.4, in both sets of plots the expected number of QCD events from montecarlo simulation is less than one event at any α_T value for 5 fb^{-1} of integrated luminosity. The requirement of tight isolation on each of the muons is largely responsible for the purity of the sample, the transverse mass and di-muon mass window cuts ensure the sample is rich in electro-weak events with visible muons. The agreement between data and montecarlo in these plots is good and the simulation models the α_T acceptance well, the systematic assigned to this acceptance is detailed in Section 7.2.

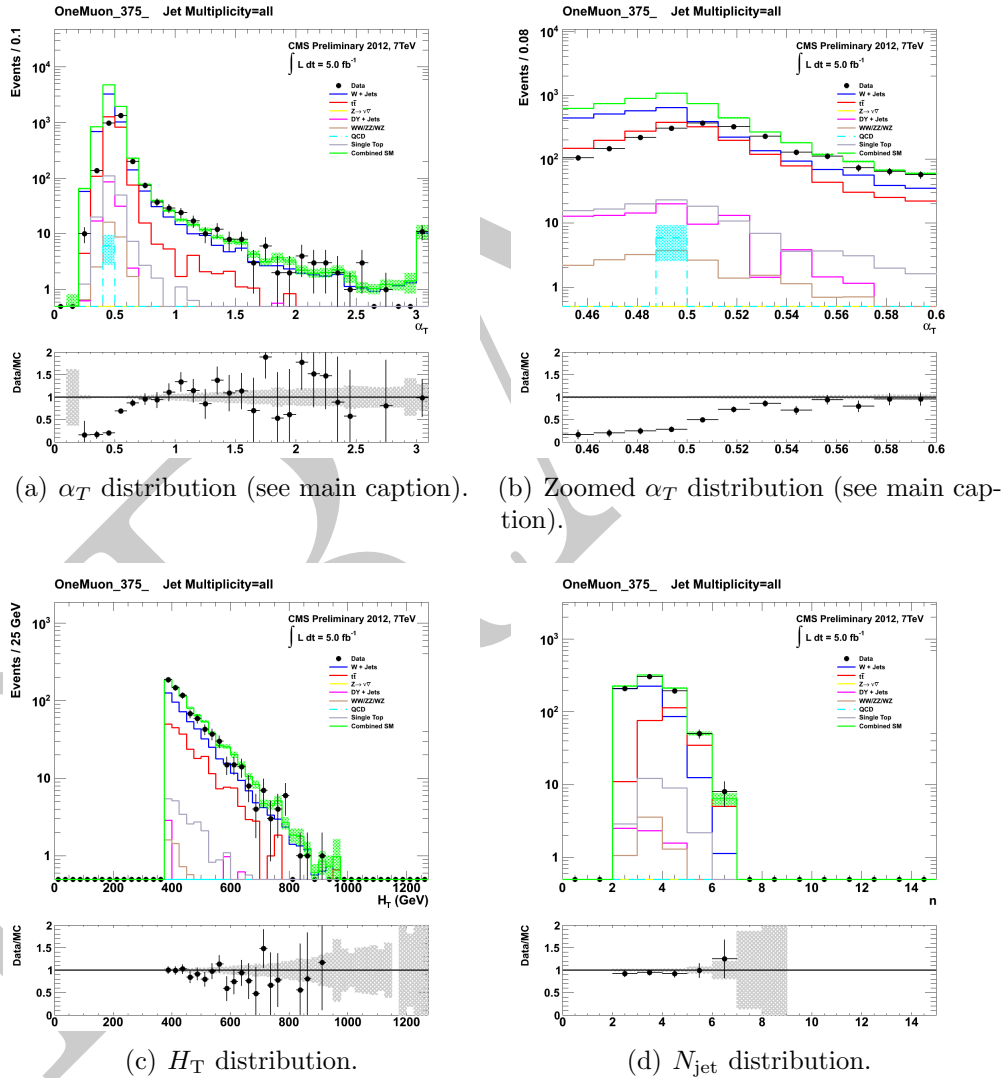


Figure 7.3.: Data–MC comparisons of key variables for the muon control sample, for the region $H_T > 375 \text{ GeV}$ and $\alpha_T > 0.55$. Bands represent the uncertainties due to the limited size of MC samples. No requirement is made on the number of b-tagged jets in an event. *The discrepancy in the α_T distributions for values $\alpha_T > 0.55$ is due to the trigger not being simulated in the MC simulation.*

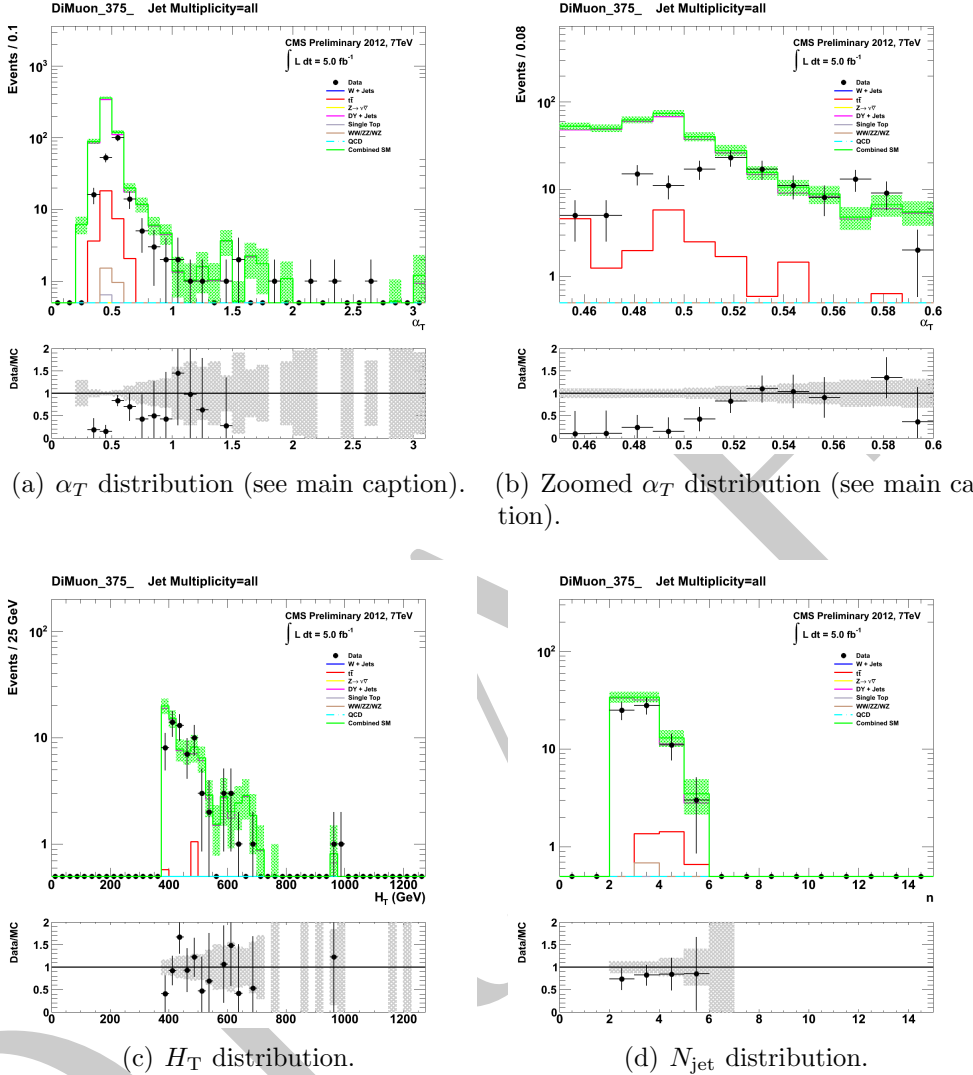


Figure 7.4.: Data–MC comparisons of key variables for the di-muon control sample, for the region $H_T > 375 \text{ GeV}$ and $\alpha_T > 0.55$. Bands represent the uncertainties due to the limited size of MC samples. No requirement is made on the number of b-tagged jets in an event. *The discrepancy in the α_T distributions for values $\alpha_T > 0.55$ is due to the trigger not being simulated in the MC simulation.*

Moving to a selection where there is no required α_T cut means that the α_T trigger suite can not be used to collect the high event yield control samples. Instead a trigger requiring H_T and a muon in the final state (Mu_HT) is used, due to the muon trigger threshold the p_T acceptance cut is raised to 45 GeV in these control samples. The H_T requirement on these triggers raises to 300 GeV so only the offline bins with $H_T > 375 \text{ GeV}$ are able to benefit from the increased background estimation precision, due to the larger size of the predicting sample. The efficiency for triggering on a single muon at

¹ 45 GeV is measured to be $91.3 \pm 0.1\%$ though out the data taking period, measured for
² the H_T + single muon triggers, the H_T component of the trigger is measured to be 100%
³ efficient though out. In the case of the di-muon sample, as both muons have to be above
⁴ 45 GeV and either of them could have triggered the event, the efficiency is found to be
⁵ H_T -dependant in the range of 95-97%.

⁶ The muon control samples in the H_T bins where $H_T < 375$ GeV are collected with
⁷ the α_T trigger suite and the measured efficiencies are the same as those measured for the
⁸ hadronic sample. The details of the triggers used for each of the muon + Jets control
⁹ samples are listed in Table 7.3.

Table 7.3.: List of triggers used for the larger $\mu + \text{Jets}$ and $\mu\mu + \text{Jets}$ samples.

H_T bin (GeV)	275–325	325–375	375–475	475–575	575–675	675–775	775–875	>875
α_T cut	0.55	0.55	None	None	None	None	None	None
Muon p_T cut	10	10	45	45	45	45	45	45
Trigger	α_T	α_T	Mu_HT	Mu_HT	Mu_HT	Mu_HT	Mu_HT	Mu_HT
Dataset	HT	HT	MuHad	MuHad	MuHad	MuHad	MuHad	MuHad
Thresholds	Table A.2	Table A.2	Table A.3					

¹⁰ 7.2. Systematic uncertainties on the electro-weak ¹¹ background model.

¹² As previously discussed in Section 7.1 the final background prediction is given by the
¹³ simultaneous fit to the yields in the signal and control samples and the translation
¹⁴ factors obtained from MC. The fit has some freedom via the statistical and systematic
¹⁵ uncertainties measured for each translation factor. This implies that the measurement of
¹⁶ the systematic uncertainties on the translation factors are vital for the fitting procedure.

¹⁷ A set of closure tests were performed on data to identify any sources of systematic
¹⁸ biased introduced by the background prediction method. To do this the individual
¹⁹ background samples are used to predict one another using the same translation factor
²⁰ method as for the prediction of SM missing energy sources in the hadronic signal regions.
²¹ The level of agreement is quantified in terms of the ratio $(N_{\text{obs}} - N_{\text{pred}}) / N_{\text{pred}}$, the
²² statistical error from the translation factor, based on the available Montecarlo stats

is combined with the statistical error on the number of events in the predicting sample to give the error on the closure, hence the deviation of the ratio from zero gives the level of closure per analysis bin. This gives a measure of any biases introduced by the background estimation method.

The closure tests between the background samples are designed to test the Montecarlo's ability to model kinematic effects; such as the α_T acceptance; μ acceptance and γ acceptance, instrumental effects such as; reconstruction efficiencies and the effects of pile up on isolation and finally the theoretical precision of the production and decay cross sections and their relative contributions to the SM background. These individual components are not separable by the closure tests, which instead gives a total systematic error estimation.

As described in Section 7.1.4 the control samples which do not require an α_T cut use a Mu-HT cross object trigger to collect the data events. As shown in Table A.3 there was a period of data taking where due to the increased trigger thresholds the Mu-HT triggers are unsuitable for use in the region $H_T < 375$ GeV. Thusly in the closure tests between the control samples which use an α_T cut and those that do not the integrated luminosity is limited to 3.9 fb^{-1} . This causes a loss of some statistical power in these cases.

The individual closure tests and fits to the H_T dependance of the ratio $(N_{obs} - N_{pred}) / N_{pred}$ are shown in Appendix C. The Figures C.1 show the closure of the prediction between $\mu + \text{Jets}(\text{no } \alpha_T) \rightarrow \mu + \text{Jets}(\alpha_T > 0.55)$ and $\mu\mu + \text{Jets}(\text{no } \alpha_T) \rightarrow \mu\mu + \text{Jets}(\alpha_T > 0.55)$ for two samples, one with no requirement on the number of b tagged jets (n_b), which increases the precision of the measurement, and one requiring $n_b = 1$, the red line is the result of a one parameter fit. The level of closure shows that the Montecarlo accurately models the α_T acceptance, with no significant bias.

Figure C.2 shows the closure between $\mu + \text{Jets} \rightarrow \mu\mu + \text{Jets}$ and between $\gamma + \text{jets} \rightarrow \mu\mu + \text{Jets}$ over both the full H_T range using only 3.9 fb^{-1} of integrated luminosity and for $H_T > 375$ GeV using the full data set. Again the red lines are the result of fitting with a one parameter fit.

Figure C.3 tests the closure between samples with differing n_b the three tests are $\mu + \text{Jets}(n_b = 0) \rightarrow \mu + \text{Jets}(n_b = 1, \text{no } \alpha_T)$, $\mu + \text{Jets}(n_b = 1) \rightarrow \mu + \text{Jets}(n_b > 1, \text{no } \alpha_T)$ and $\mu + \text{Jets}(n_b = 0) \rightarrow \mu + \text{Jets}(n_b > 1, \text{no } \alpha_T)$. Figure C.4 also tests the closure between samples with differing n_b , here the test is between $\mu + \text{Jets}(n_b = 0) \rightarrow \mu\mu + \text{Jets}(n_b = 0)$ and $\mu + \text{Jets}(n_b = 1) \rightarrow \mu\mu + \text{Jets}(n_b = 1)$.

Finally any dependance on pile up is measured by comparing a subset of the individual closure tests between samples which have pile up subtracted jets and those that do not. The example closures are $\mu + \text{Jets}(\text{no } \alpha_T) \rightarrow \mu + \text{Jets}(\alpha_T > 0.55)$, $\mu + \text{Jets}(\text{no } \alpha_T) \rightarrow \mu\mu + \text{Jets}(\text{no } \alpha_T)$, and $\mu + \text{Jets}(n_b = 0) \rightarrow \mu + \text{Jets}(n_b = 1, \text{no } \alpha_T)$.

7.3. Motivating the combined systematic on the translation factors

The closure tests described in the previous section are combined to give a total systematic uncertainty. This uncertainty is binned in to three H_T regions $275 \text{ GeV} \rightarrow 575 \text{ GeV}$, $575 \text{ GeV} \rightarrow 775 \text{ GeV}$ and 775 GeV+ . In each of these regions all of the individual closure tests are used to calculate a weighted mean and variance. The systematic is defined as 3σ of this variance, which is conservative but necessary to cover any biases. The systematics are treated as fully uncorrelated between the three regions, again this is the conservative approach. Figure 7.5 shows the key example closures, the grey shaded region shows the systematic error. The values obtained for the error are 6%, 20% and 39%, these are rounded to 10%, 20% and 40% and then used in the final background simultaneous fit.

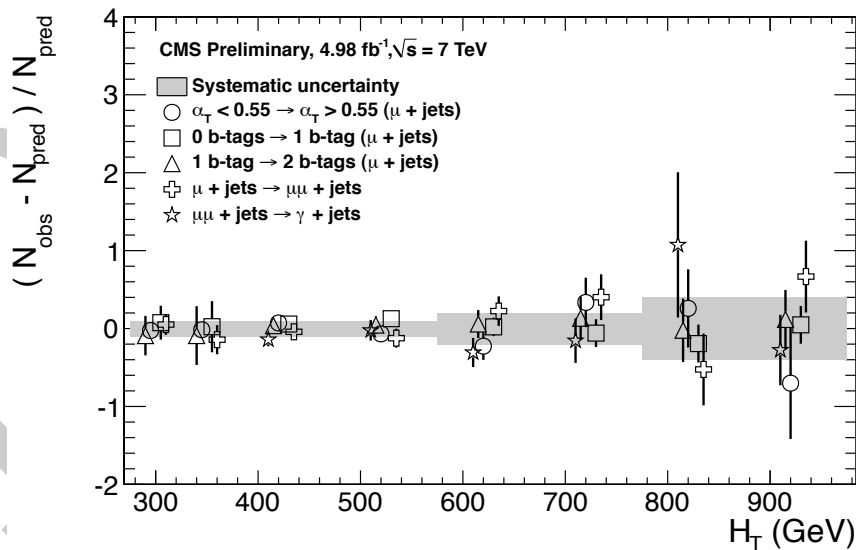


Figure 7.5.: A set of closure tests (open symbols) overlaid on top of grey bands that represent the systematic uncertainties used for three H_T regions in the final simultaneous fit. The solid circles and their errors represent the weighted mean and standard deviation for the five closure tests of each individual H_T bin.

¹ 7.4. Estimating the residual QCD background component.^[1]

³ The expected QCD contamination in the signal region where $H_T > 275$ GeV and $\alpha_T >$
⁴ 0.55 from simulated background samples is negligible, residual events are removed via the
⁵ application of the detector failure and $R_{miss} < 1.25$ filters. However due to the difficulty
⁶ in simulating QCD multi jet events accurately a conservative approach is taken where a
⁷ term is inserted in the likelihood to model any residual QCD contamination.

The term is based on the ratio of the number of events above and below the α_T threshold of 0.55 in the individual H_T bins. The dependance of this ratio is modelled as an exponentially falling quantity:

$$R_{\alpha_T}(H_T) = \mathcal{A}_{n_b} e^{-k_{QCD} H_T} \quad (7.2)$$

⁸ Where \mathcal{A}_{n_b} is the b-tag bin dependant normalisation factor and k_{QCD} is the b-tag
⁹ dependant decay constant.

¹⁰ The exponential behaviour is due to several features, the first of which is the improve-
¹¹ ment of the jet energy resolution with H_T due to the larger energies deposited in the
¹² calorimeter systems. Secondly for the region $H_T > 375$ GeV the jet multiplicity rises
¹³ slowly with H_T , which due to the combinatorics used in the α_T calculation, results in
¹⁴ a narrower α_T distribution peaked at 0.5. Due to the signal region definition and the
¹⁵ exponentially falling nature of the QCD background component is reduced to zero above
¹⁶ ≈ 500 GeV, thus the validity of the QCD background model above 575 GeV is not of
¹⁷ consequence to the final analysis, however the model chosen is shown to be valid over
¹⁸ the whole H_T region of the analysis as shown below.

¹⁹ Maximum likelihood (ML) values for k_{QCD} and \mathcal{A}_{n_b} are found by the final likelihood
²⁰ fit, however k_{QCD} is first constrained by a measurement in a background enriched side
²¹ band regions where either the α_T cut is relaxed or the R_{miss} cut is inverted. Figure 7.6
²² depicts the regions where k_{QCD} is measured, the signal region is as described before
²³ where $\alpha_T > 0.55$ and $R_{miss} < 1.25$ are required. Region B is defined by the inversion
²⁴ of the α_T cut. Region C is defined by inverting both the α_T requirement and the R_{miss}
²⁵ requirement, this region is further divided in to three slices in α_T of $0.52 < \alpha_T < 0.53$,
²⁶ $0.53 < \alpha_T < 0.54$ and $0.54 < \alpha_T < 0.55$, as the index of C_i rises the expected amount of
²⁷ QCD in that control region increases. Finally region D has only the R_{miss} requirement

- ¹ inverted, region D is not used to constrain k_{QCD} , but instead to check the validity of the exponential model. The fits to the individual side bands are shown in Appendix B. The

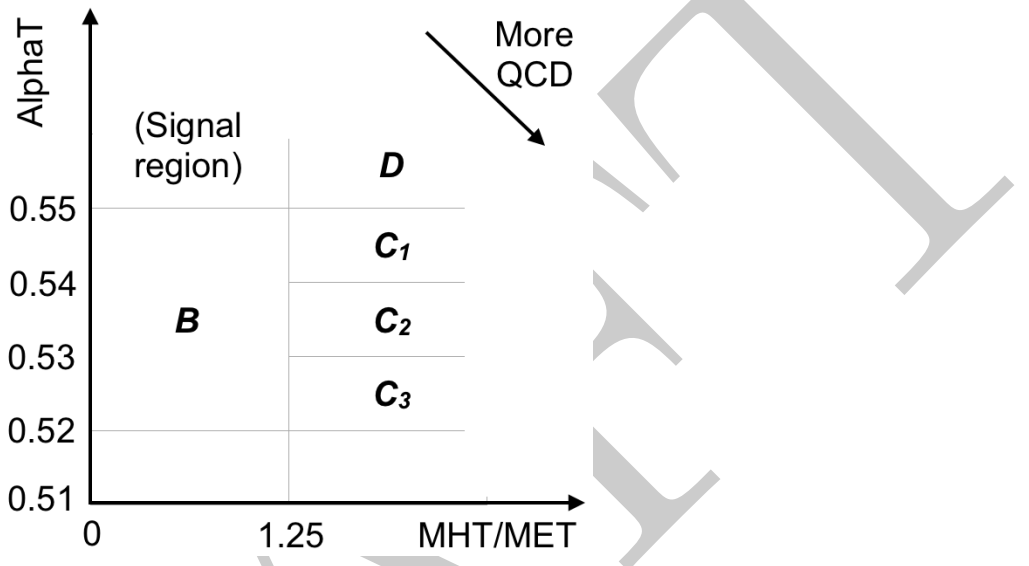


Figure 7.6.: QCD side-band regions, used for determination of k_{QCD} .

- ²
³ best fit value for k_{QCD} of $2.96 \pm 0.64 \times 10^{-2} \text{ GeV}^{-1}$ obtained from region B is used as
⁴ the central value of the constraint. The assumption that this method gives an unbiased
⁵ estimate of k_{QCD} stems from the similarity in event kinematics in the two α_T regions. The
⁶ best fit values for the three C_i regions are used to estimate the systematic uncertainty on
⁷ the central value obtained from region B . The fit results show now dependance on the α_T
⁸ region used to measure the number of events, supporting the assumption that region B
⁹ provides an unbiased estimate of k_{QCD} . The variation of the measured values for each C_i
¹⁰ slice are used to calculate the error on the central value, the weighted mean and standard
¹¹ deviation of the three slices in α_T are calculated to be $1.13 \pm 0.26 \times 10^{-2} \text{ GeV}^{-1}$, the
¹² relative error on this value is 20% which is then applied to the central value to give an
¹³ estimate of the systematic uncertainty.

- ¹⁴ The data side bands are used to provide a constrained value of k_{QCD} as an input to
¹⁵ the final likelihood model which describes the expected number of background events in
¹⁶ bins of H_T and the number of observed jets containing a b quark. The value measured for
¹⁷ k_{QCD} is $2.96 \pm 0.61(\text{stat}) \pm 0.46(\text{sys}) \times 10^{-2} \text{ GeV}^{-1}$. The uncertainty values are used
¹⁸ as penalty timers in the likelihood model which is described in Section 7.5

- ¹⁹ A final check is performed using region D , which requires $\alpha_T > 0.55$ but has no
²⁰ R_{miss} cut, this introduces QCD background in to the signal region. The likelihood fit

Table 7.4.: Best fit values for the parameters k as obtained from the regions B , C_1 , C_2 , and C_3 . The latter three measurements are used to calculate a weighted mean (identified as region C). Also quoted is the maximum likelihood value of the parameter k given by the simultaneous fit using the sample defined by region D . Quoted errors are statistical only. From [1].

Side-band region	k_{QCD} ($\times 10^{-2}$ GeV $^{-1}$)	p-value
B	2.96 ± 0.64	0.24
C_1	1.19 ± 0.45	0.93
C_2	1.47 ± 0.37	0.42
C_3	1.17 ± 0.55	0.98
C (weighted mean)	1.31 ± 0.26	-
D (likelihood fit)	1.31 ± 0.09	0.57

is performed on this background enriched region and no constraint is applied on k_{QCD} which is then determined by the fit only. The fit is performed over the full H_T range used in the final analysis. Figure 7.7 shows the resulting fit, the ML value obtained for k_{QCD} is $(1.31 \pm 0.09) \times 10^{-2}$ GeV $^{-1}$, this value is in excellent agreement with the value found from the weighed mean of the regions C_i , secondly the fit shows that the choice of exponential function used in the likelihood model is valid over the entire H_T range. This supports the assumption that region B provides an unbiased estimate of k_{QCD} in the signal region $\alpha_T > 0.55$ and $R_{miss} < 1.25$.

7.5. Likelihood model

Declaration The likelihood model was implemented, developed, commissioned and deployed in anger by Edward Laird and is best described in his thesis[45]. However for completeness the likelihood model is described in this section. The likelihood is used to gauge the agreement between the observed yields in the hadronic signal region and the predicted yields obtained from the control samples. For the hadronic sample the likelihood is as follows, for N bins in H_T , let n_i represent the observed hadronic yield in H_T bin i , the likelihood for observing n_i events is then

$$L_{had} = \prod_i Pois(n_i | b_i + s_i) \quad (7.3)$$

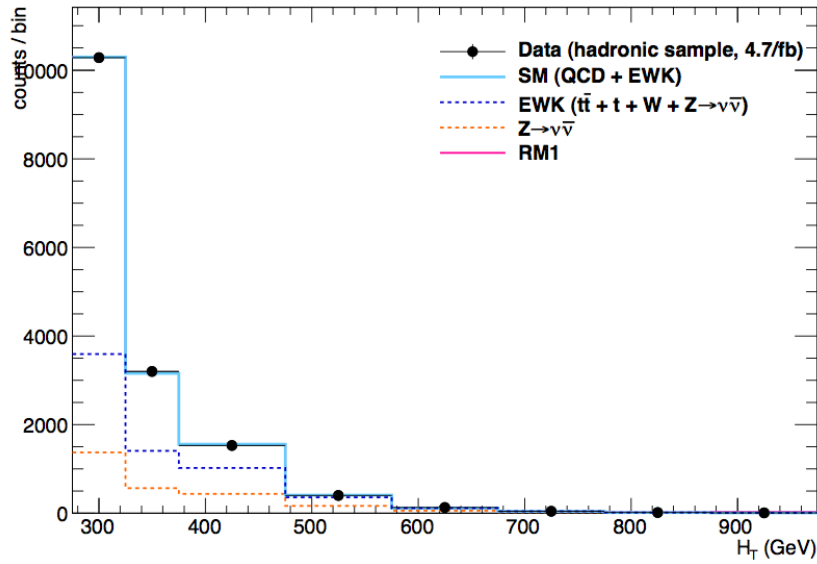


Figure 7.7.: Comparison of the observed yields and SM expectations given by the simultaneous fit in bins of H_T for the side-band region D . No requirement on the number of b jets is made. Shown are the observed event yields in data (black dots with error bars representing the statistical uncertainties) and the expectations given by the simultaneous fit for the $Z \rightarrow \nu\nu + \text{jets}$ process (orange dotted-dashed line); the sum of all processes with genuine \cancel{E}_T , which are primarily $t\bar{t}$, $W + \text{jets}$, and $Z \rightarrow \nu\nu + \text{jets}$ (dark blue long-dashed line); and the sum of QCD and all aforementioned SM processes (light blue solid line).[1]

where b_i is the number of expected background events and s_i the expected signal yield, which is dependant on the signal model being considered. Pois refers to the Poisson distribution of these values, b_i is equal to the sum of electro-weak events expected plus the number of QCD events ($b_i = EWK_i + QCD_i$) expected per bin.

In Section 7.4 it was shown that the QCD contribution can be modelled as an exponentially falling as a function of H_T .

$$R_{\alpha_T}(H_T) = A_{qcd} e^{-k_{QCD} H_T} \quad (7.4)$$

Where A_{QCD} and k_{QCD} have been constrained by measurements in the control regions. QCD_i is then given as:

$$QCD_i = m_i A_{qcd} e^{-k_{QCD} \langle H_T \rangle^i}. \quad (7.5)$$

Where m_i is the number of events per H_T bin which fail $\alpha_T > 0.55$ and $\langle H_T \rangle^i$ is the mean H_T of the the bin.

For the electro-weak background two components are considered, f_{Zinv}^i represents the fraction of the total electro-weak background contributed by $Z \rightarrow \nu\nu + \text{Jets}$ events. This is modelled as a liner component:

$$f_{Zinv}^i = f_{Zinv}^0 + \frac{\langle H_T \rangle^i - \langle H_T \rangle^0}{\langle H_T \rangle^{N-1} - \langle H_T \rangle^0} (f_{Zinv}^{N-1} - f_{Zinv}^i), \quad (7.6)$$

where f_{Zinv}^i and f_{Zinv}^{N-1} are floating parameters who's final values are limited between zero and one. The total number of $Z \rightarrow \nu\nu + \text{Jets}$ events per bin is then given by:

$$Z_{inv}^i = f_{Zinv}^i \times EWK^i \quad (7.7)$$

with the remaining background from other electro-weak processes given by:

$$Y = (1 - f_{Zinv}^i) \times EWK^i. \quad (7.8)$$

In each H_T bin i there are three background measurements, n_γ^i , n_μ^i and $n_{\mu\mu}^i$, representing the event counts from the photon, muon and di-muon control samples respectively, each of these yields has a Montecarlo counter-part yield. From the Montecarlo it is also possible to extract MC_{Zinv}^i and MC_Y^i . After defining:

$$r_\gamma^i = \frac{MC_\gamma^i}{MC_{Zinv}^i}, \quad r_{\mu\mu}^i = \frac{MC_{\mu\mu}^i}{MC_{Zinv}^i}, \quad r_\mu^i = \frac{MC_\mu^i}{MC_Y^i} \quad (7.9)$$

three likelihood functions are defined:

$$L_\gamma = \prod_i Pois \left(n_\gamma^i | \rho_{\gamma Z}^j \cdot r_\gamma^i \cdot Z_{inv}^i \right), \quad (7.10)$$

$$L_{\mu\mu} = \prod_i Pois \left(n_{\mu\mu}^i | \rho_{\mu\mu Z}^j \cdot r_{\mu\mu}^i \cdot Z_{inv}^i \right), \quad (7.11)$$

$$L_\mu = \prod_i Pois \left(n_\mu^i | \rho_{\mu Y}^j \cdot r_\mu^i \cdot Y^i + s_\mu^i \right), \quad (7.12)$$

Equation (7.10) is used to estimate the ML values for Z_{inv} which is the expectation of the number of $Z \rightarrow \nu\nu + \text{Jets}$ events in the hadronic signal region using the observations n_γ^i in the photon control sample and the ratio r_γ^i , similarly the number of $Z \rightarrow \nu\nu + \text{Jets}$

Table 7.5.: The systematic parameters used in H_T bins.

H_T bin (i)	0	1	2	3	4	5	6	7
syst. parameter (j)	0	0	0	0	1	1	2	2

events expected in the signal region predicted by the $Z \rightarrow \mu\mu + \text{Jets}$ are found using Equation (7.11). The non $Z \rightarrow \nu\nu$ backgrounds are estimated by the ML value for Equation (7.12) in a similar way with the addition of s_μ^i which represents the signal contamination in the single muon control sample. The measurements and ratios are considered simultaneously though the relationships defined in Equations (7.3), (7.7) and (7.8). The ratios $r_\gamma^i, r_{\mu\mu}^i$ and r_μ^i are the inverse of the translation factors given by Equation (7.1). The parameters $\rho_{\gamma Z}, \rho_{\mu\mu Z}$ and $\rho_{\mu Y}$ are correction factors that account for the systematic uncertainty on each of the ratios and $\sigma_{\gamma Z}, \sigma_{\mu\mu Z}$ and $\sigma_{\mu Y}$ represent the relative systematic uncertainties for the control sample constraints, these are accounted for in:

$$L_{EWK \ syst} = \prod_j Gaus(1.0 | \rho_{\mu Y}^j, \sigma_{\mu Y}^j) \times Gaus(1.0 | \rho_{\mu\mu Z}^j, \sigma_{\mu\mu Z}^j) \times Gaus(1.0 | \rho_{\gamma Z}^j, \sigma_{\gamma Z}^j) \quad (7.13)$$

- ¹ Three parameters per control sample are used to cover the eight H_T bins as show in
- ² Table 7.5.

Alternatively the single muon control sample can be used to constrain the total electro-weak background, we can define:

$$r_\mu^{i'} = \frac{MC_\mu^i}{MC_{tot}^i} \quad (7.14)$$

and

$$L'_\mu = \prod_i Pois(n_\mu^i | \rho_{\mu Y} \times r_\mu^{i'} \times EWK^i + s_\mu^i) \quad (7.15)$$

Signal Contamination The cross section for each model is represented by x , l represents the total recorded luminosity considered by the analysis in the signal region. The efficiency is defined as ϵ_{had}^i for the signal region and ϵ_μ^i for the single muon control sample, δ represents the relative uncertainty on signal measured in the previous section, δ is taken

to be fully correlated though the H_T bins. ρ_{sig} is the correction factor to the signal yield which accommodates this uncertainty. f represents an unknown multiplicative factor on the signal cross section, for which an allowed interval is computed. The expected signal yield s^i from Equation (7.3) is defined as:

$$s_{had}^i = f \rho_{sig} x l \epsilon_{had}^i, \quad (7.16)$$

the signal contamination s_μ^i is given by:

$$s_\mu^i = f \rho_\mu x l \epsilon_\mu^i. \quad (7.17)$$

The systematic on signal uncertainty is included by in an additional term in the likelihood:

$$L_{sig} = Gaus(1.0 | \rho_{sig}, \delta). \quad (7.18)$$

The total likelihood The total likelihood for a given signal selection $k(H_T, n_b)$ is given by:

$$L^k = L_{had}^k \times L_\mu^k \times L_\gamma^k \times L_{\mu\mu}^k, \quad (7.19)$$

each k has $3 + N$ nuisance parameters; $\mathcal{A}_{QCD}, f_{Zinv}^0, f_{Zinv}^{N-1}, \{EWK^i\}_{i=0}^{N-1}$. The 11 parameters k_{QCD}, ρ_{sig} , and $\rho_{\gamma Z}^k, \rho_{\mu\mu}^k, \rho_\mu^k$ with $j = \{0, 1, 2\}$ are shared between the selections, the total likelihood is then given as:

$$L = L_{sig} \times L_{EWKsyst} \times \prod_k L_{had}^k \times L_\mu^k \times L_\gamma^k \times L_{\mu\mu}^k. \quad (7.20)$$

7.6. Final Results

2 The yields obtained in the hadronic signal regions are tested for their compatibility with
 3 the background predicted by the likelihood model both in terms of agreement with the
 4 Standard Model and interpretations in the forms of limits on new physics models.

5 To test the level of agreement with the standard model the signal terms are dropped
 6 from the likelihood, which is then maximised over all parameters using **Roofit**[46] and
 7 **MINUIT**[47]. The individual yields and errors from the fits are shown in Appendix

8 put these tables in teh appendix

¹ . The total background and data yields and their errors as given by the ML fit are
² show below in Table 7.6.

Table 7.6.: Comparison of the measured yields in the different H_T and b jet multiplicity bins for the hadronic sample with the SM expectations and combined statistical and systematic uncertainties given by the simultaneous fit.

H_T (GeV)	275–325	325–375	375–475	475–575	575–675	675–775	775–875	875– ∞
0 b jets SM	2933^{+56}_{-52}	1139^{+17}_{-40}	783^{+17}_{-27}	261^{+14}_{-8}	$81.5^{+6.5}_{-6.5}$	$34.2^{+4.0}_{-3.8}$	$10.4^{+2.8}_{-1.8}$	$5.3^{+1.7}_{-1.1}$
0 b jets Data	2919	1166	769	255	91	31	10	4
1 b jet SM	630^{+26}_{-25}	271^{+10}_{-16}	202^{+10}_{-6}	$78.0^{+6.9}_{-1.9}$	$24.2^{+2.9}_{-2.0}$	$10.6^{+1.7}_{-1.3}$	$2.9^{+0.9}_{-0.5}$	$2.2^{+0.7}_{-0.4}$
1 b jet Data	614	294	214	71	20	6	4	0
2 b jets SM	162^{+13}_{-12}	$61.8^{+4.8}_{-6.3}$	$58.8^{+4.8}_{-2.6}$	$28.0^{+3.5}_{-1.1}$	$9.0^{+1.4}_{-1.0}$	$7.1^{+1.4}_{-1.0}$	$0.6^{+0.3}_{-0.2}$	$0.9^{+0.4}_{-0.2}$
2 b jets Data	160	68	52	19	11	7	0	2
≥ 3 b jets SM	$10.5^{+3.5}_{-2.2}$	$7.1^{+2.2}_{-1.8}$	$5.8^{+1.4}_{-0.9}$	$3.1^{+1.0}_{-0.7}$	$1.7^{+0.5}_{-0.4}$	$0.7^{+0.5}_{-0.4}$	$0.1^{+0.1}_{-0.1}$	$0.2^{+0.1}_{-0.1}$
≥ 3 b jets Data	10	8	8	1	0	0	0	0

³ Figures 7.8, 7.9, 7.10 and 7.11 show comparisons of the observed yields and the
⁴ Standard Model only expectations given by the simultaneous fit for 0, 1, 2, ≥ 3 exclusive
⁵ b-tag bins. A good agreement with the standard model is observed in all H_T and b-tag
⁶ categories. Given the lack of a signal like observation limits are set on the production
⁷ masses and cross sections of beyond the standard model particles.

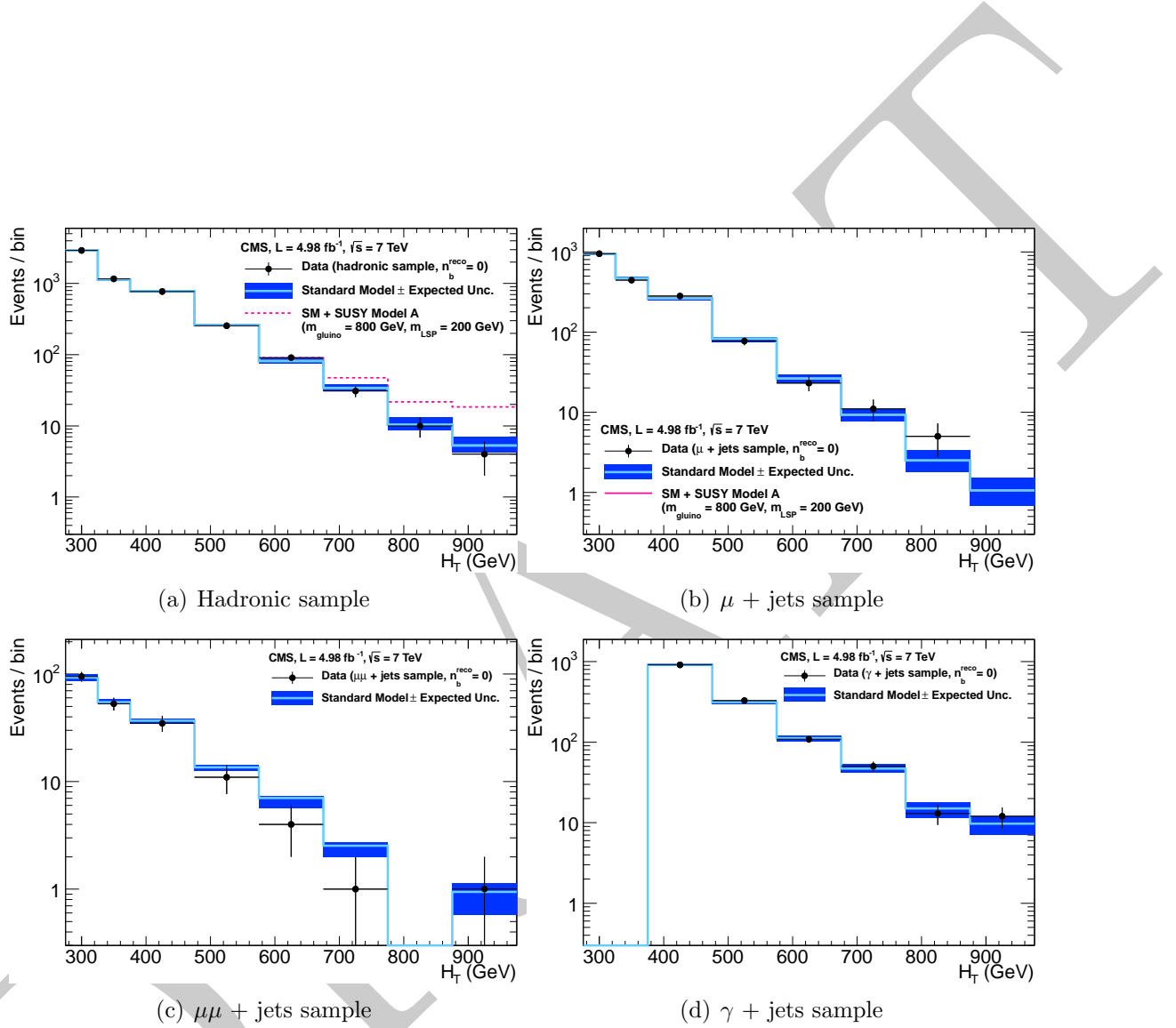


Figure 7.8.: Comparison of the observed yields and SM expectations given by the simultaneous fit in bins of H_T for the (a) hadronic, (b) $\mu +$ Jets, (c) $\mu\mu +$ Jets and (d) $\gamma +$ Jets samples when requiring exactly zero reconstructed b-jets. The observed event yields in data (black dots) and the expectations and their uncertainties, as determined by the simultaneous fit, for all SM processes (light blue solid line with dark blue bands) are shown. For illustrative purposes only, an example signal model is superimposed on the SM expectation (magenta solid line). The expected signal contamination in the control samples is negligible.

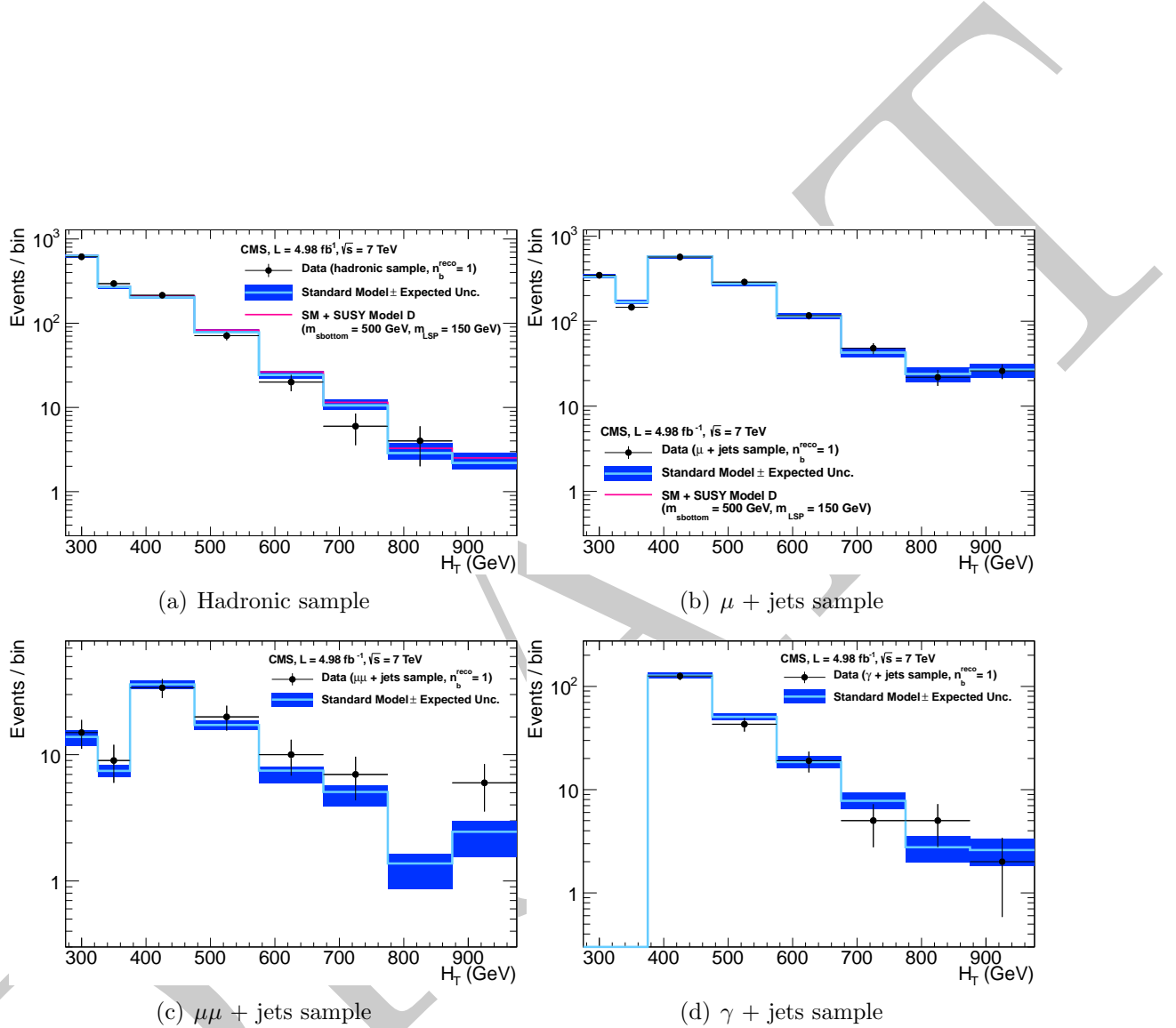


Figure 7.9.: Comparison of the observed yields and SM expectations given by the simultaneous fit in bins of H_T for the (a) hadronic, (b) $\mu +$ Jets, (c) $\mu\mu +$ Jets and (d) $\gamma +$ Jets samples when requiring exactly one reconstructed b-jet. The observed event yields in data (black dots) and the expectations and their uncertainties, as determined by the simultaneous fit, for all SM processes (light blue solid line with dark blue bands) are shown. For illustrative purposes only, an example signal model is superimposed on the SM expectation (magenta solid line). The expected signal contamination in the control samples is negligible.

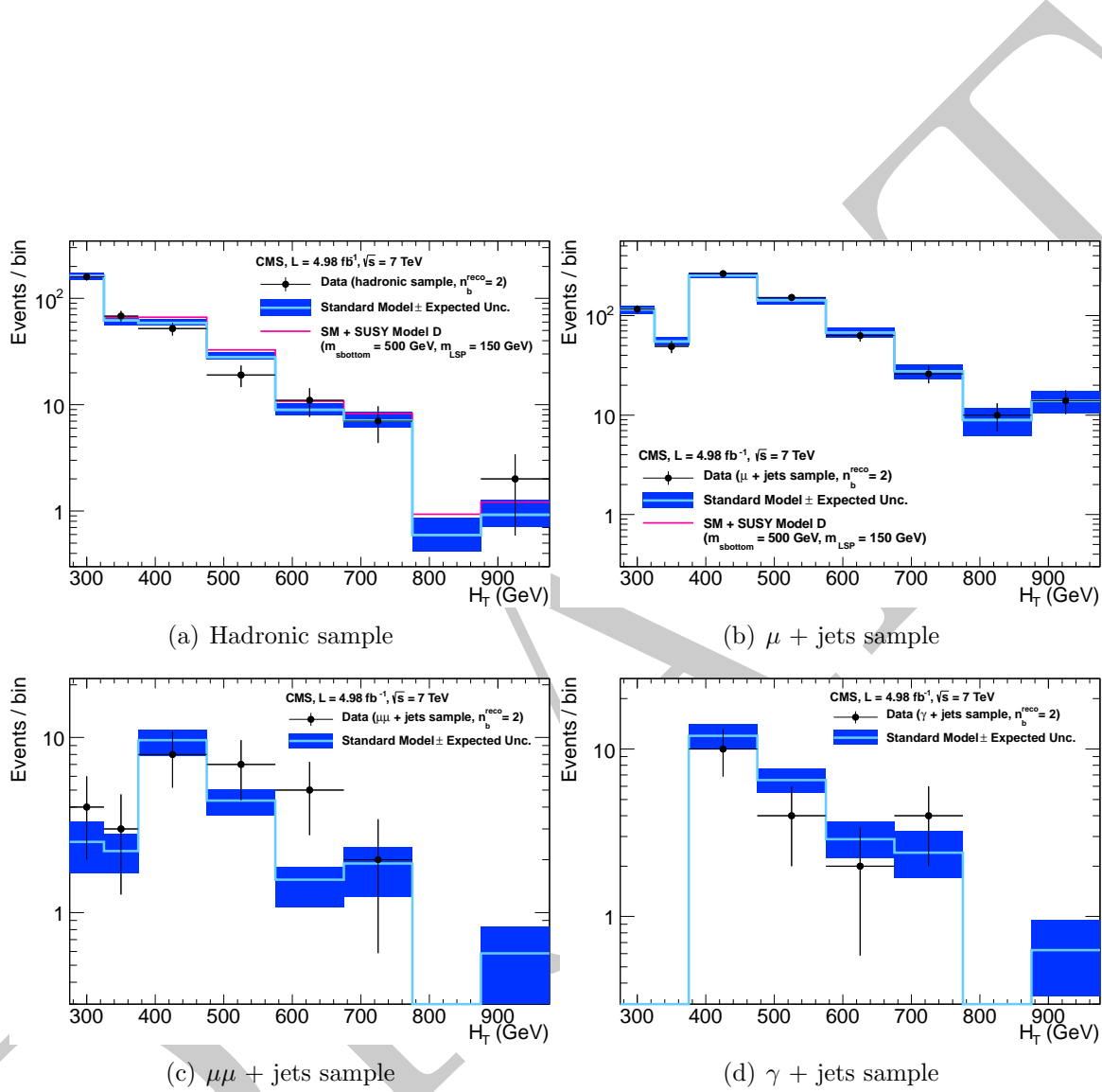


Figure 7.10.: Comparison of the observed yields and SM expectations given by the simultaneous fit in bins of H_T for the (a) hadronic, (b) $\mu +$ Jets, (c) $\mu\mu +$ Jets and (d) $\gamma +$ Jets samples when requiring exactly two reconstructed b-jets. The observed event yields in data (black dots) and the expectations and their uncertainties, as determined by the simultaneous fit, for all SM processes (light blue solid line with dark blue bands) are shown. For illustrative purposes only, an example signal model is superimposed on the SM expectation (magenta solid line). The expected signal contamination in the control samples is negligible.

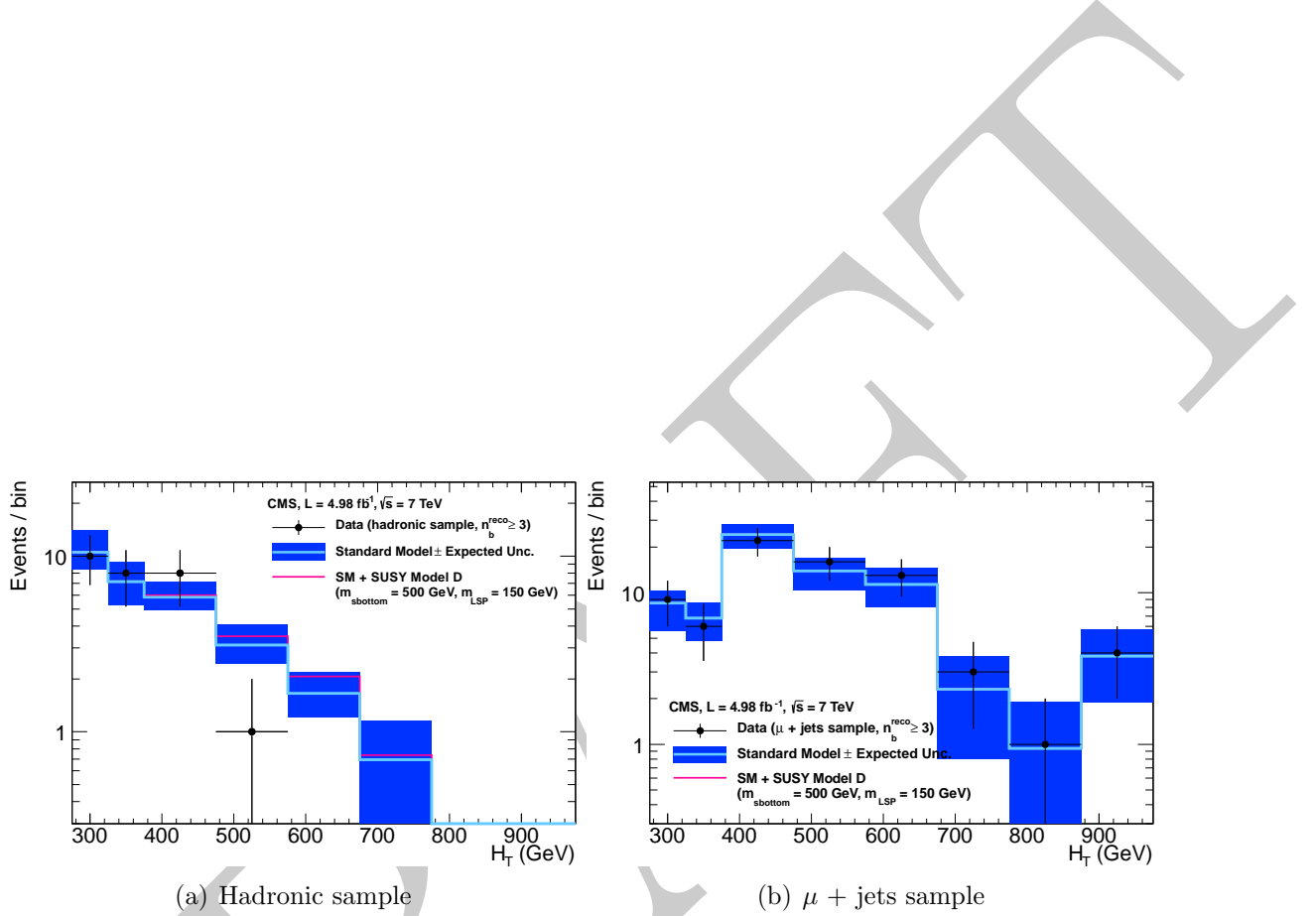


Figure 7.11.: Comparison of the observed yields and SM expectations given by the simultaneous fit in bins of H_T for the (a) hadronic and (b) $\mu +$ Jets samples when requiring at least three reconstructed b-jets. The observed event yields in data (black dots) and the expectations and their uncertainties, as determined by the simultaneous fit, for all SM processes (light blue solid line with dark blue bands) are shown. For illustrative purposes only, an example signal model is superimposed on the SM expectation (magenta solid line). The expected signal contamination in the $\mu +$ Jets control sample is negligible.

Chapter 8.

¹ Interpretation

² 8.1. Signal Models

³ The level of agreement of the analysis with the SM give a handle on the production
⁴ cross sections and masses of particles predicted by new physics models. The final results
⁵ are presented in terms of a specific SUSY model and a selection of generic final state
⁶ topologies, known as Simplified Model Spectra (SMS).

⁷ The SUSY model considered is the CMSSM[] which is described in Section 2.2.1, the
⁸ parameters chosen are $\tan \beta = 3$, $A_0 = 0\text{GeV}$, $\mu > 0$ with the exclusion curve presented
⁹ in the m_0 , $m_{1/2}$ plane. This model combines many production and decay topologies and
¹⁰ is common to results shown by previous and contemporary experiments []

¹¹ Reference ATLAS and Tevatron susy results

¹² . The results are also presented in terms of SMS[] models, these are models with
¹³ single production methods and a specified decay topology. The CMS terminology for
¹⁴ the production methods are as follows: T1 models are gluino-gluino production, which
¹⁵ then decay to four SM hadronic jets and two neutralinos. T2 models are squark-squark
¹⁶ production with decays to two SM hadronic jets and two neutralinos. These topologies
¹⁷ can be further specialised by enforcing the squarks or gluinos to decay to heavy flavour
¹⁸ SM quarks, such as t, which promptly decay to jets containing b quarks or direct decays
¹⁹ to b quarks. The limits on the SMS space are defined in terms of the mass splitting
²⁰ between the neutralino and the pair produced SUSY particle defining the model.

¹ 8.2. Signal Efficiency

² 8.2.1. CMSSM

³ The CMSSM signal scan is composed of eight sub-processes which define the production
⁴ and decay topologies. The dominant process varies with $m_0, m_{1/2}$ and at next to leading
⁵ order the cross section for each of these processes varies per point. The analysis is run
⁶ over each sub process in turn with the final efficiency given by the weighted sum of the
⁷ subprocess efficiencies. The yield per point is then given by $\epsilon \times \mathcal{L}$ for 5 fb^{-1} the total
⁸ yields are shown in the appendix in Figure D.1 these yields are for the sum of the H_T
⁹ analysis bins.

¹⁰ 8.2.2. Simplified Models

¹¹ The SMS models contain only one production process and a set decay topology, making
¹² the interpretation in these models simpler, however the individual models are not
¹³ representative of some complete SUSY model. Instead these models allow the testing of
¹⁴ specific facets of new physics models, with out the ambiguity of the relative contributions
¹⁵ of each sub process at a point which is seen when testing full models. The efficiency
¹⁶ is measured for each of the models, with the yield per point given by $\epsilon \times \sigma \times \mathcal{L}$ where
¹⁷ σ is given as a reference cross section only. The efficiencies for which are shown in the
¹⁸ appendix, Table 8.1 lists which figure corresponds to which model, it is to be noted that
¹⁹ the total efficiency summed over H_T bins is shown.

Table 8.1.: Production and decay modes for various simplified models.

Model	Production and decay modes	Figure showing efficiency
T1	$\tilde{g}\tilde{g} \rightarrow q\bar{q}\tilde{\chi}^0 q\bar{q}\tilde{\chi}^0$	D.2
T2	$\tilde{q}\tilde{q} \rightarrow q\tilde{\chi}^0 \bar{q}\tilde{\chi}^0$	D.3
T2tt	$\tilde{t}\tilde{t} \rightarrow t\tilde{\chi}^0 \bar{t}\tilde{\chi}^0$	D.4
T2bb	$\tilde{b}\tilde{b} \rightarrow b\tilde{\chi}^0 \bar{b}\tilde{\chi}^0$	D.5
T1tttt	$\tilde{g}\tilde{g} \rightarrow t\bar{t}\tilde{\chi}^0 t\bar{t}\tilde{\chi}^0$	D.6
T1bbbb	$\tilde{g}\tilde{g} \rightarrow b\bar{b}\tilde{\chi}^0 b\bar{b}\tilde{\chi}^0$	D.7

²⁰ **Signal Efficiency for the Background Selection** If the couplings of the SUSY
²¹ particles are analogous to the SM particles then the final states may involve muons

which in the presence of signal would infer an over estimation of the background from the control samples. To measure this the background selection is applied to the signal models and the yields are taken into account in the final limit setting procedure. On average the background selection’s efficiency on signal is $10\times$ lower than the efficiency in the hadronic signal region. This is shown for the model T1tttt in Figure D.8 where the most muons of all the signal models are expected in the final state, the contamination in the n_b bins that drive the limit is on the order of $10 - 20\%$.

8.3. Uncertainty on Signal Efficiency

The systematic uncertainty on the signal models is due to: Choice of PDF at generator level, the PDF set used to generate the sample has effects on both the acceptance and the cross section; The measurement of the integrated luminosity is accounted for in the signal yield; Due to the signal models being created with CMS FastSim[] rather than CMS FullSim[] the acceptance differs between the signal and the background samples; The error on the jet energy scale is accounted for on the signal yield; Systematic errors from the cleanings cuts (R_{miss} and ECAL dead regions) and lepton/photon vetoes are also taken in to account; Finally corrections to the b-tagging efficiency between the FullSim and the FastSim are applied as well as their errors.

Each of these uncertainties is expressed as a percentage change in the efficiency from the central value given by applying the full analysis to each signal model, the total systematic is given by summing the components in quadrature. In the following section the measurements of the error from each of these sources is detailed and summarised per considered signal model at the end of the section.

The uncertainties for the CMSSM are considered in a band of ± 60 GeV in $m_{1/2}$ around the expected limit to confine the errors to the relevant part of the plane, in the very high $m_0, m_{1/2}$ area the jet energy scale causes large fluctuations due to the small mass splitting between the SUSY particles. For the SMS models two regions are defined, one “close” to the diagonal, which has small mass splitting and thus the effects of jet energy scale and PDF acceptance have a large impact on the analysis efficiency. A second “far” region is defined with large mass splitting and thus a small change on the analysis efficiency due to jet energy scale and PDF variations. The near and far regions

are defined by:

$$m_{sq}(m_{gl}) - m_{lsp} > 350 \text{ GeV and } m_{sq}(m_{gl}) > 475 \text{ GeV} \quad (8.1)$$

- ₁ events passing these conditions are classified as being in the “far” region, those failing in
₂ the “close” region.

₃ 8.4. Choice of PDF set at generator level.

₄ The PDF set contains information on the interaction probabilities of the quark and gluons
₅ in the proton at different energies, the model used in the production of the Montecarlo
₆ simulation has direct impact on the kinematics of the final states, since the PDFs have
₇ been measured at lower energies than those found at the LHC the quark and gluon
₈ distributions have been extrapolated from the low energy regime, the uncertainty at high
₉ energy is thus significant. The uncertainties on acceptance due to the choice of PDF set
₁₀ used to generate the signal Montecarlo are calculated in line with the PDF4LHC[48] working
₁₁ group recommendations. On the event level the individual weights are re-calculated by
₁₂ moving between PDF set, the weight is based on the energy at which the quarks or gluons
₁₃ interact and the form given by the PDF. This is done for the central value of the three
₁₄ considered PDF sets (CTEQ6.1[49], MSTW2008nlo68cl[50] and NNPDF2.0[51]) and for
₁₅ the variations of each of their errors. The change in analysis efficiency is measured per
₁₆ H_T bin, Figure 8.1 shows the deviation in efficiency per bin for three examples points
₁₇ in the CMSSM plane, the error bars represent the Root Mean Squared (RMS) of the
₁₈ spread of the efficiency inside each PDF set. It is to be noted that some bins show a large
₁₉ change in efficiency due to the choice of PDF set, however these are low efficiency bins
₂₀ where changes in yield of a few events has a large effect, the final result however is driven
₂₁ by the high efficiency bins, hence these large fluctuations can be ignored. The effects on
₂₂ the cross section are studied by re-calculating the Next to Leading Order (NLO) cross
₂₃ sections of each of the sub processes for each choice of PDF set, this is done centrally by
₂₄ CMS, these changes in cross section are accounted for in the error band on the expected
₂₅ limit.

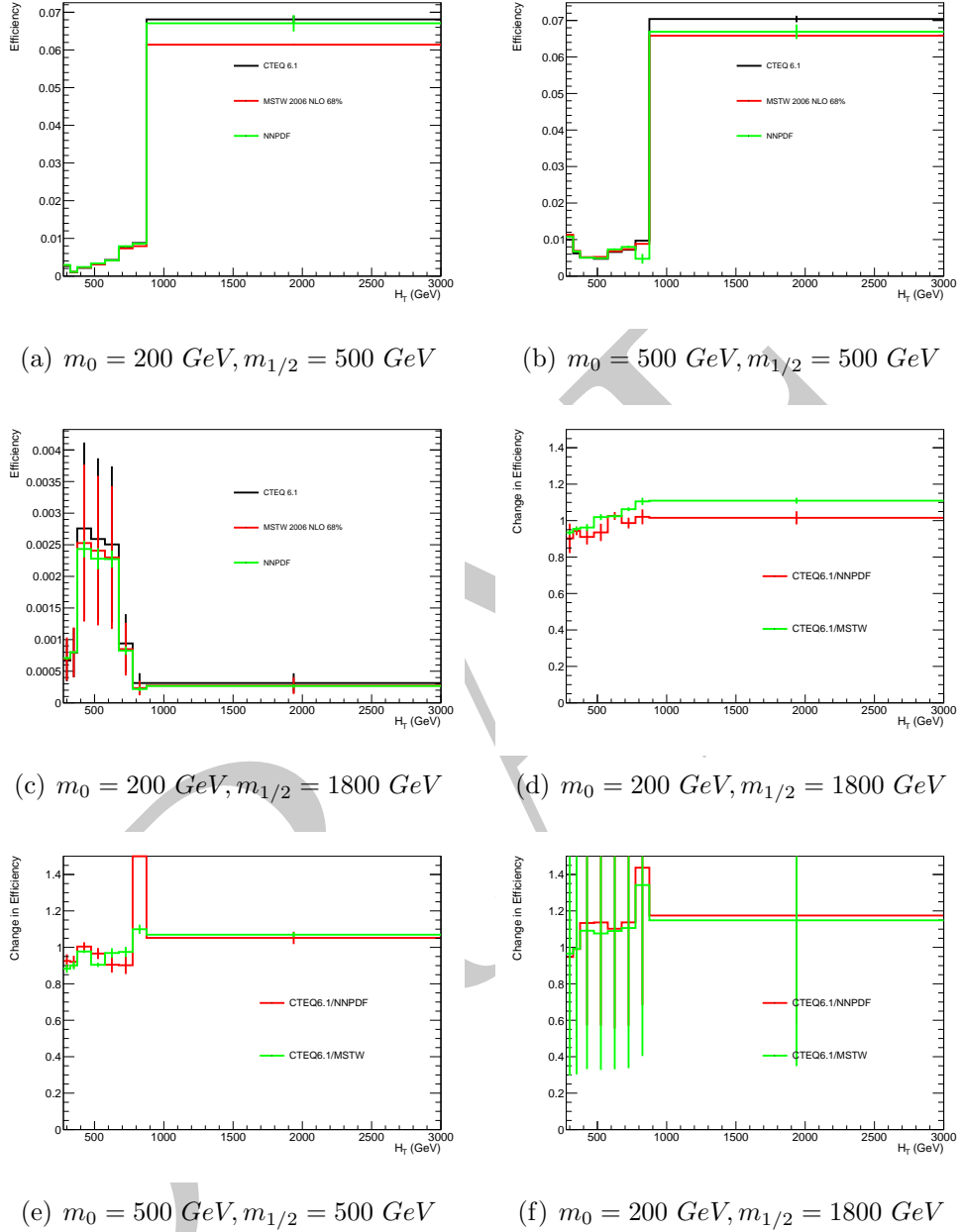


Figure 8.1.: Figures 8.1(a), 8.1(b) and 8.1(c) show the efficiency per H_T bin for the inclusive selection. The three coloured lines represent the analysis efficiency for a choice of PDF set, the error bars are the RMS of the change in efficiency per PDF set from varying the internal components by 1σ of their error. Figures 8.1(d), 8.1(e) and 8.1(f) show the ratio of the change in efficiency from the default PDF set (CTEQ6.1) for three illustrative points in the $m_0, m_{1/2}$ plane of the CMSSM. The change in efficiency in the high efficiency bins is on the order of 10% for all points.

¹ 8.5. Effects of Jet Energy Scale Variations on Signal ² Efficiency

³ Section 6.2.1 describes the JEC and their uncertainties, which are derived in [31], these
⁴ uncertainties are dependant on the $|\eta|$ and E_T of the jet in question. To measure the
⁵ impact of the individual jet energy uncertainties on signal acceptance two additional
⁶ selections are performed on the signal samples, the first with the energy of each jet in
⁷ the event raised from the central value by 1σ of it's uncertainty, the second with the
⁸ energy decreased by 1σ , the relative change in efficiency with respect to the central value
⁹ is then calculated for signal point. The model dependant systematic is found from the
¹⁰ 68th percentile of the 1D distribution of the absolute change in signal efficiency over
¹¹ each point in the model space. Figure E.1 shows the change in efficiency over the full
¹² $m_0, m_{1/2}$ plane for the CMSSM, at high $m_0, m_{1/2}$ the variation is large due to the primary
¹³ production method of SUSY particles being electro-weak production of charginos in this
¹⁴ region. These charginos then decay though a chain to the neutralino and SM particles,
¹⁵ due to the small mass splitting (compressed spectra) between each of the charginos the
¹⁶ jets produced are only just within E_T acceptance. A small change of the individual jet
¹⁷ E_T 's thus moves many jets in and out of acceptance causing a large change in analysis
¹⁸ efficiency, hence only the region within ± 60 GeV around the expected limit in $m_{1/2}$ is
¹⁹ considered when calculating the systematic for the CMSSM. The points close to the
²⁰ diagonal in the SMS models display compressed spectra and so are effected by the change
²¹ in jet energy scale. Figures E.2 and E.3 show the effects of scaling the jet energies
²² for the considered SMS models, Figures E.4 and E.5 show the 68% coverage of the 1D
²³ distribution of the relative change in efficiency for the near and far regions from which
²⁴ the systematic is taken.

²⁵ 8.6. Systematic Uncertainty on Signal Yield from ²⁶ Cleaning Filters and Object Vetoos.

²⁷ For each of the cleaning cuts, R_{miss} and the DeadECAL, the systematic is given as the
²⁸ product of the ratio of normalised yields in the control samples, between data and
²⁹ Montecarlo and the relative change in efficiency due to the cleaning filter for each
³⁰ individual signal model. The background sample is chosen before an α_T cut or any other
³¹ cleaning cuts and is high in real \cancel{E}_T due to the selection of W + Jets and t \bar{t} events,

1 meaning the efficiency of the R_{miss} cut should be high. Figure E.6 shows the accuracy of
2 the R_{miss} modelling, at a cut value of $R_{miss} < 1.25$ the miss modelling is at the level of
3 14%. Figures E.7, E.8 and E.9 show the change in selection efficiency due to the R_{miss}
4 on the signal models.

5 As for the R_{miss} cut the background selection is performed on data and Montecarlo
6 and the accuracy of modelling the DeadECAL filter is measured, the ratio of the nor-
7 malised cut efficiency on data and simulation shows a miss modelling at the level of
8 1.8%, this is taken as the uncertainty on the Montecarlo model of the detector failures.
9 Figures E.11, E.12 and E.13 show the relative change in efficiency due to the DeadECAL
10 filter on the considered signal models.

11 Again regions with compressed spectra and many jet topologies are more effected by
12 the cleaning cuts.

13 Finally the effects of the lepton vetoes on the signal efficiency are studied. A generator
14 level filter is first applied removing any events with final state leptons or photons, thus
15 measuring the effect of hadronic objects faking leptons or photons. The relative change in
16 efficiency due to the application of the object vetoes is show in Figures E.15, E.17 and E.18,
17 the inefficiency for each signal model are very small and are used directly as the systematic
18 error.

19 8.7. Interpretation in terms of new physics models.

20 Due to the lack of a signal like observation limits are set on new physics models. The first
21 of these is the CMSSM, at each point in the $m_0, m_{1/2}$ parameter space the SUSY particle
22 spectrum is calculated using **SoftSUSY**[52], the signal events are generated at leading order
23 using **Pythia 6.4**[53], the Next to Leading Order + Next Leading Log (NLO+NNL)
24 process dependant cross sections are calculated using **PROSPINO**[54] using the **CTEQ6**[49]
25 PDF set. The previously measured errors on the background prediction, total collected
26 luminosity and signal yield are included in the calculation of the limit. Although signal
27 contributions from each data observation (hadronic, $\mu + \text{Jets}$, $\mu\mu + \text{Jets}$ and $\gamma + \text{Jets}$)
28 are included, the only relevant signal contribution to the CMSSM is from the hadronic
29 signal regions. Figure 8.2 shows the expected limit contour with it's associated $\pm 1\sigma$
30 error band as well as the observed limit. The limit is calculated using NLO+NNL cross
31 sections using **CL_s**[55], the limit presented is for the 95% confidence level. For the choice

of $\tan \beta = 10$, $A_0 = 0$ GeV, $\mu > 0$ and a top quark mass $m_{top} = 173.2$ GeV, squarks with masses below 1.25 TeV are excluded at 95% confidence, gluinos with a mass up to 1.25 TeV are also excluded when $m_0 < 600$ GeV. In the region $m_0 > 600$ GeV gluino masses below 700 GeV are excluded as are squarks with masses between 1.25-2.5 TeV, m_0 dependant.

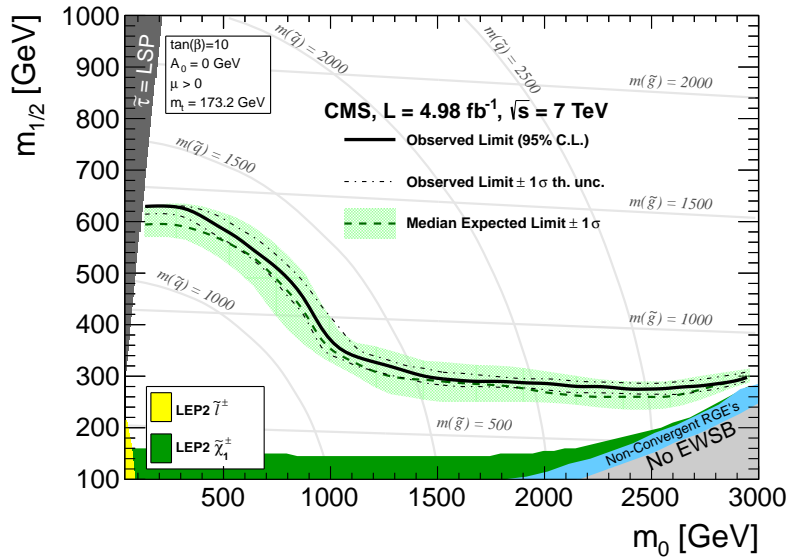


Figure 8.2.: Exclusion contours at 95% CL in the CMSSM ($m_0, m_{1/2}$) plane ($\tan \beta = 10, A_0 = 0, \mu > 0$) calculated with NLO+NNL SUSY production cross sections and the CL_s method. The solid black line indicates the observed exclusion region. The dotted-dashed black lines represent the observed excluded region when varying the cross section by its theoretical uncertainty. The expected median exclusion region (green dashed line) $\pm 1\sigma$ (green band) are also shown.

The observed yields are also used to set limits on SMS models. This allows interpretation of the results for defined mass splittings and final states. Each SMS sample is characterised by the SUSY particle which is pair produced, either a squark or a gluino and the LSP mass, the individual points are then defined by the mass difference between the pair produced particle and the LSP. The decay topologies are further specialised by enforcing the final state quarks to be heavy flavours, either top or bottom quarks. The decays of the considered models are summarised in Table 8.2 As before the experimental uncertainties on the background estimation, collected luminosity, and the model dependant signal uncertainties are accounted for in the calculation of the limit.

In the regions $m_{\tilde{q}(\tilde{g})} - m_{LSP} < 200$ GeV and $m_{\tilde{q}(\tilde{g})} < 350$ GeV any selection efficiency is strongly dependant on the presence of initial state radiation which is not well modelled in the Montecarlo simulation, hence these regions are not considered when setting limits

in the SMS models, for the model T1tttt the ignored region is expanded to cover $m_{\tilde{g}} - m_{LSP} < 400$ GeV.

Figure 8.3 shows the observed limits at 95% confidence level obtained using CL_s as a function of $m_{\tilde{q}(\tilde{g})}$ and m_{LSP} . The solid black lines represent the observed median limit assuming NLO+NNL[54, 56] SUSY cross sections for squark pair production in the limit of de-coupled gluinos and vice versa for the gluino production models. The thin black lines represent the limit when this cross section is varied by $\pm 1\sigma$ of the theoretical uncertainty, the dashed purple lines represent the expected limit and its $\pm 1\sigma$ uncertainty.

The best limits are set on the mass of the pair produced sparticles are at low m_{LSP} due to the large mass splitting between the sparticles and the LSP producing high p_T final state objects. The limits degrade as the decay spectra become compressed, above a certain m_{LSP} no limit is set.

No exclusion on direct stop, stop production (T2tt) is expected assuming the NLO+NNL production cross section for $m_{LSP} > 50$ GeV. Figure 8.4 shows the observed upper limit at 95% confidence level on the cross section as a function of m_{stop} for an LSP with a mass of 50 GeV.

Table 8.2.: Production and decay modes for various simplified models.

Model	Production and decay modes	Figure showing limit
T1	$\tilde{g}\tilde{g} \rightarrow q\bar{q}\tilde{\chi}^0 q\bar{q}\tilde{\chi}^0$	8.3(a)
T2	$\tilde{q}\tilde{q} \rightarrow q\tilde{\chi}^0 \bar{q}\tilde{\chi}^0$	8.3(b)
T2tt	$\tilde{t}\tilde{t} \rightarrow t\tilde{\chi}^0 \bar{t}\tilde{\chi}^0$	8.3(c), 8.4
T2bb	$\tilde{b}\tilde{b} \rightarrow b\tilde{\chi}^0 \bar{b}\tilde{\chi}^0$	8.3(d)
T1tttt	$\tilde{g}\tilde{g} \rightarrow t\bar{t}\tilde{\chi}^0 t\bar{t}\tilde{\chi}^0$	8.3(e)
T1bbbb	$\tilde{g}\tilde{g} \rightarrow b\bar{b}\tilde{\chi}^0 b\bar{b}\tilde{\chi}^0$	8.3(f)

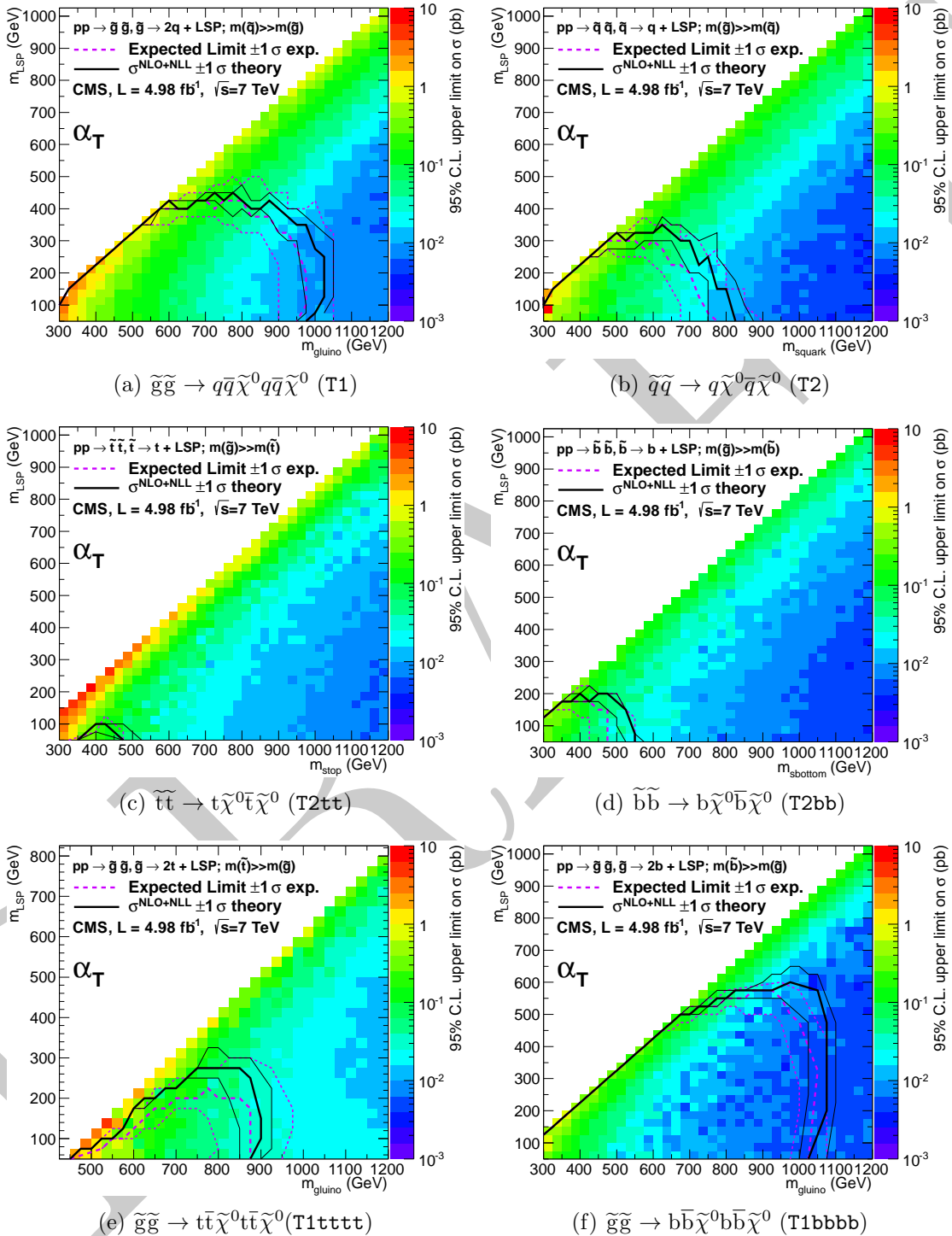


Figure 8.3.: Upper limit on cross section at 95% CL as a function of $m_{\tilde{q}}$ or $m_{\tilde{g}}$ and m_{LSP} for various simplified models. The solid thick black line indicates the observed exclusion region assuming NLO+NLL SUSY production cross section. The thin black lines represent the observed excluded region when varying the cross section by its theoretical uncertainty. The dashed purple lines indicate the median (thick line) $\pm 1\sigma$ (thin lines) expected exclusion regions.

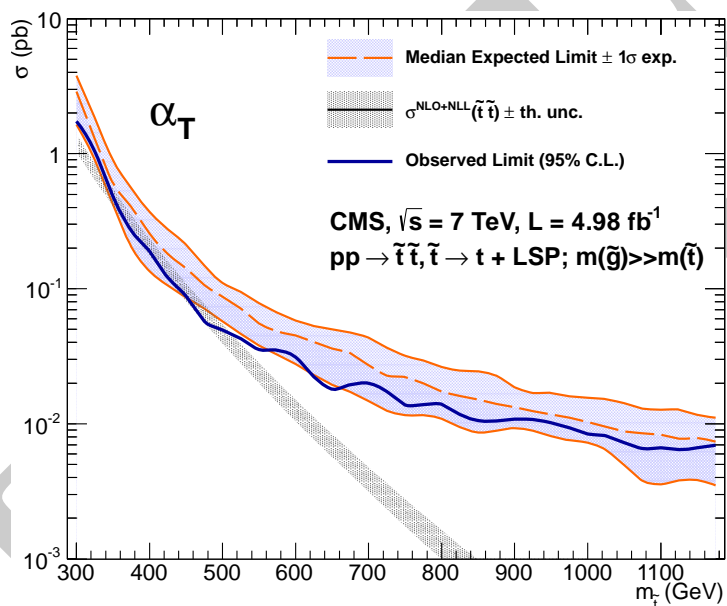


Figure 8.4.: Excluded cross section versus top squark mass for a model in which pair-produced top squarks decay to two top quarks and two neutralinos. The solid blue line indicates the observed cross section upper limit (95% CL) as a function of the top squark mass, $m_{\tilde{t}}$. The dashed orange line and blue band indicate the median expected excluded cross section with experimental uncertainties. The solid black line with grey band indicates the NLO+NNL SUSY top squark pair-production cross section and theoretical uncertainties.

Chapter 9.

Conclusion

DRAFT

Appendix A.

1 Additional information on triggers

Table A.1.: List of HT triggers used.

H_T bin (GeV)	Trigger
$275 < H_T < 325$	HLT-HT250_v*
$325 < H_T < 375$	HLT-HT300_v*
$375 < H_T < 475$	HLT-HT350_v*
$H_T > 475$	HLT-HT400_v*

Table A.2.: List of α_T triggers used.

$275 < H_T < 325 GeV$	$325 < H_T < 375 GeV$
HLT-HT250_AlphaT0p53_v*	HLT-HT300_AlphaT0p52_v*
HLT-HT250_AlphaT0p55_v*	HLT-HT300_AlphaT0p53_v*
HLT-HT250_AlphaT0p58_v*	HLT-HT300_AlphaT0p54_v*
HLT-HT250_AlphaT0p60_v*	HLT-HT300_AlphaT0p55_v*

$375 < H_T < 475 GeV$	$H_T > 475 GeV$
HLT-HT350_AlphaT0p51_v*	HLT-HT400_AlphaT0p51_v*
HLT-HT350_AlphaT0p52_v*	HLT-HT400_AlphaT0p52_v*
HLT-HT350_AlphaT0p52_v*	
HLT-HT350_AlphaT0p53_v*	

Table A.3.: List of Mu_T triggers used.

$H_T > 275 GeV$	$H_T > 375 GeV$
HLT_Mu5_HT200_v*	HLT_Mu5_HT200_v*
HLT_Mu8_HT200_v*	HLT_Mu8_HT200_v*
HLT_Mu15_HT200_v*	HLT_Mu15_HT200_v*
HLT_Mu30_HT200_v*	HLT_Mu30_HT200_v*
HLT_Mu40_HT200_v*	HLT_Mu40_HT200_v*
	HLT_Mu40_HT300_v*

Table A.4.: List of Photon triggers used.

$H_T > 375 GeV$
HLT_Photon75_CaloIdVL_v*
HLT_Photon75_CaloIdVL_IsoL_v*
HLT_Photon90_CaloIdVL_v*
HLT_Photon90_CaloIdVL_IsoL_v*
HLT_Photon125_v*
HLT_Photon135_v*

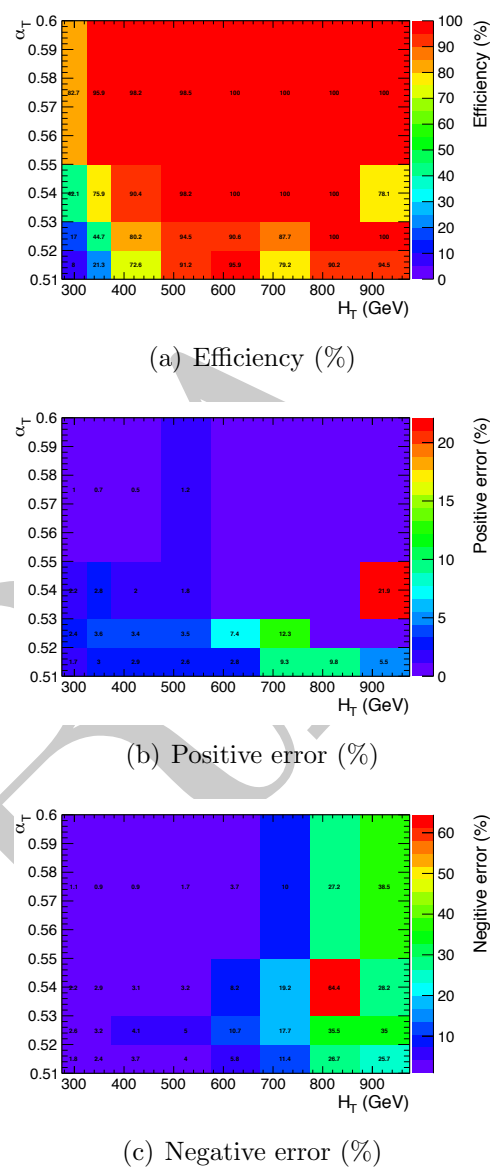


Figure A.1.: Efficiency and associated errors of the α_T trigger in offline bins of H_T and α_T .

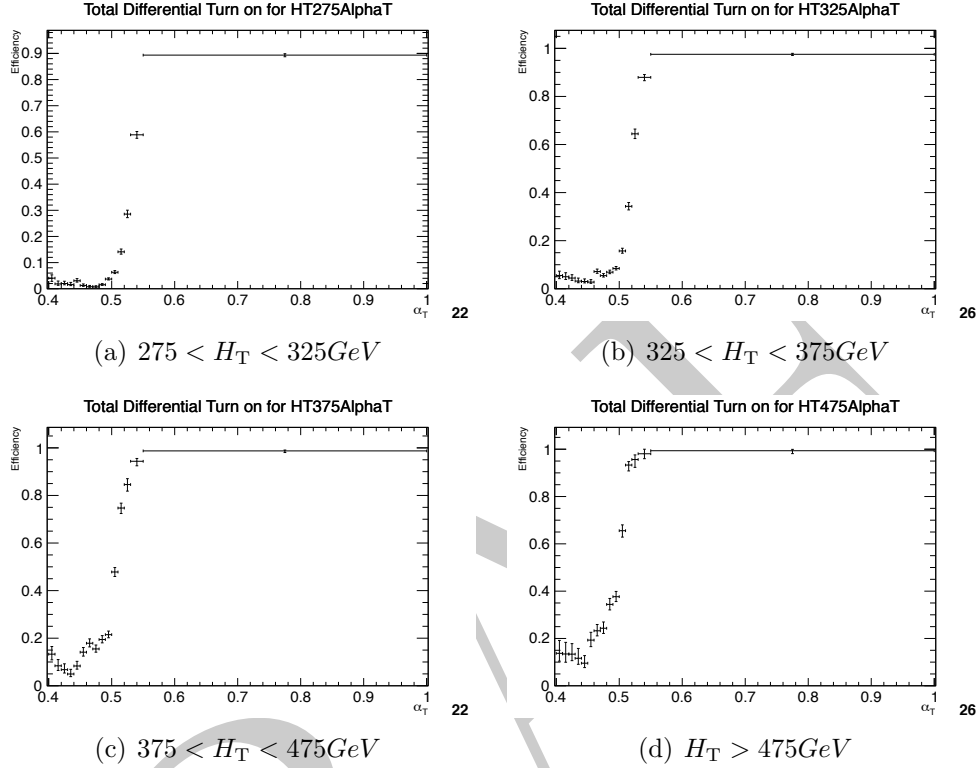


Figure A.2.: Efficiency turn-on curves for the α_T triggers used to collect events for four different HT regions.

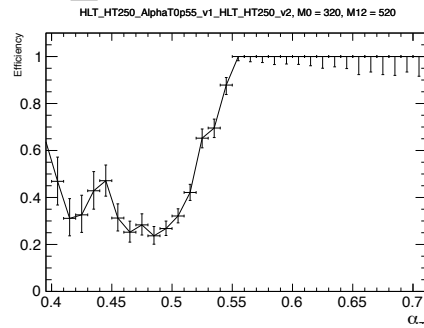


Figure A.3.: Efficiency turn-on curve for the representative model RM1, with $m_0 = 320 \text{ GeV}$ and $m_{1/2} = 520 \text{ GeV}$, using the α_T trigger with thresholds $H_T > 250 \text{ GeV}$ and $\alpha_T > 0.55$ and an offline signal region defined by $H_T > 275 \text{ GeV}$ and $\alpha_T > 0.55$.

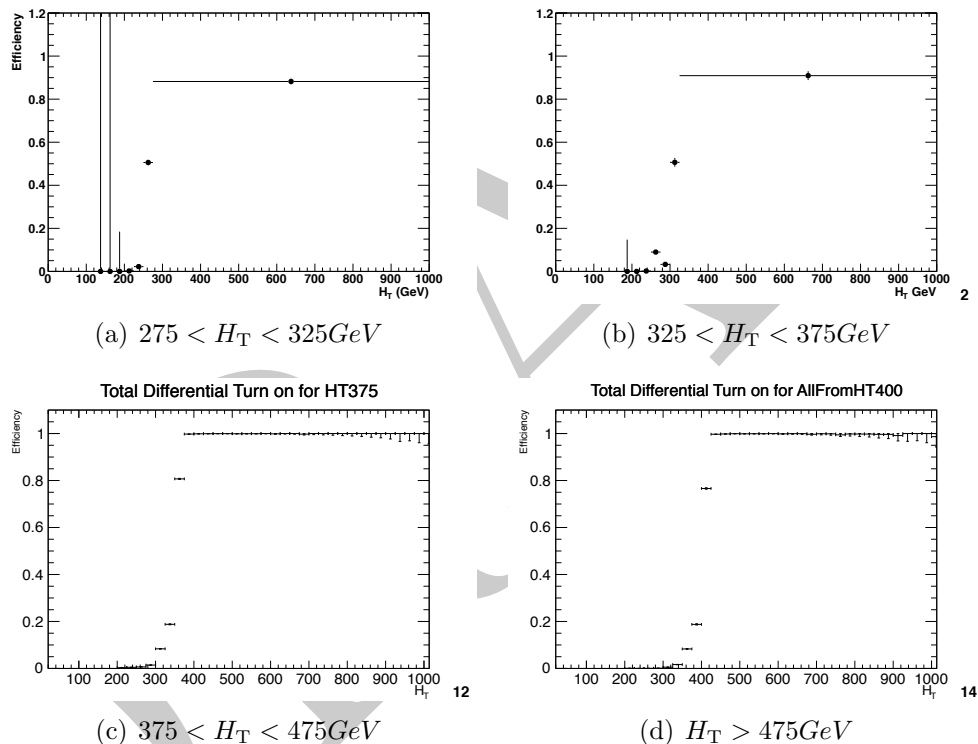


Figure A.4.: Efficiency turn-on curves for the H_T triggers used to collect events for four different H_T regions.

Appendix B.

¹ Addition information on background ² estimation methods

³ B.1. Determination of k_{QCD}

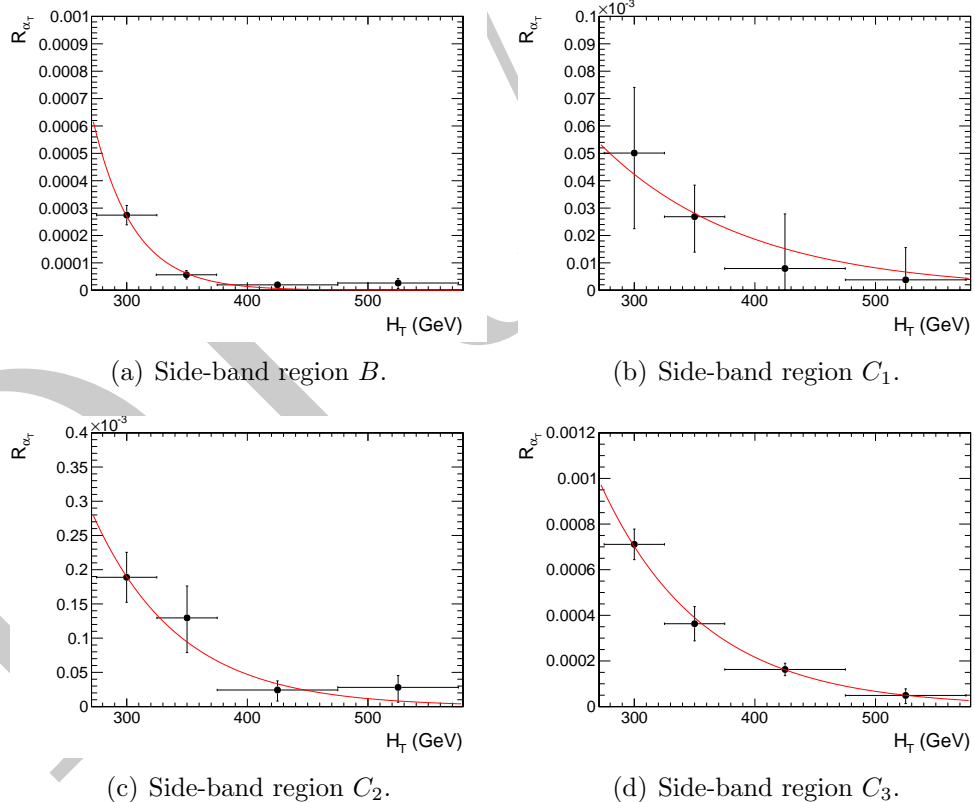


Figure B.1.: $R_{\alpha_T}(H_T)$ and exponential fit for various data side-bands. Linear y-axis scale.

Appendix C.

¹ Closure tests and systematic ² uncertainties

³ C.1. Defining muon samples without an α_T ⁴ requirement

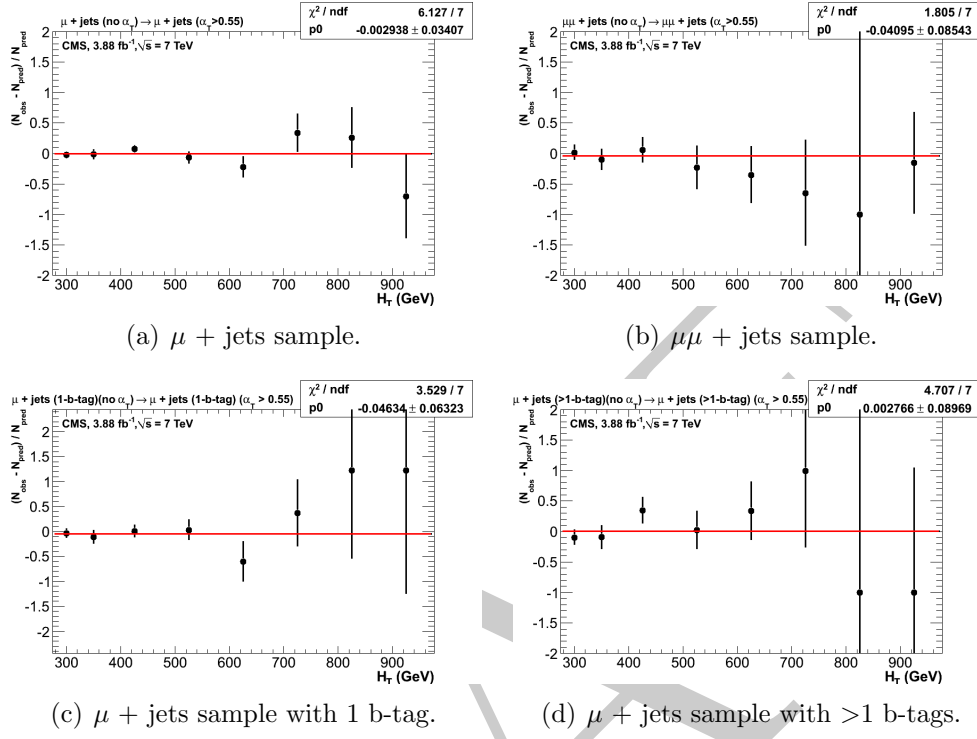


Figure C.1.: Closure tests that demonstrate the MC modelling of the α_T acceptance. The closure tests are performed for both the inclusive analysis with (a) the $\mu + \text{jets}$ sample and (b) the $\mu\mu + \text{jets}$ control sample. Similar tests are performed for the b-tag analysis using (a) the $\mu + \text{jets}$ sample and a requirement of exactly one b-tag, and (b) the $\mu + \text{jets}$ sample and a requirement of at least two b-tags. The red lines indicate the constant best fit value across all H_T bins.

C.2. Closure tests for inclusive analysis

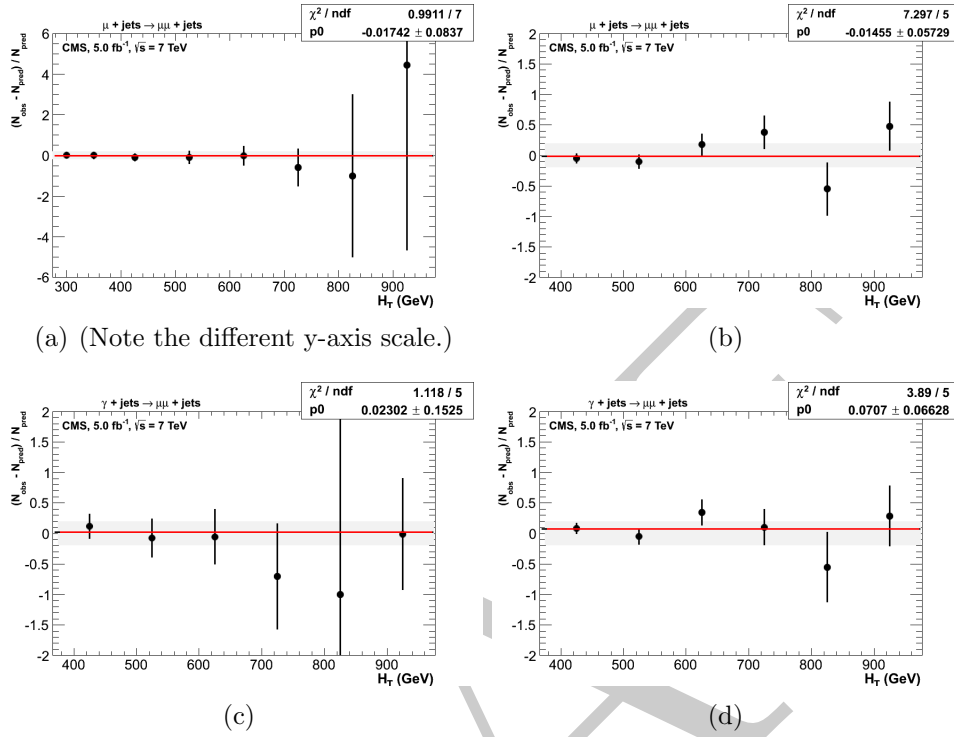


Figure C.2.: Closure tests using yields from one control to predict yields in another sample. The two plots on the left show closure tests which use “low stats” muon samples recorded with the `HT_AlphaT` triggers and defined by offline selection criteria that include an α_T requirement: (a) $\mu + \text{jets}$ sample $\rightarrow \mu\mu + \text{jets}$ sample and (c) $\gamma + \text{jets}$ sample $\rightarrow \mu\mu + \text{jets}$ sample. Similarly, the plots on the right show the same closure tests but using “high-stats” muon samples recorded with `Mu_HT` triggers and defined with no offline α_T requirement. The same tests are performed: (b) $\mu + \text{jets}$ sample $\rightarrow \mu\mu + \text{jets}$ sample and (d) $\gamma + \text{jets}$ sample $\rightarrow \mu\mu + \text{jets}$ sample. These closure tests are only possible for the six highest H_T bins due to the trigger conditions. The red lines indicate the constant best fit value across all H_T bins.

1 C.3. Closure tests for b-tag analysis

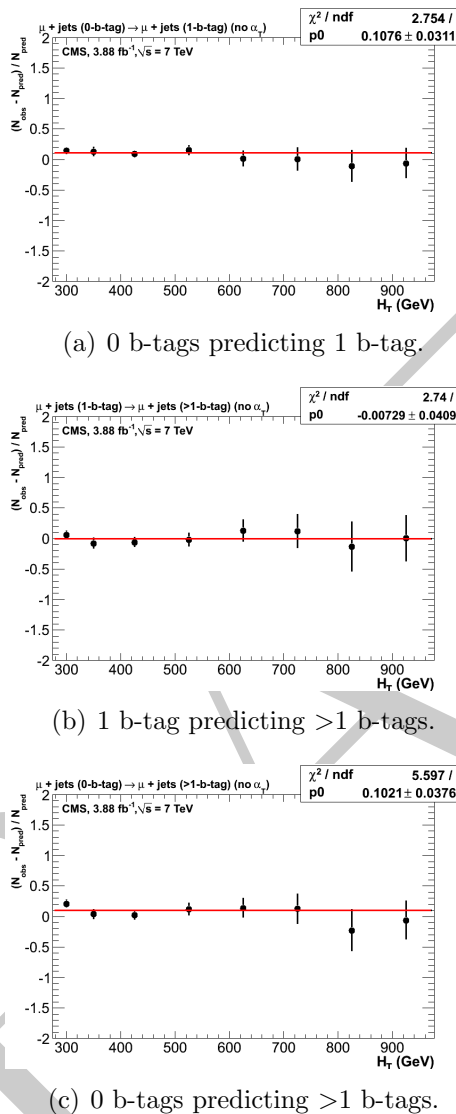


Figure C.3.: Closure tests with the $\mu + \text{jets}$ sample that demonstrate the MC modelling of the b-tagging algorithm and of different sample compositions by for different b-tag multiplicities: (a) 0 b-tags \rightarrow 1 b-tag, (b) 1 b-tags $\rightarrow \geq 2$ b-tags, (c) 0 b-tags $\rightarrow \geq 2$ b-tags.

C.4. Closure tests concerning pile-up

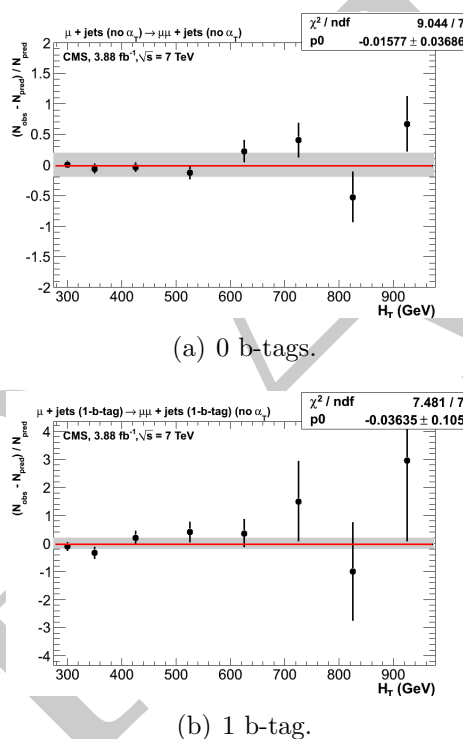


Figure C.4.: Closure tests using the $\mu + \text{jets}$ sample to predict the yields in a $\mu\mu + \text{jets}$ sample, for events with (a) exactly 0-b-tags and (b) exactly 1-b-tags.

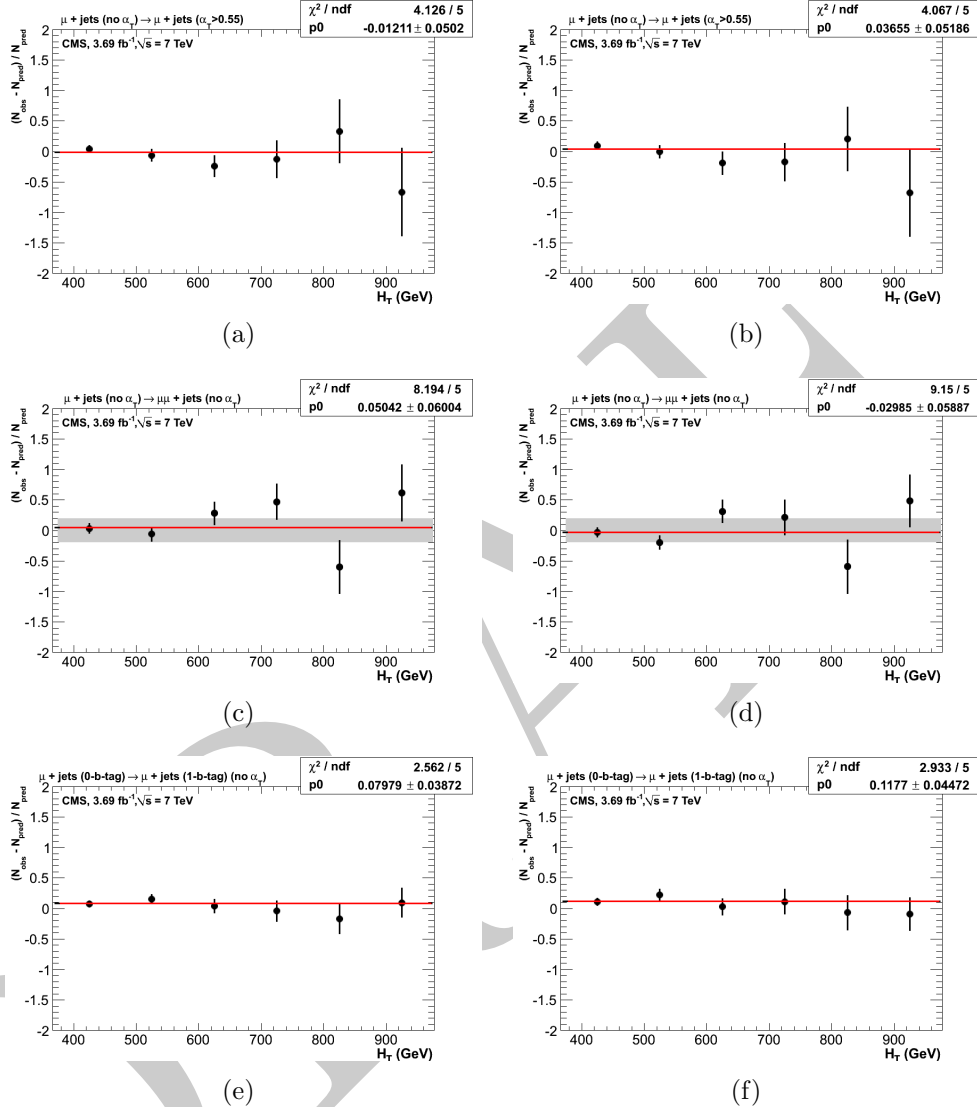


Figure C.5.: Closure tests using yields from one control to predict yields in another sample. The three plots on the left show closure tests from the inclusive analysis, which uses jets that are not corrected for the effects of pile-up. On the right, the jets in the analysis *are* corrected for pile-up effects by applying the L10offset jet energy correction. The three closure tests are: probing the MC modelling of the α_T acceptance with the $\mu + \text{jets}$ sample (a) without and (b) with L10offset jet energy corrections; using the $\mu + \text{jets}$ sample to predict yields in the $\mu\mu + \text{jets}$ sample (a) without and (b) with L10offset jet energy corrections; and using a 0 b-tagged $\mu + \text{jets}$ sample to predict yields in a 1 b-tagged $\mu + \text{jets}$ sample (a) without and (b) with L10offset jet energy corrections. The red lines indicate the constant best fit value across all H_T bins.

Appendix D.

1 Signal efficiency

2 D.1. CMSSM

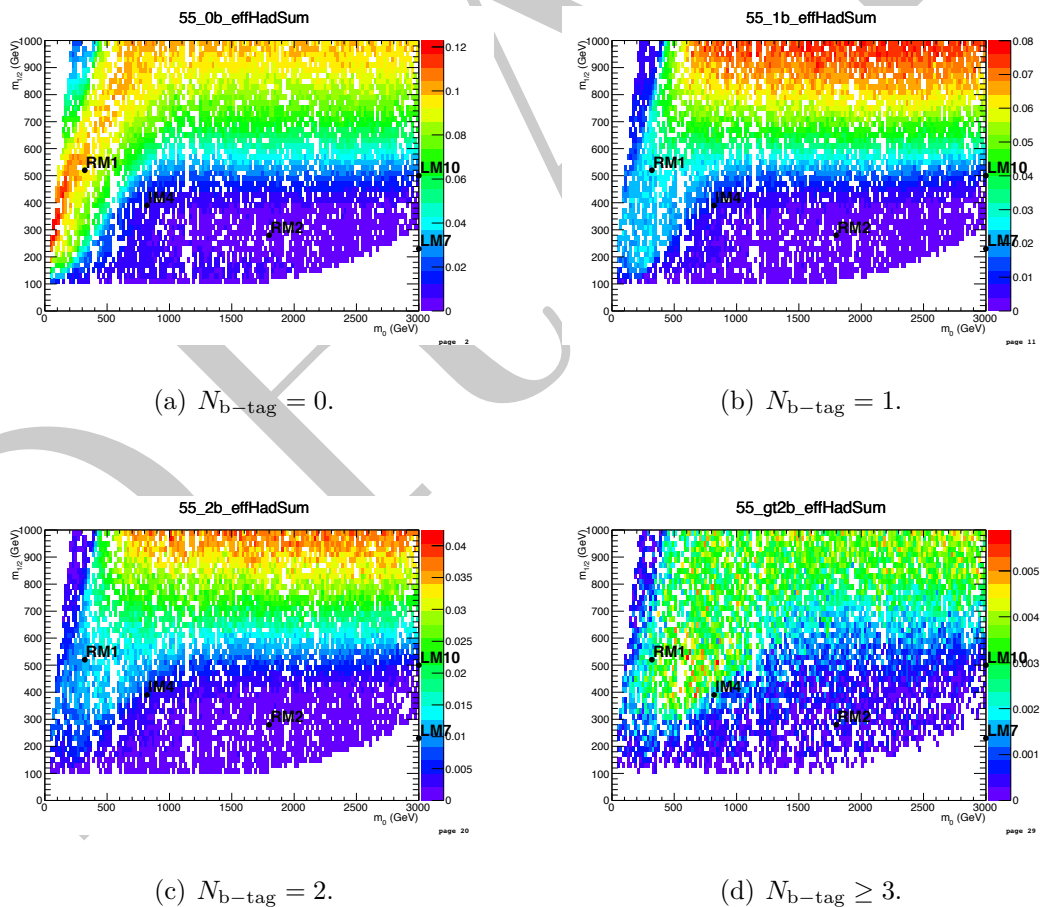


Figure D.1.: Signal efficiency in the $(m_0, m_{1/2})$ plane of the CMSSM, of the full hadronic signal selection, integrating over all eight H_T bins and requiring (a) exactly zero, (b) exactly one, (c) exactly two, and (d) at least three b-tags per event.

1 D.2. T1

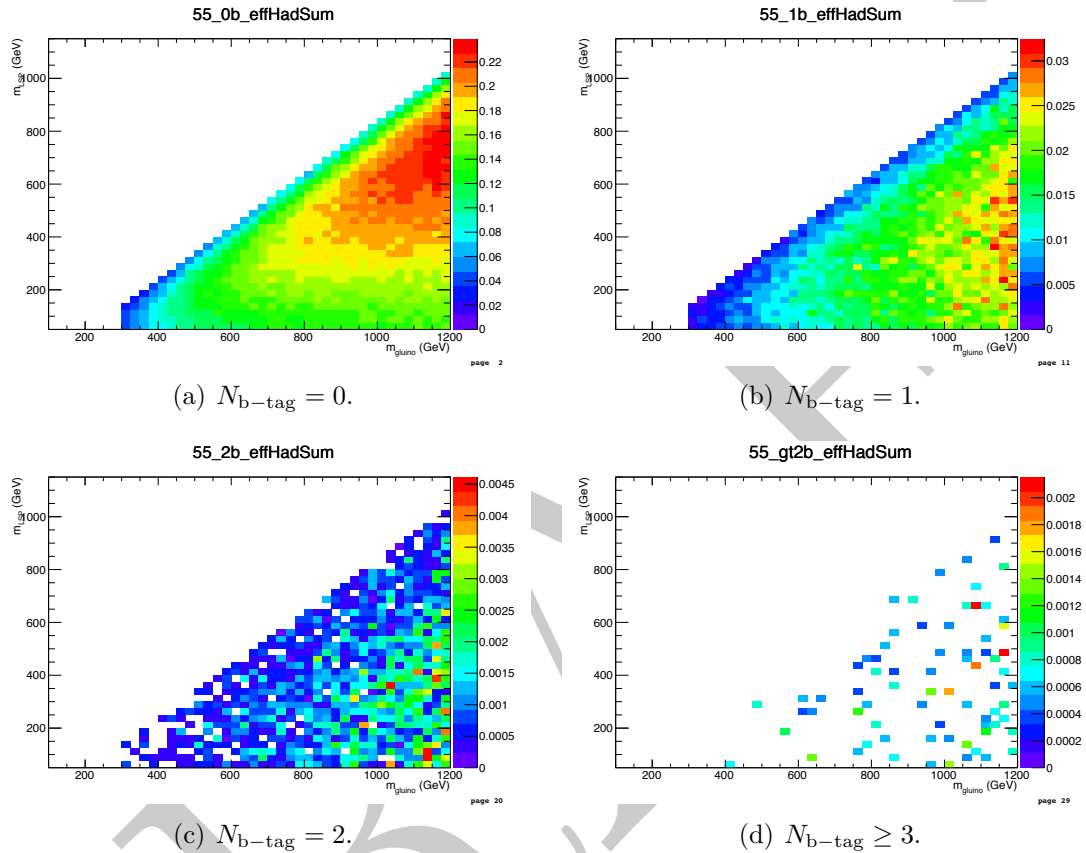


Figure D.2.: Signal efficiency in the $(m_{\text{glino}}, m_{\text{LSP}})$ plane of the T1 simplified model, of the full hadronic signal selection, integrating over all eight H_T bins and requiring (a) exactly zero, (b) exactly one, (c) exactly two, and (d) at least three b-tags per event.

¹ D.3. T2

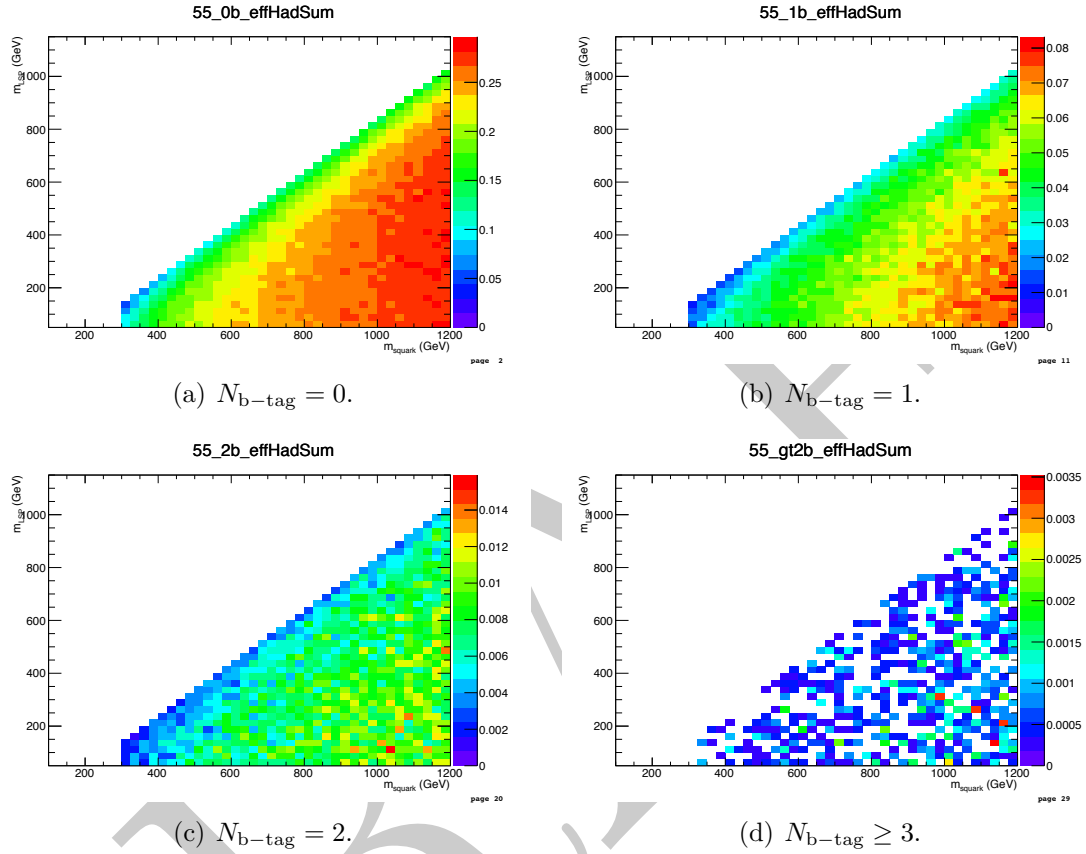


Figure D.3.: Signal efficiency in the $(m_{\text{sq}}, m_{\text{LSP}})$ plane of the T2 simplified model, of the full hadronic signal selection, integrating over all eight H_T bins and requiring (a) exactly zero, (b) exactly one, (c) exactly two, and (d) at least three b-tags per event.

1 D.4. T2tt

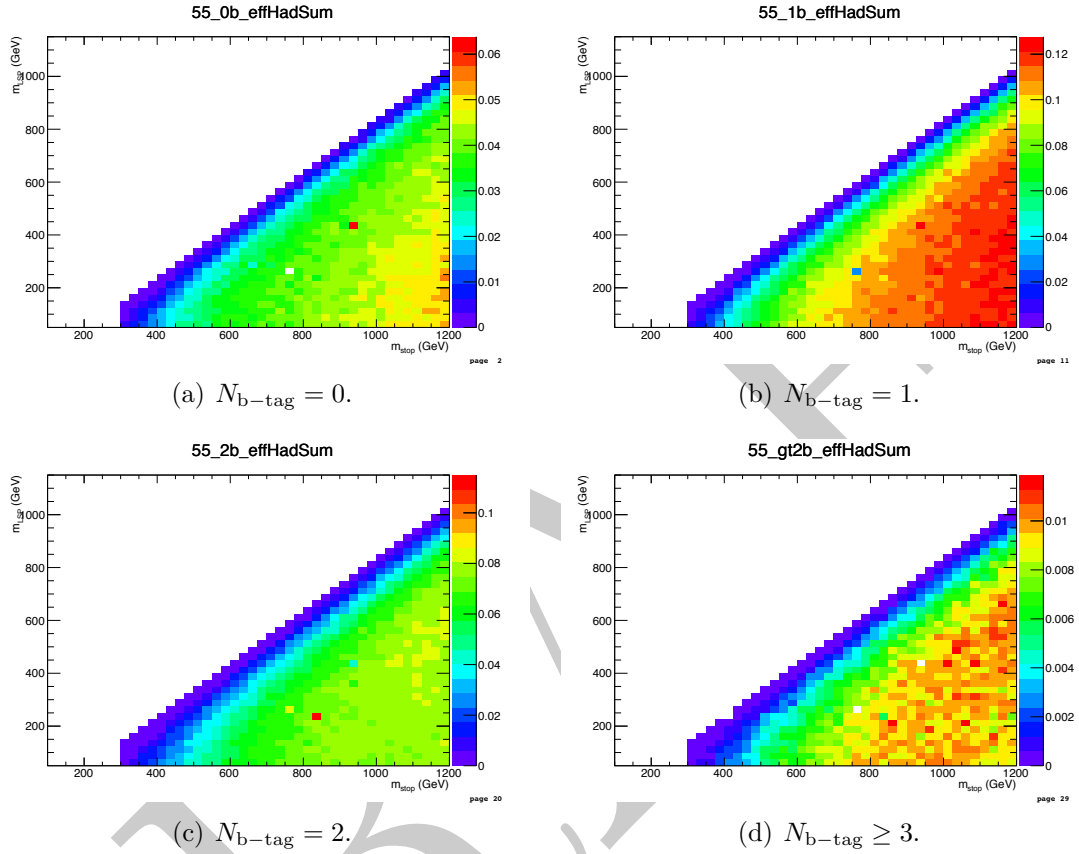


Figure D.4.: Signal efficiency in the $(m_{\text{sq}}, m_{\text{LSP}})$ plane of the T2tt simplified model, of the full hadronic signal selection, integrating over all eight H_T bins and requiring (a) exactly zero, (b) exactly one, (c) exactly two, and (d) at least three b-tags per event.

1 D.5. T2bb

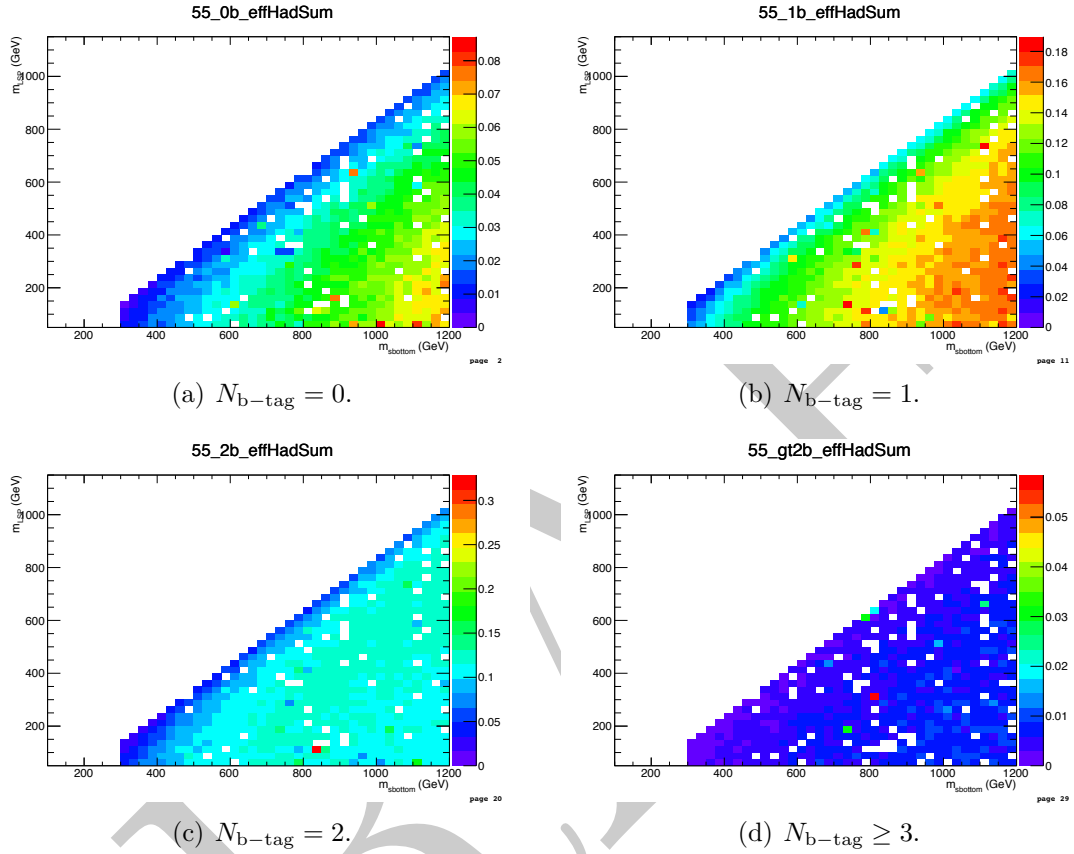


Figure D.5.: Signal efficiency in the (m_{sq}, m_{LSP}) plane of the T2bb simplified model, of the full hadronic signal selection, integrating over all eight H_T bins and requiring (a) exactly zero, (b) exactly one, (c) exactly two, and (d) at least three b-tags per event.

1 D.6. T1tttt

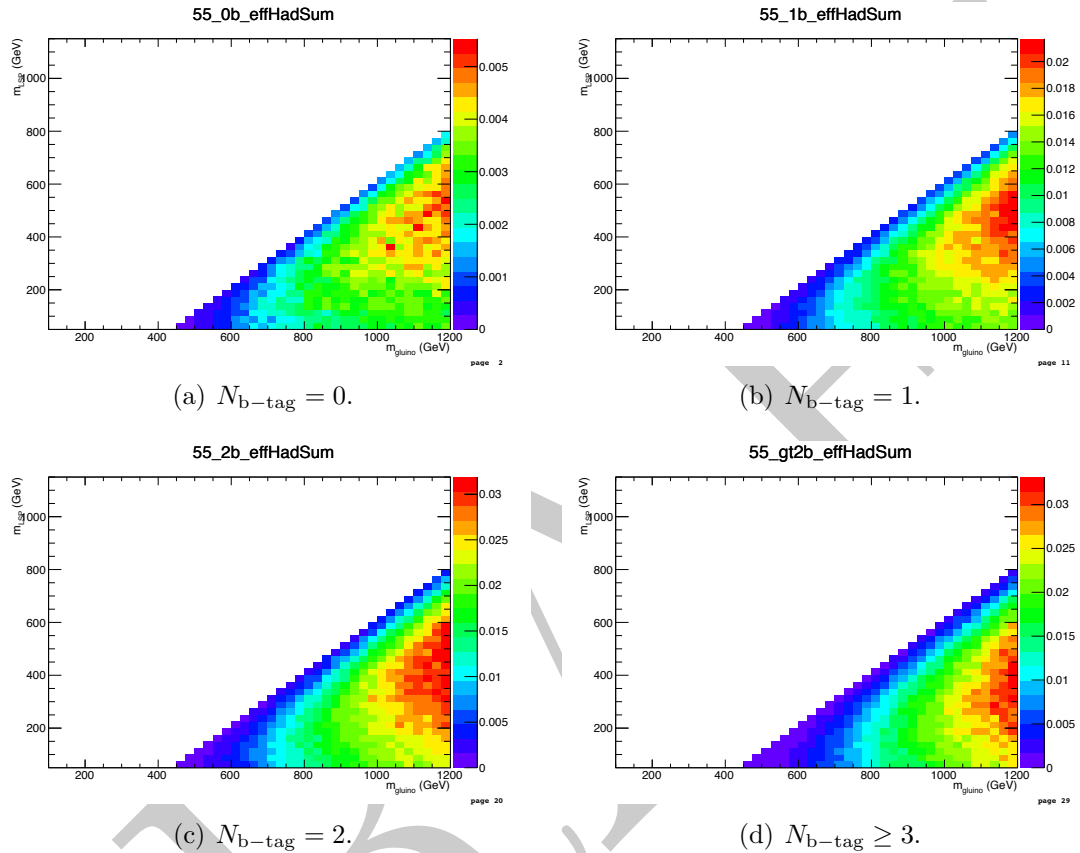


Figure D.6.: Signal efficiency in the $(m_{\text{gluino}}, m_{\text{LSP}})$ plane of the T1tttt simplified model, of the full hadronic signal selection, integrating over all eight H_T bins and requiring (a) exactly zero, (b) exactly one, (c) exactly two, and (d) at least three b-tags per event.

1 D.7. T1bbbb

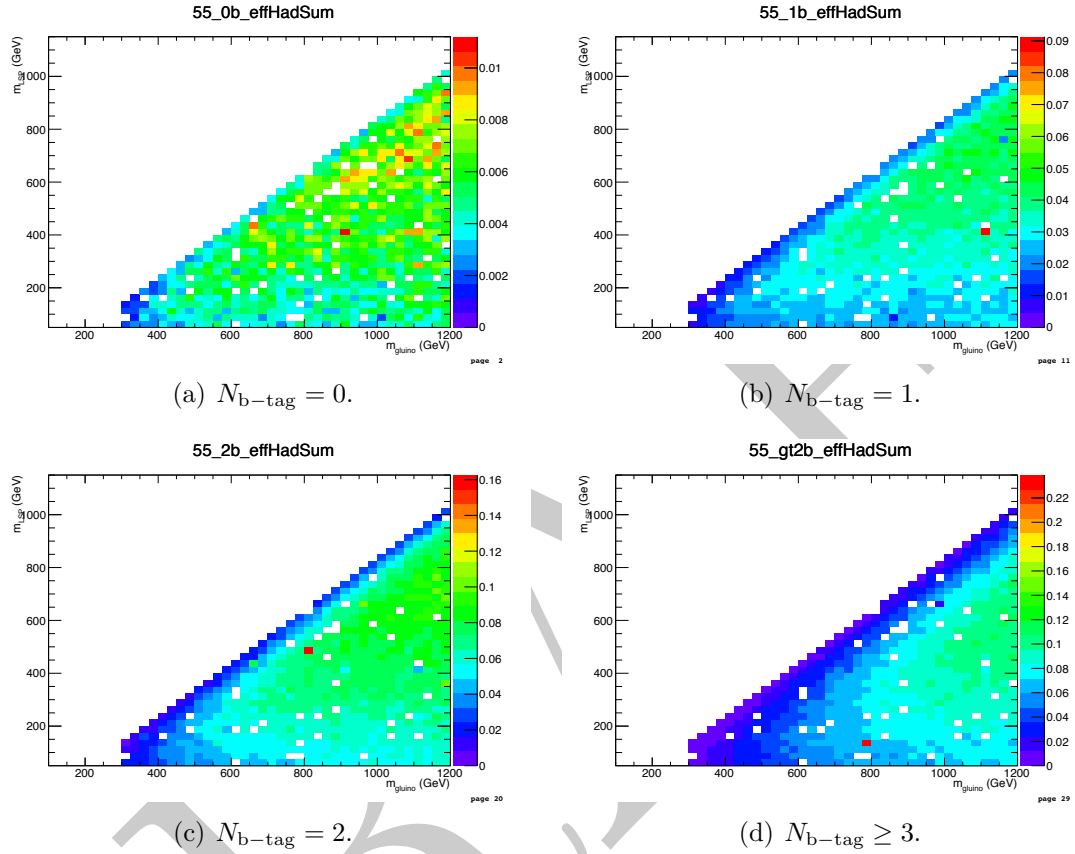


Figure D.7.: Signal efficiency in the $(m_{\text{gluino}}, m_{\text{LSP}})$ plane of the T1bbbb simplified model, of the full hadronic signal selection, integrating over all eight H_T bins and requiring (a) exactly zero, (b) exactly one, (c) exactly two, and (d) at least three b-tags per event.

1 D.8. Signal contamination for T1tttt

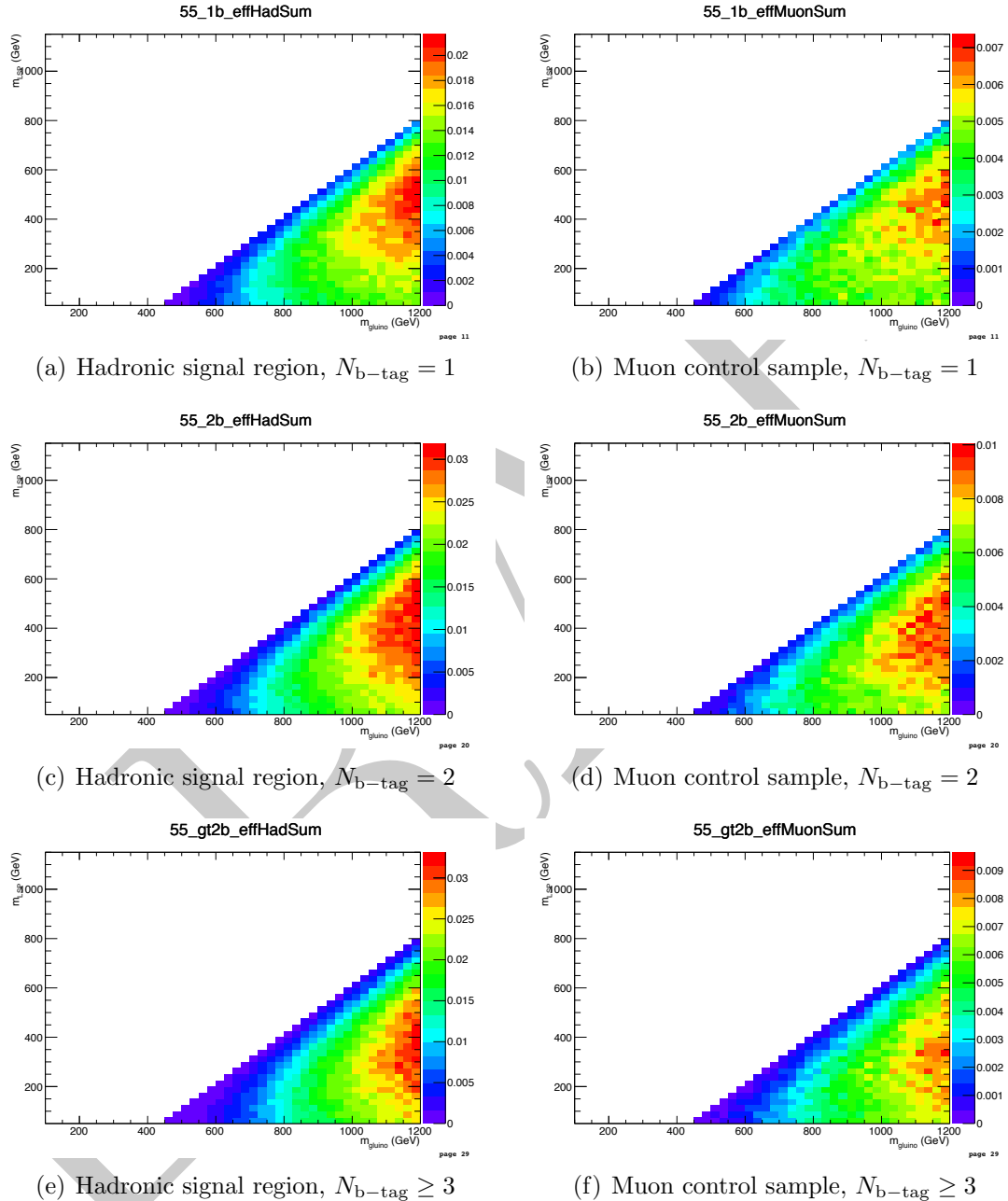


Figure D.8.: Signal efficiency in the planes of simplified model T1tttt, of the (left) hadronic signal sample selection or (right) single muon control sample selection, integrating over all eight H_T bins and requiring (top) exactly one, (middle) exactly two, or (bottom) at least three b-tags per event.

Appendix E.

¹ Experimental systematic
² uncertainties on signal efficiency
³ times acceptance

⁴ E.1. Systematics due to jet energy scale
⁵ uncertainties

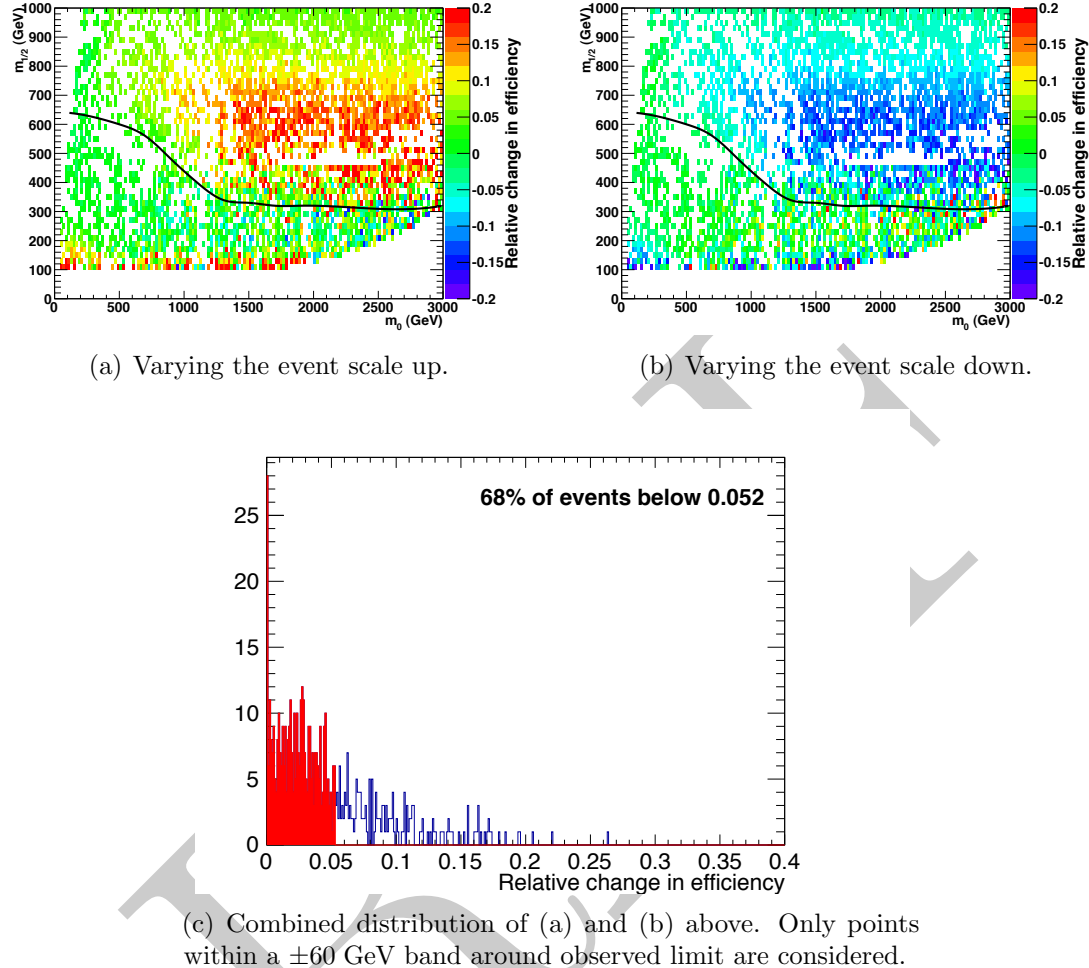


Figure E.1.: The effect of jet energy scale variations on signal efficiency in the CMSSM plane. All plots show the relative change in efficiency. No requirement is made on the number of reconstructed b jets. The red shaded area is bounded by the 68th percentile.

E.2. Systematics due to the MHT/MET cut

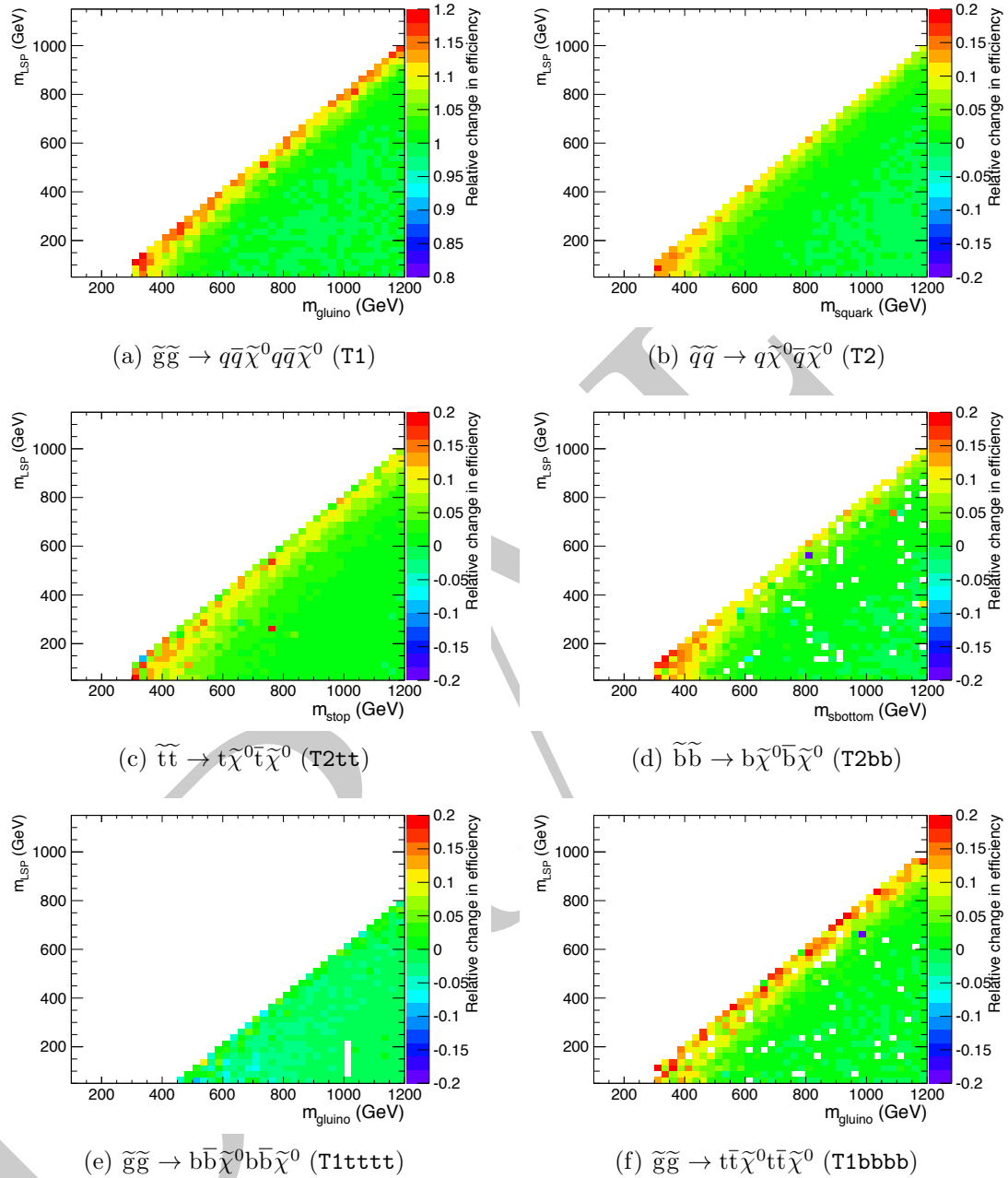


Figure E.2.: The fractional change in signal efficiency due to systematically increasing all jet energies, for various topologies. No requirement is made on the number of reconstructed b jets.

E.3. Systematics due to the dead ECAL cut

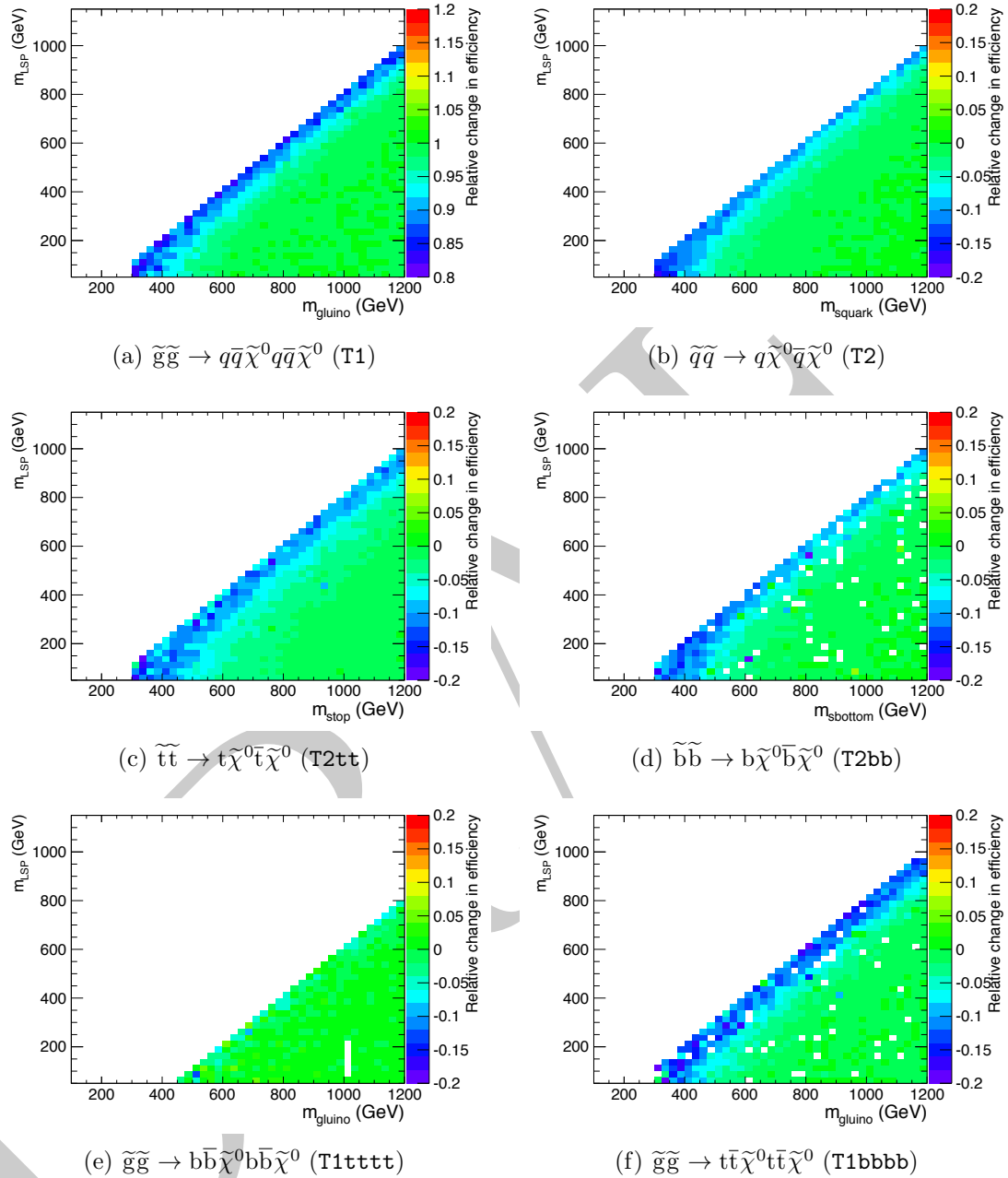


Figure E.3.: The fractional change in signal efficiency due to systematically decreasing all jet energies, for various topologies. No requirement is made on the number of reconstructed b jets.

E.4. Systematics due to the lepton and photon vetoes

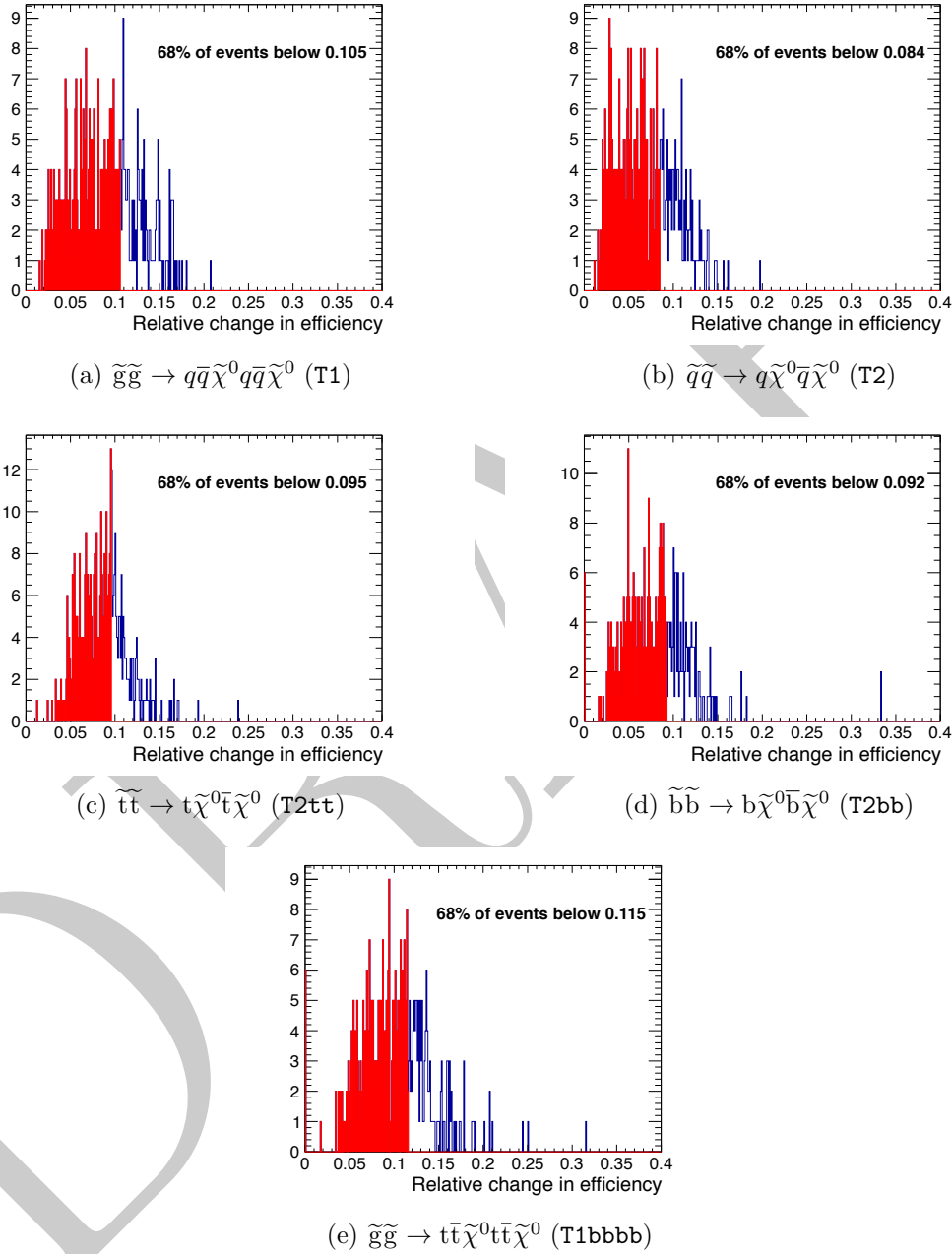


Figure E.4.: The fractional change in signal efficiency near to the diagonal due to systematically increasing or decreasing all jet energies, for various topologies. No requirement is made on the number of reconstructed b jets.

Experimental systematic uncertainties on signal efficiency times acceptance

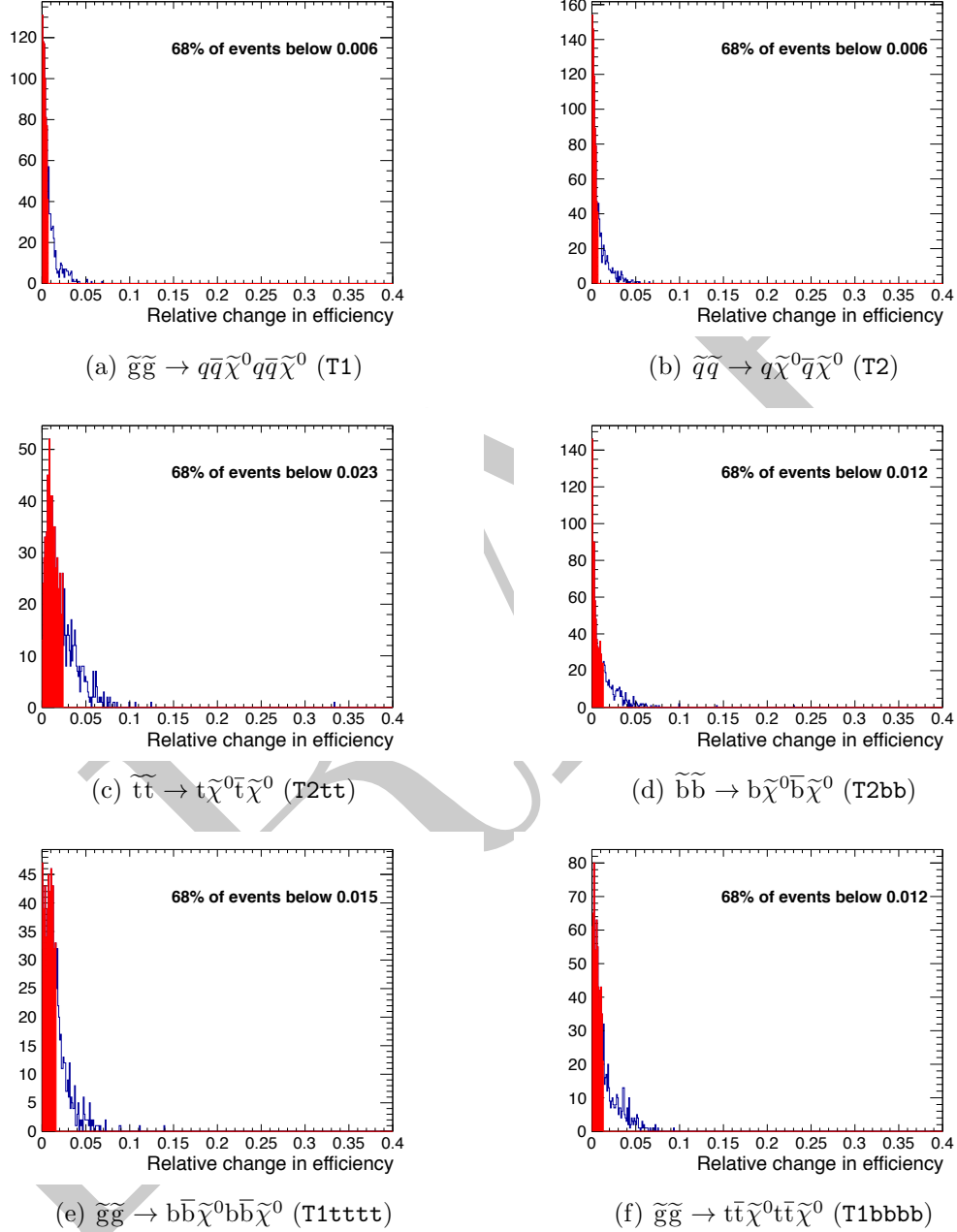


Figure E.5.: The fractional change in signal efficiency far from the diagonal due to systematically increasing or decreasing all jet energies, for various topologies. No requirement is made on the number of reconstructed b jets.

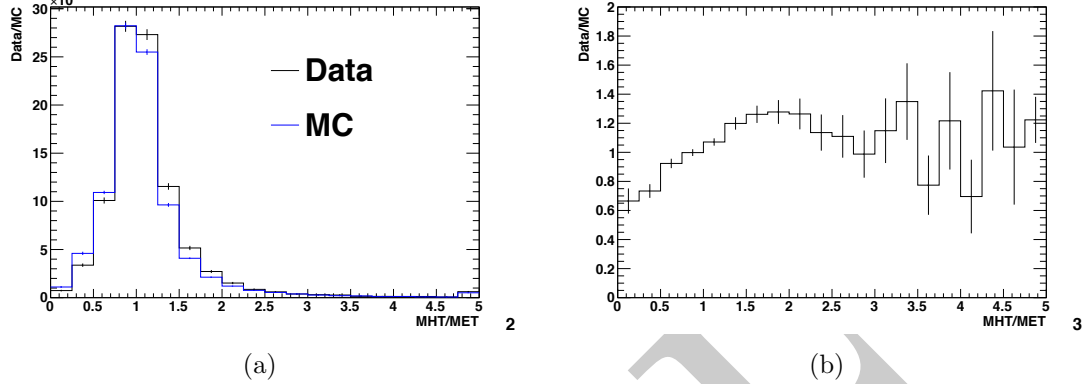
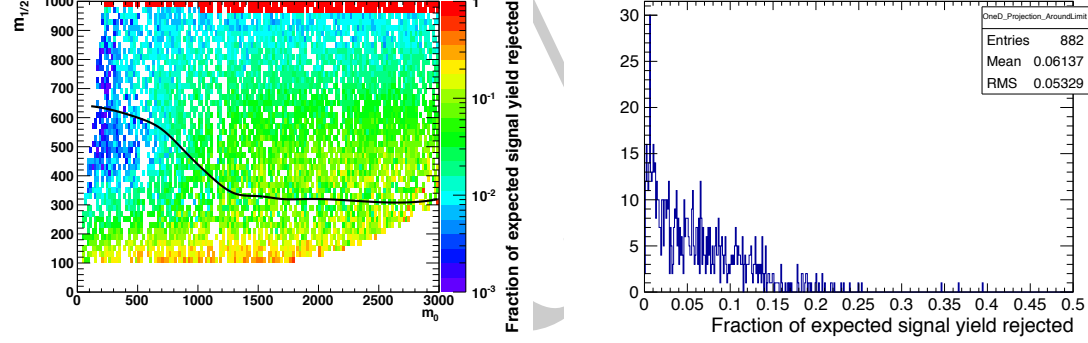


Figure E.6.: (a) Comparison of the MHT/MET distributions from data and MC, and (b) the ratio of the distributions, data/MC, as a function of the MHT/MET cut value.



(a) Fraction of expected signal yield rejected. (b) Fraction of expected signal yield rejected in a ± 60 GeV band around the observed limit.

Figure E.7.: The fraction of expected signal yield that is rejected by the MHT/MET cut in the CMSSM plane. No requirement is made on the number of reconstructed b jets.

Table E.1.: Conservative estimates of inefficiency (%) for the MHT/MET cut when considering model points in the region near to the diagonal (i.e. small mass splitting and compressed spectra) for various simplified models.

	T1	T2	T2tt	T2bb	T1tttt	T1bbbb
Near	10.9	3.5	20.4	3.9	-	10.8
Far	3.2	0.9	3.1	1.2	32.4	3.7

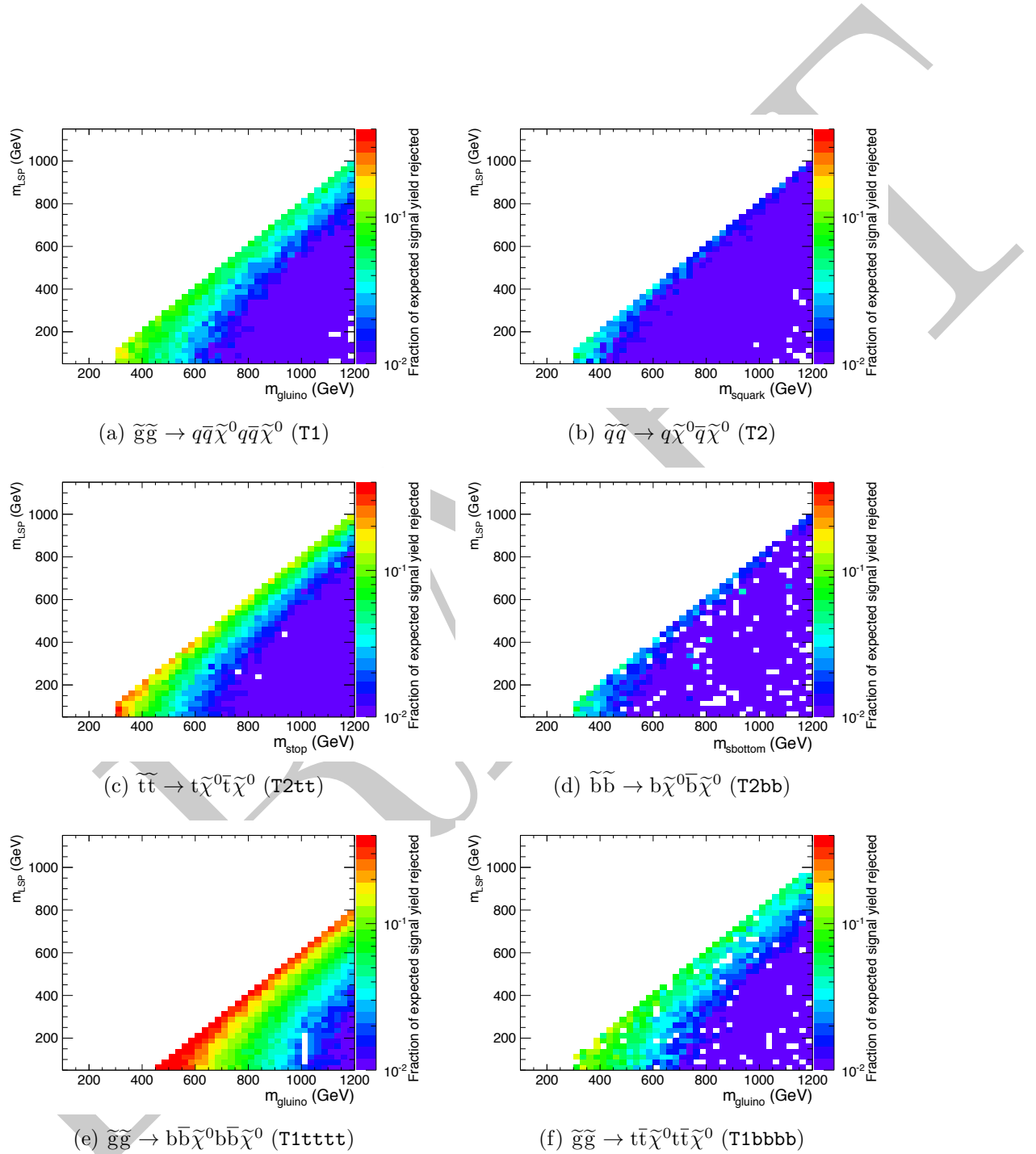


Figure E.8.: The fraction of expected signal yield that is rejected by the MHT/MET cleaning cut, for various topologies. No requirement is made on the number of reconstructed b jets.

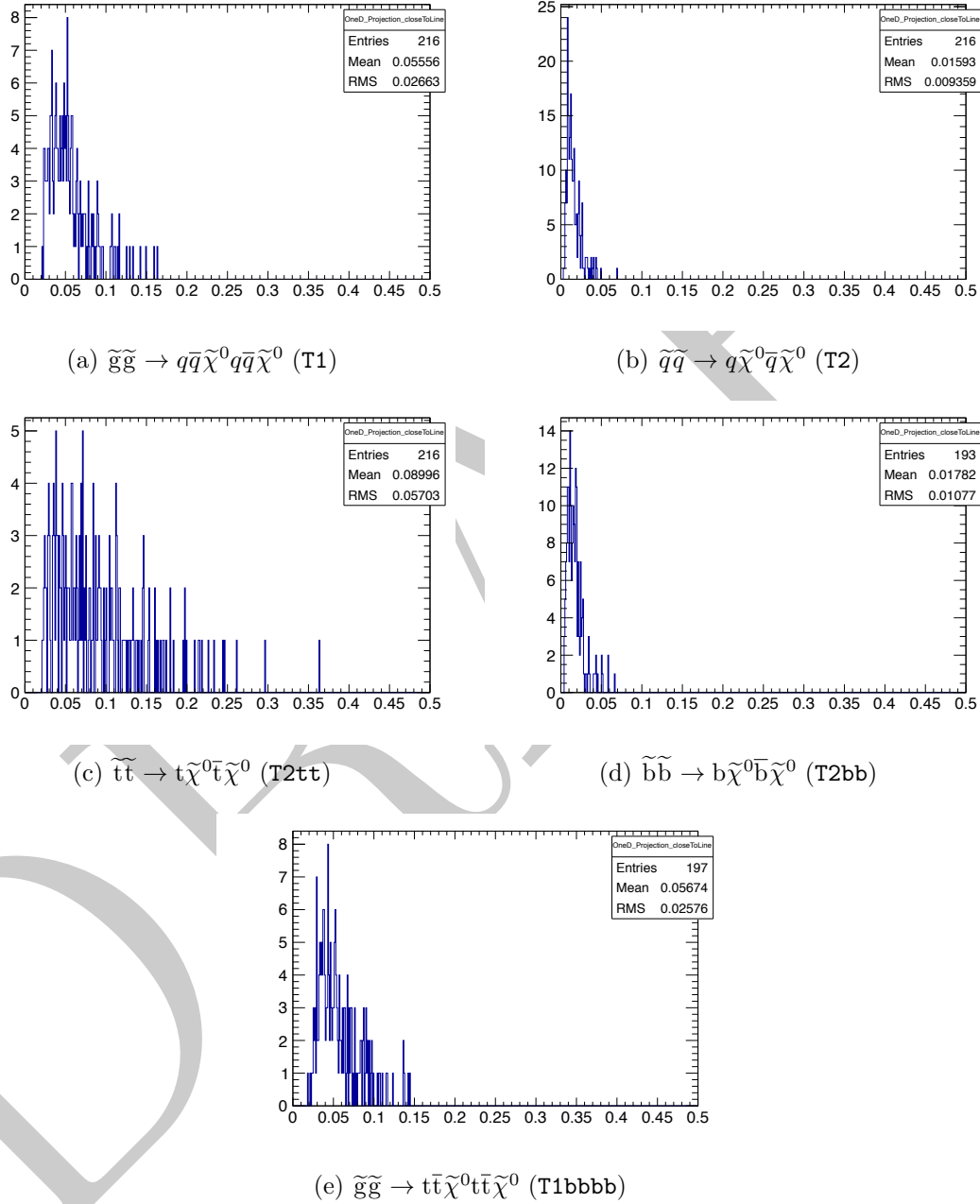


Figure E.9.: The fraction of expected signal yield that is rejected by the MHT/MET cleaning cut, near to the diagonal, for various topologies. No requirement is made on the number of reconstructed b jets.

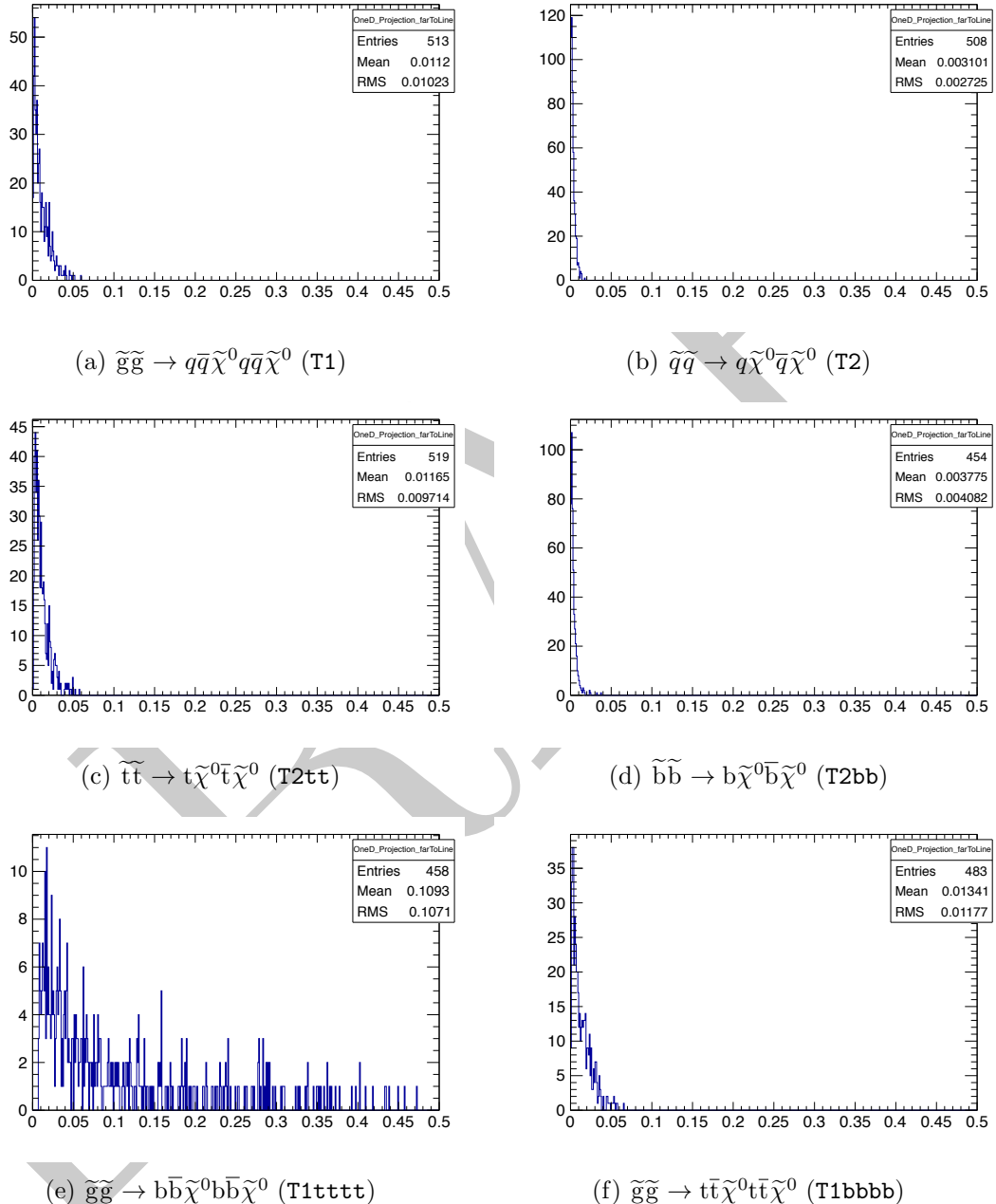


Figure E.10.: The fraction of expected signal yield that is rejected by the MHT/MET cleaning cut, far from the diagonal, for various topologies. No requirement is made on the number of reconstructed b jets.

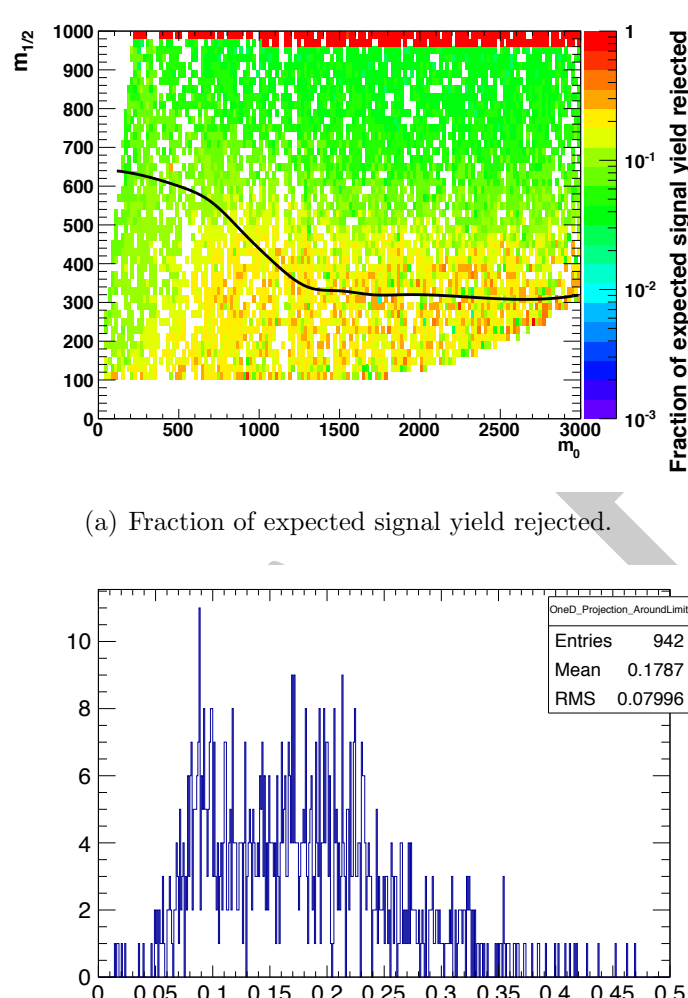


Figure E.11.: The fraction of expected signal yield that is rejected by the dead ECAL cut in the CMSSM plane. No requirement is made on the number of reconstructed b jets.

Table E.2.: Conservative estimates of inefficiency (%) for the dead ECAL cut when considering model points in the region near to the diagonal (i.e. small mass splitting and compressed spectra) for various simplified models.

	T1	T2	T2tt	T2bb	T1tttt	T1bbbb
Near	13.3	6.4	23.7	7.5	-	16.4
Far	13.6	5.8	9.4	6.2	27.6	13.9

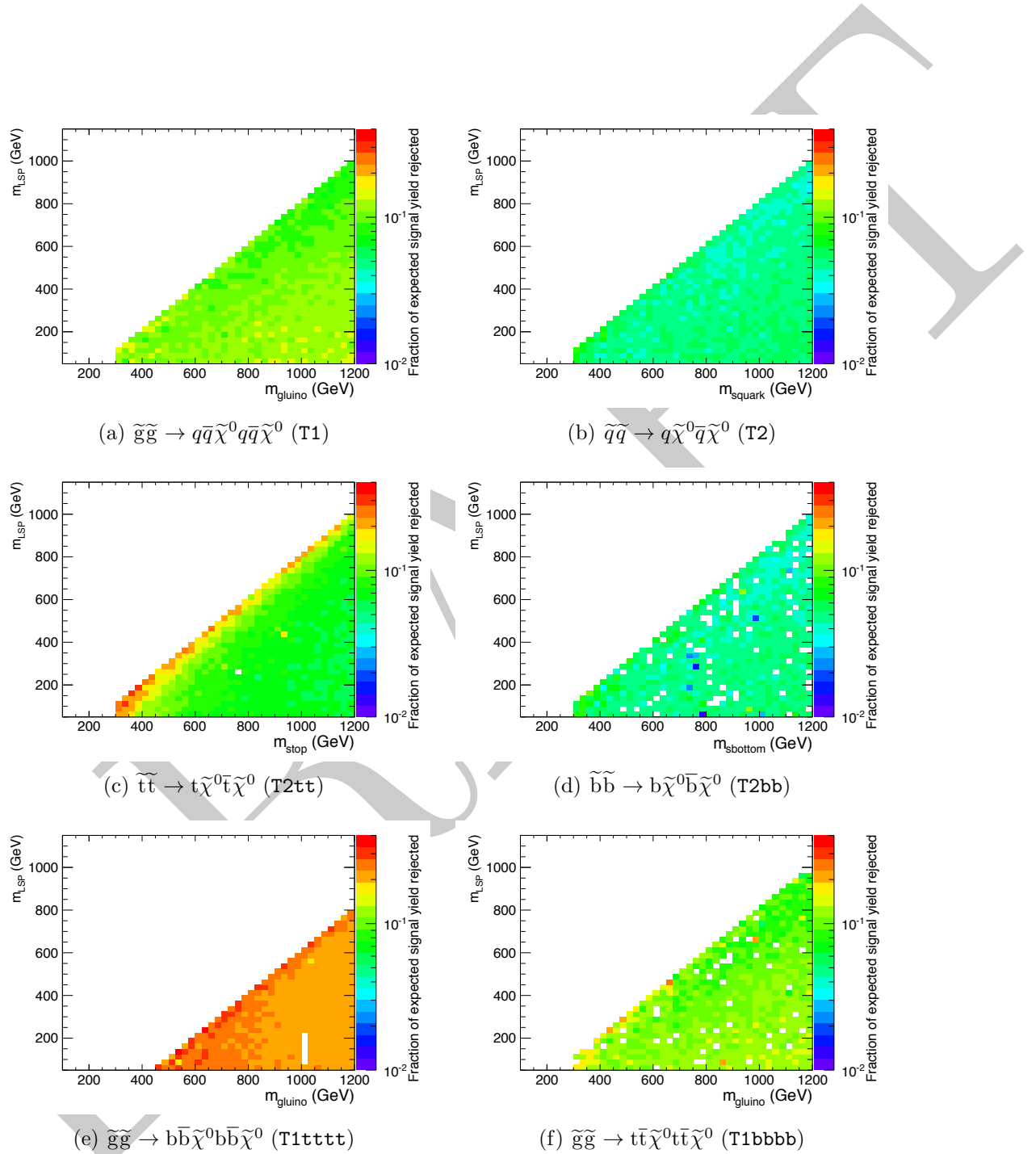


Figure E.12.: The fraction of expected signal yield that is rejected by the dead ECAL cleaning cut, for various topologies. No requirement is made on the number of reconstructed b jets.

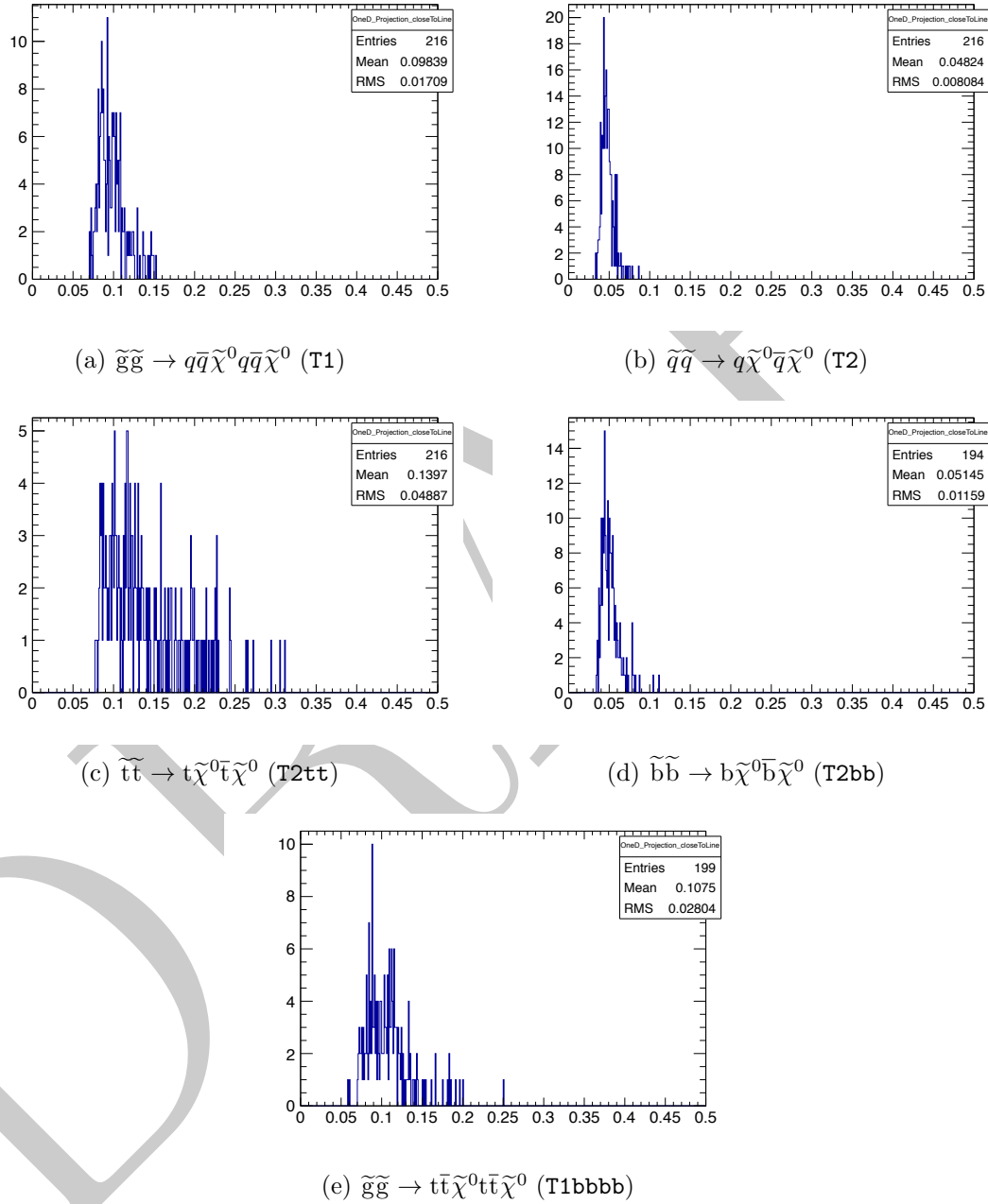


Figure E.13.: The fraction of expected signal yield that is rejected by the dead ECAL cleaning cut, near to the diagonal, for various topologies. No requirement is made on the number of reconstructed b jets.

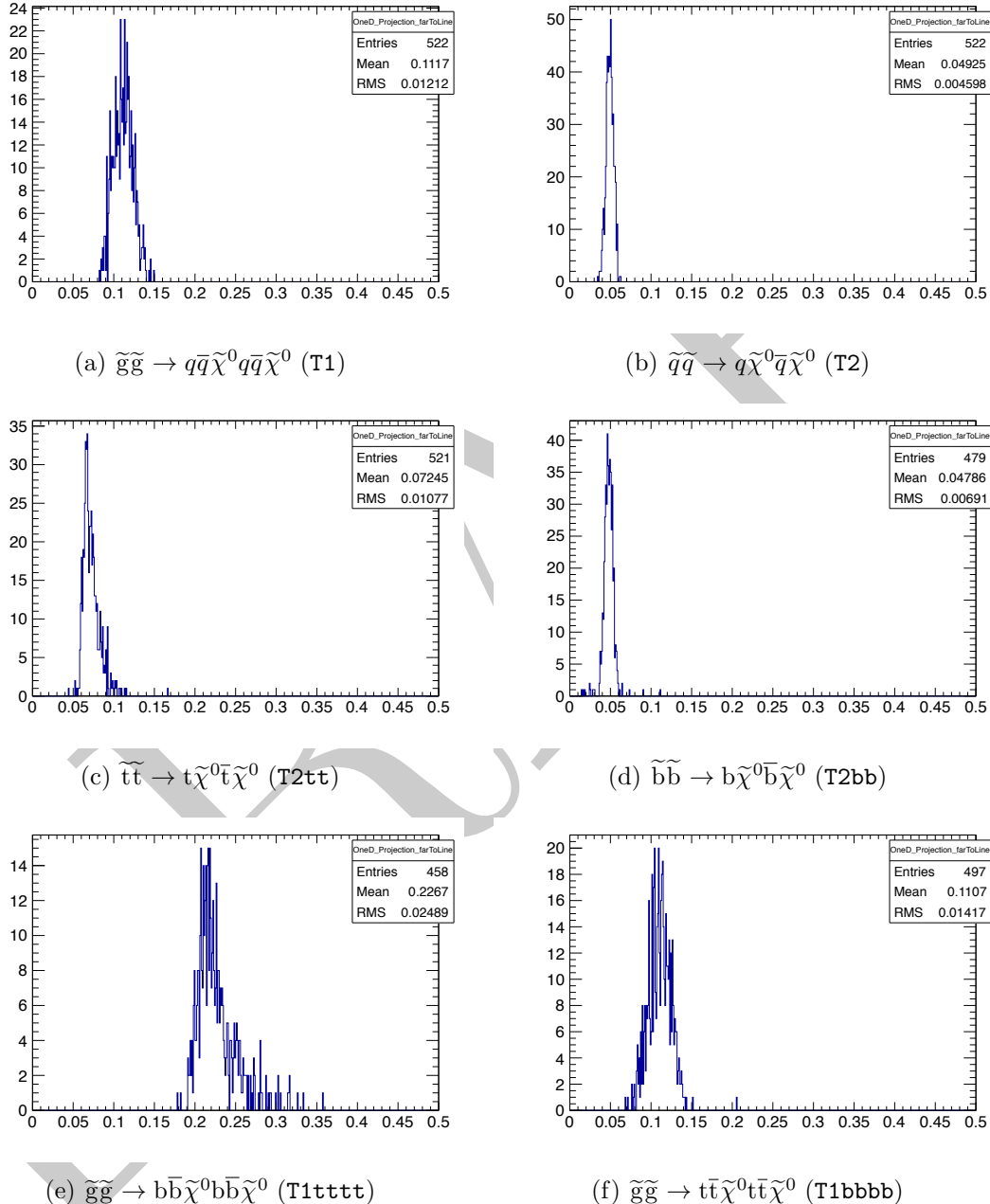
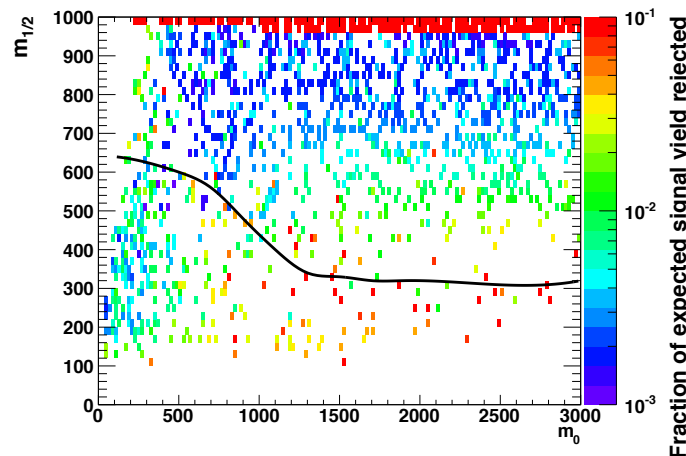
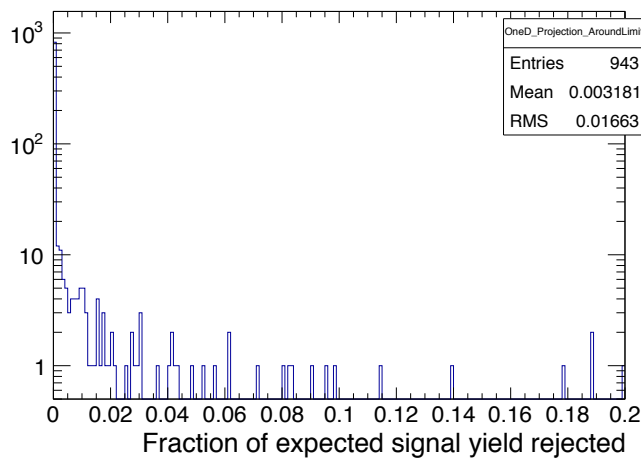


Figure E.14.: The fraction of expected signal yield that is rejected by the dead ECAL cleaning cut, far from the diagonal, for various topologies. No requirement is made on the number of reconstructed b jets.



(a) Fraction of expected signal yield rejected.



(b) Fraction of expected signal yield rejected in a ± 60 GeV band around the observed limit.

Figure E.15.: The fraction of expected signal yield that is rejected by the dead ECAL cut in the CMSSM plane. No requirement is made on the number of reconstructed b jets.

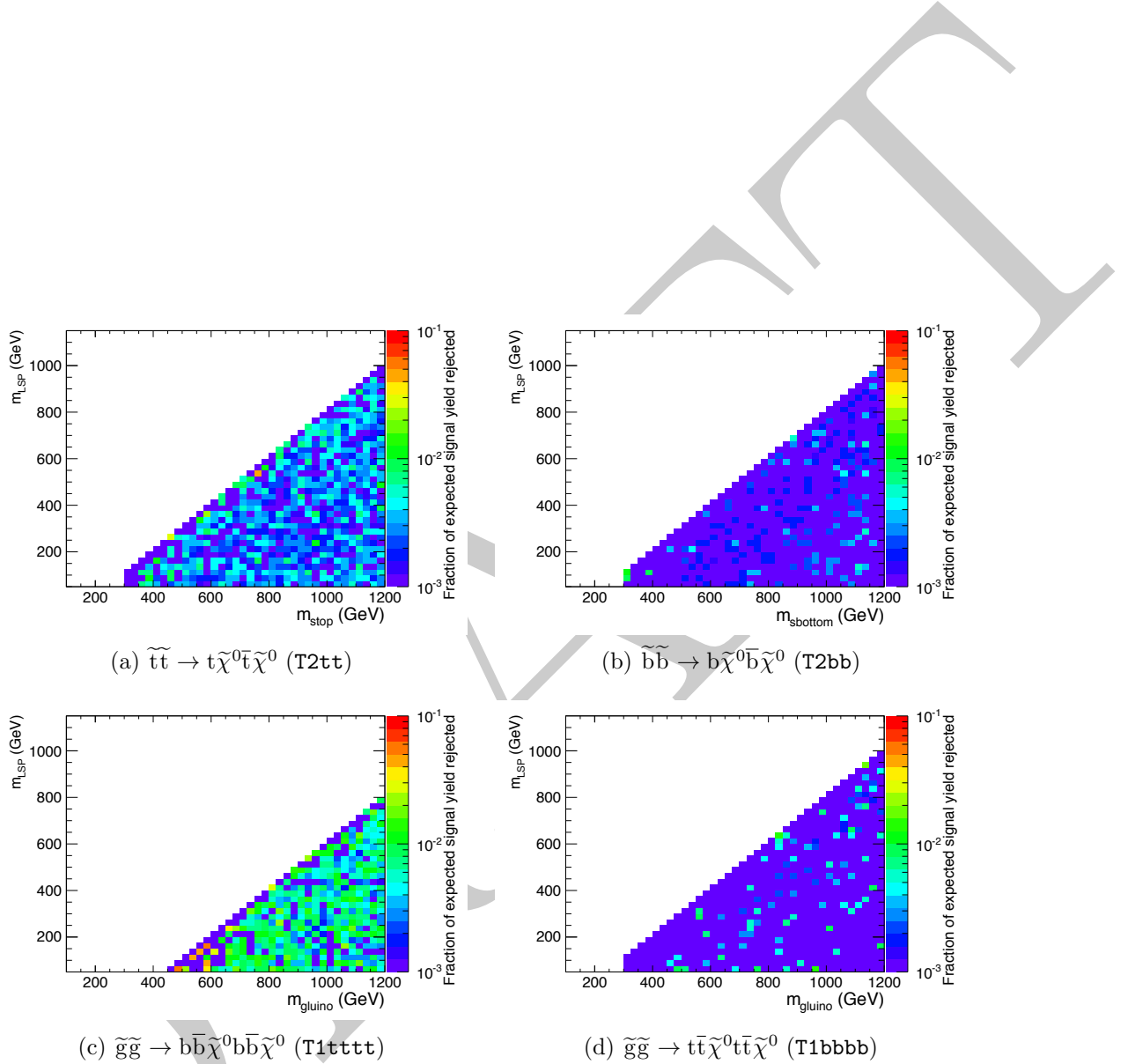


Figure E.16.: The fraction of expected signal yield that is rejected by the lepton and photon vetoes, for various topologies. No requirement is made on the number of reconstructed b jets.

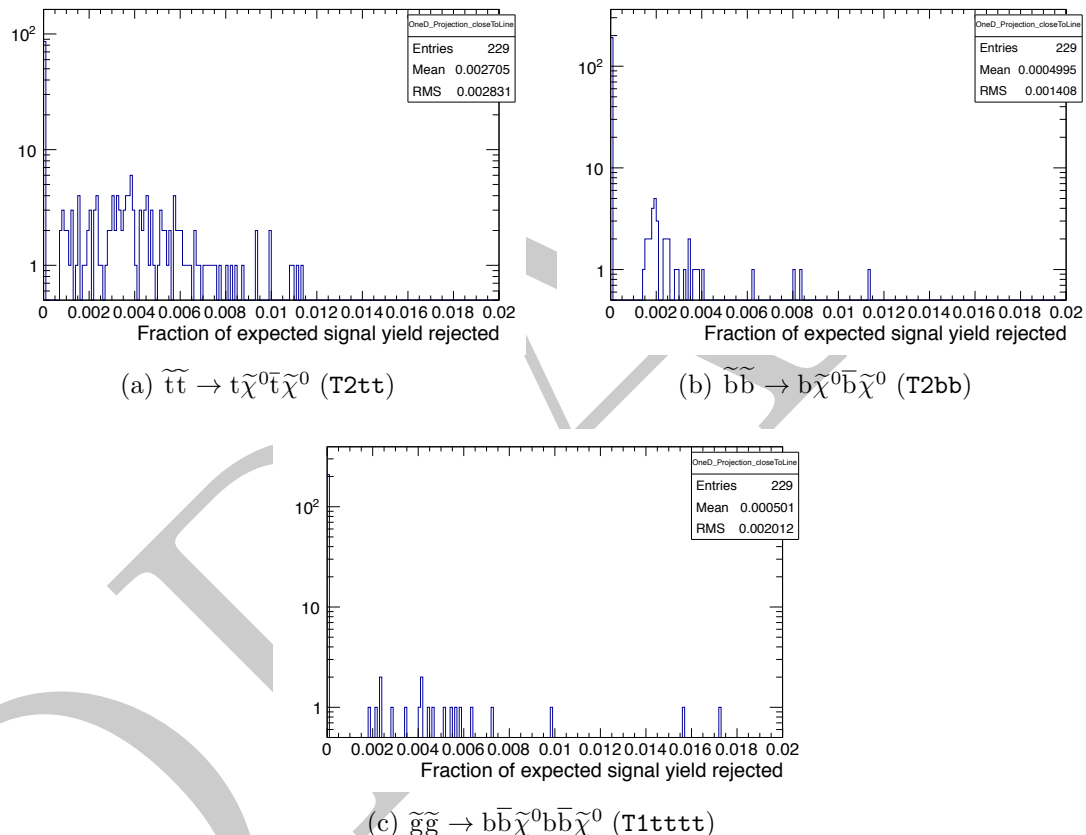


Figure E.17.: The fraction of expected signal yield that is rejected by the lepton and photon vetoes, near to the diagonal, for various topologies. No requirement is made on the number of reconstructed b jets.

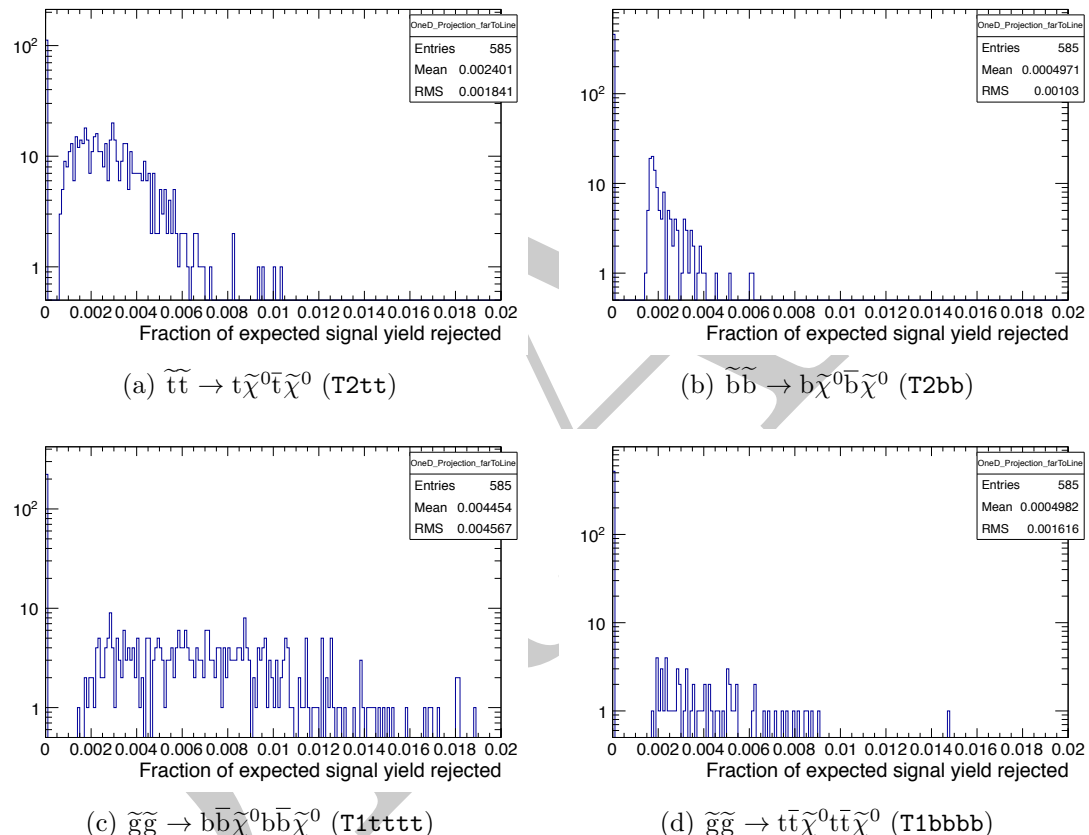


Figure E.18.: The fraction of expected signal yield that is rejected by the lepton and photon vetoes, far from the diagonal, for various topologies. No requirement is made on the number of reconstructed b jets.

Experimental systematic uncertainties on signal efficiency times acceptance

1

DRAFT

Bibliography

- [1] “Search for supersymmetry with the α_t variable in the 7 tev dataset of 2011,” no. CMS-AN-11-517, 2011.
- [2] E. Corbelli and P. Salucci, “The extended rotation curve and the dark matter halo of m33,” 1999.
- [3] T. A. Collaboration, “The ATLAS Experiment at the CERN Large Hadron Collider,” *JINST* **3** S08003, 2008.
- [4] S. Chatrchyan and others, “The CMS experiment at the CERN LHC,” *JINST*, vol. 03, p. S08004, 2008.
- [5] T. L. Collaboration, “The LHCb experiment at the CERN LHC,” *JINST* **3** S08005, 2008.
- [6] T. A. Collaboration, “The ALICE experiment at the CERN LHC,” *JINST* **3** S08002, 2008.
- [7] G. Hooft, “Renormalizable lagrangians for massive yang-mills fields,” *Nuclear Physics B*, vol. 35, no. 1, pp. 167 – 188, 1971.
- [8] G. Arnison, A. Astbury, B. Aubert, C. Bacci, G. Bauer, A. Bzaguet, R. Bck, T. Bowcock, M. Calvetti, T. Carroll, P. Catz, P. Cennini, S. Centro, F. Ceradini, S. Cittolin, D. Cline, C. Cochet, J. Colas, M. Corden, D. Dallman, M. DeBeer, M. D. Negra, M. Demoulin, D. Denegri, A. D. Ciaccio, D. DiBitonto, L. Dobrzynski, J. Dowell, M. Edwards, K. Eggert, E. Eisenhandler, N. Ellis, P. Erhard, H. Faissner, G. Fontaine, R. Frey, R. Frhwirth, J. Garvey, S. Geer, C. Ghesquiere, P. Ghez, K. Giboni, W. Gibson, Y. Giraud-Hraud, A. Givernaud, A. Gonidec, G. Grayer, P. Gutierrez, T. Hansl-Kozanecka, W. Haynes, L. Hertzberger, C. Hodges, D. Hoffmann, H. Hoffmann, D. Holthuizen, R. Homer, A. Honma, W. Jank, G. Jorat, P. Kalmus, V. Karimki, R. Keeler, I. Kenyon, A. Kernan, R. Kinnunen, H. Kowalski, W. Kozanecki, D. Krym, F. Lacava, J.-P. Laugier, J.-P. Lees, H. Lehmann, K. Leuchs,

- 1 A. Lvque, E. Linglin, E. Locci, M. Loret, J.-J. Malosse, T. Markiewicz, G. Maurin,
2 T. McMahon, J.-P. Mendiburu, M.-N. Minard, M. Moricca, H. Muirhead, F. Muller,
3 A. Nandi, L. Naumann, A. Norton, A. Orkin-Lecourtois, L. Paoluzi, G. Petrucci,
4 G. Mortari, M. Pimi, A. Placci, E. Radermacher, J. Ransdell, H. Reithler, J.-P. Revol,
5 J. Rich, M. Rijssenbeek, C. Roberts, J. Rohlf, P. Rossi, C. Rubbia, B. Sadoulet,
6 G. Sajot, G. Salvi, J. Salvini, J. Sass, A. Saudraix, A. Savoy-Navarro, D. Schinzel,
7 W. Scott, T. Shah, M. Spiro, J. Strauss, K. Sumorok, F. Szoncso, D. Smith, C. Tao,
8 G. Thompson, J. Timmer, E. Tscheslog, J. Tuominiemi, S. V. der Meer, J.-P. Vialle,
9 J. Vrana, V. Vuillemin, H. Wahl, P. Watkins, J. Wilson, Y. Xie, M. Yvert, and
10 E. Zurfluh, “Experimental observation of isolated large transverse energy electrons
11 with associated missing energy at $s=540$ gev,” *Physics Letters B*, vol. 122, no. 1,
12 pp. 103 – 116, 1983.
- 13 [9] T. D. Collaboration, “Measurement of the mass and width of the z_0 -particle from
14 multihadronic final states produced in e^+e^- annihilations,” *Physics Letters B*, vol. 231,
15 no. 4, pp. 539 – 547, 1989.
- 16 [10] P. W. Higgs, “Spontaneous Symmetry Breakdown without Massless Bosons,” *Physical
17 Review*, vol. 145, pp. 1156–1163, May 1966.
- 18 [11] P. W. Higgs, “Broken Symmetres and the Masses of Gauge Bosons,” *Physical Review
19 Letters*, vol. 13, pp. 508–509, Oct. 1964.
- 20 [12] T. C. Collaboration, “Observation of a new boson at a mass of 125 gev with the
21 cms experiment at the lhc,” *Physics Letters B*, vol. 716, no. 1, pp. 30 – 61, 2012.
- 22 [13] T. A. Collaboration, “Observation of a new particle in the search for the standard
23 model higgs boson with the atlas detector at the lhc,” *Physics Letters B*, vol. 716,
24 no. 1, pp. 1 – 29, 2012.
- 25 [14] N. Arkani-Hamed, P. Schuster, N. Toro, J. Thaler, L.-T. Wang, *et al.*, “Marmoset:
26 The path from lhc data to the new standard model via on-shell effective theories,”
27 2007.
- 28 [15] T. Sakuma, “3d sketchup images of the cms detector (120918),” 2012.
- 29 [16] T. C. Collaboration, “Cms tracking performance results from early lhc operation,”
30 *Eur. Phys. J. C*, vol. 70, p. 1165. 29 p, Jul 2010.
- 31 [17] *The CMS electromagnetic calorimeter project: Technical Design Report*. Technical
32 Design Report CMS, Geneva: CERN, 1997.

- ¹ [18] W. Smith, P. Busson, S. Dasu, J. Hauser, G. Heath, J. Krolikowski, J. Varela,
² A. Taurok, G. Wrochna, and P. Zotto, “Cms phyiscs technical design report: The
³ trigger system,” vol. 1, pp. 1–630, Dec 2000.
- ⁴ [19] “Ecal performance plots, 2012 data,” Jul 2012.
- ⁵ [20] “Cms ecal performance on 2011 data,” Feb 2012.
- ⁶ [21] T. C. collaboration, “Performance of cms muon reconstruction in pp collision events
⁷ at s = 7 tev,” *Journal of Instrumentation*, vol. 7, no. 10, p. P10002, 2012.
- ⁸ [22] CMS Collaboration, “The Trigger and Data Acquisition Project Technical Design
⁹ Report, Volume 1, The Level-1 Trigger,” *CERN/LHCC 2000-038, CMS TDR 6.1*,
¹⁰ 2000.
- ¹¹ [23] J. Marrouche and others, “Commissioning the CMS Global Calorimeter Trigger,”
¹² *CMS IN*, vol. 2010/029, 2010.
- ¹³ [24] I. et al., “Revised cms global calorimeter trigger functionality and algorithms,”
¹⁴ *Proceedings of the 12th Workshop on Electronics for LHC and Future Experimentsm*
¹⁵ *25-29 September 2006, Valencia, Spain.*
- ¹⁶ [25]
- ¹⁷ [26] tech. rep.
- ¹⁸ [27] L. Randall and D. Tucker-Smith, “Dijet Searches for Supersymmetry at the LHC,”
¹⁹ *arXiv*, vol. hep-ph, Jan. 2008.
- ²⁰ [28] CMS Collaboration, “SUSY searches with dijet events,” tech. rep., 2008.
- ²¹ [29] CMS Collaboration, “Search strategy for exclusive multi-jet events from supersym-
²² metry at CMS,” tech. rep., 2009.
- ²³ [30] M. Cacciari, G. Salam, and G. Soyez, “The anti-kt jet clustering algorithm,” *Journal*
²⁴ *of High Energy . . .*, Jan. 2008.
- ²⁵ [31] S. Chatrchyan and others, “Determination of Jet Energy Calibration and Transverse
²⁶ Momentum Resolution in CMS,” *arXiv*, vol. 6, p. P11002, 2011.
- ²⁷ [32] T. C. collaboration, “Determination of jet energy calibration and transverse mo-
²⁸ mentum resolution in cms,” *Journal of Instrumentation*, vol. 6, no. 11, p. P11002,
²⁹ 2011.

- ¹ [33]
- ² [34] T. C. Collaboration, “Cms physics technical design report, volume ii: Physics performance,” *Journal of Physics G: Nuclear and Particle Physics*, vol. 34, no. 6, p. 995, 2007.
- ⁵ [35] W. Adam, R. Frhwirth, A. Strandlie, and T. Todorov, “Reconstruction of electrons with the gaussian-sum filter in the cms tracker at the lhc,” *Journal of Physics G: Nuclear and Particle Physics*, vol. 31, no. 9, p. N9, 2005.
- ⁸ [36] CMS Collaboration, “Electron reconstruction and identification at $\sqrt{s} = 7$ TeV,” tech. rep., 2010.
- ¹⁰ [37] CMS Collaboration, “Performance of muon identification in pp collisions at $\sqrt{s} = 7$ TeV,” tech. rep., 2010.
- ¹² [38] CMS Collaboration, “Isolated Photon Reconstruction and Identification at $\sqrt{s} = 7$ TeV,” tech. rep., 2010.
- ¹⁴ [39] “Search for supersymmetry in final states with missing transverse energy and 0, 1, 2, 3, or at least 4 b-quark jets in 8 tev pp collisions using the variable alphat,” no. CMS-PAS-SUS-12-028, 2012.
- ¹⁷ [40] CMS Collaboration, “CMS b-tagging performance database,” tech. rep.
- ¹⁸ [41] tech. rep.
- ¹⁹ [42] “Updated measurements of the inclusive w and z cross sections at 7 tev,” no. CMS-AN-10-264, 2010.
- ²¹ [43] CMS Collaboration, “Data-Driven Estimation of the Invisible Z Background to the SUSY MET Plus Jets Search,” tech. rep., 2008.
- ²³ [44] Z. Bern, G. Diana, L. J. Dixon, F. Febres Cordero, S. Hoche, and others, “Driving Missing Data at Next-to-Leading Order,” *arXiv*, vol. D84, p. 114002, 2011.
- ²⁵ [45] E. M. Laird, “A Search for Squarks and Gluinos with the CMS Detector,” 2012.
- ²⁶ [46] B. C. Moneta and others, “The RooStats Project,” *Proceedings of Science*, 2010.
- ²⁷ [47] F. James, “MINUIT Reference Manual,” *CERN Program Library Writeup*, vol. D506.
- ²⁸ [48] M. Botje, J. Butterworth, A. Cooper-Sarkar, A. de Roeck, J. Feltesse, S. Forte, A. Glazov, J. Huston, R. McNulty, T. Sjostrand, and R. Thorne, “The PDF4LHC

- ¹ Working Group Interim Recommendations," *arXiv.org*, vol. hep-ph, Jan. 2011.
- ² [49] D. Stump, J. Huston, J. Pumplin, W.-K. Tung, H. Lai, *et al.*, "Inclusive jet production, parton distributions, and the search for new physics," *JHEP*, vol. 0310, p. 046, 2003.
- ⁵ [50] R. Thorne, A. Martin, W. Stirling, and G. Watt, "Status of MRST/MSTW PDF sets," 2009.
- ⁷ [51] M. Ubiali, R. D. Ball, L. Del Debbio, S. Forte, A. Guffanti, *et al.*, "Combined PDF and strong coupling uncertainties at the LHC with NNPDF2.0," 2010.
- ⁹ [52] B. C. Allanach, "SOFTSUSY: a program for calculating supersymmetric spectra," *Comput. Phys. Commun.*, vol. 143, p. 305, 2002.
- ¹¹ [53] S. M. T. Sjöstrand and P. Z. Skands, "PYTHIA 6.4 Physics and Manual," *JHEP*, vol. 05, p. 026, 2006.
- ¹³ [54] W. Beenakker and others, "Squark and gluino production at hadron colliders," *Nucl. Phys. B*, vol. 492, p. 51, 1997.
- ¹⁵ [55] K. Nakamura, "Review of particle physics," *J. Phys. G*, vol. 37, p. 075021, 2010.
- ¹⁶ [56] M. Kr amer, A. Kulesza, R. van der Leeuw, and others, "Supersymmetry production cross sections in pp collisions at $\sqrt{s} = 7$ TeV," *arXiv*.